1521-009X/47/11/1291–1306$35.00
DRUG METABOLISM AND DISPOSITION
https://doi.org/10.1124/dmd.119.086918
Drug Metab Dispos 47:1291–1306, November 2019




# Systematic Development and Verification of a Physiologically Based Pharmacokinetic Model of Rivaroxaban

Eleanor Jing Yi Cheong,[1] Denise Wun Xi Teo,[1] Denise Xin Yi Chua,[1] and Eric Chun Yong Chan

*Department of Pharmacy, Faculty of Science, National University of Singapore, Singapore, Singapore (E.J.Y.C., D.W.X.T., D.X.Y.C., E.C.Y.C.); and National University Cancer Institute, National University Hospital Medical Centre, Singapore, Singapore (E.C.Y.C.)*

Received February 17, 2019; accepted August 28, 2019

## ABSTRACT

**Rivaroxaban is indicated for stroke prevention in nonvalvular atrial fibrillation (AF). Its elimination is mediated by both hepatic metabolism and renal excretion. Consequently, its clearance is susceptible to both intrinsic (pathophysiological) and extrinsic (concomitant drugs) variabilities that in turn implicate bleeding risks. Upon systematic model verification, physiologically based pharmacokinetic (PBPK) models are qualified for the quantitative rationalization of complex drug-drug-disease interactions (DDDIs). Hence, this study aimed to develop and verify a PBPK model of rivaroxaban systematically. Key parameters required to define rivaroxaban's disposition were either obtained from in vivo data or generated via in vitro metabolism and transport kinetic assays. Our developed PBPK model successfully predicted rivaroxaban's clinical pharmacokinetic parameters within predefined success metrics. Consideration of basolateral organic anion transporter 3 (OAT3)–mediated proximal tubular uptake in tandem with apical P-glycoprotein (P-gp)–mediated efflux facilitated mechanistic characterization of the renal elimination of rivaroxaban in both healthy and renal impaired patients. Retrospective drug-drug interaction (DDI) simulations, incorporating in vitro metabolic inhibitory parameters, accurately recapitulated clinically observed attenuation of rivaroxaban's hepatic clearance due to enzyme-mediated DDIs with CYP3A4/2J2 inhibitors (verapamil and ketoconazole). Notably, transporter-mediated DDI simulations between rivaroxaban and the P-gp inhibitor ketoconazole yielded minimal increases in rivaroxaban's systemic exposure when P-gp–mediated efflux was solely inhibited, but were successfully characterized when concomitant basolateral uptake inhibition was incorporated in the simulation. In conclusion, our developed PBPK model of rivaroxaban is systematically verified for prospective interrogation and management of untested yet clinically relevant DDDIs pertinent to AF management using rivaroxaban.**

## SIGNIFICANCE STATEMENT

**Rivaroxaban is susceptible to DDDIs comprising renal impairment and P-gp and CYP3A4/2J2 inhibition. Here, systematic construction and verification of a PBPK model of rivaroxaban, with the inclusion of a mechanistic kidney component, provided insight into the previously arcane role of OAT3-mediated basolateral uptake in influencing both clinically observed renal elimination of rivaroxaban and differential extents of transporter-mediated DDIs. The verified model holds potential for investigating clinically relevant DDDIs involving rivaroxaban and designing dosing adjustments to optimize its pharmacotherapy in atrial fibrillation.**

## Introduction

Atrial fibrillation (AF) is the most common and clinically significant cardiovascular rhythm disorder. The Global Burden of Diseases, Injuries, and Risk Factors 2010 study indicated that the previous two decades have witnessed a progressive increase in the worldwide prevalence and incidence of AF with significant effects on associated morbidity and mortality (Chugh et al., 2014). Therapeutic mainstays of AF management can be chiefly divided into symptomatic treatment of arrhythmia by rate or rhythm control and prevention of thromboembolic complications by anticoagulation (January et al., 2014).

In recent years, direct oral anticoagulants have emerged as preferred alternatives to warfarin, particularly due to predictable dose-response relationships that eliminate the need for routine laboratory monitoring (Scaglione, 2013). Rivaroxaban, a non-vitamin K antagonist oral anticoagulant approved by the US Food and Drug Administration in 2010, is indicated for stroke prevention in nonvalvular AF. Rivaroxaban possesses a unique dual mode of elimination: where two-thirds of the systematically absorbed dose undergo CYP3A4/2J2-mediated metabolism while the remaining one-third is excreted unchanged in the urine, primarily via P-glycoprotein (P-gp)–mediated efflux (Mueck et al., 2013). This inevitably increases rivaroxaban's susceptibility to drug-drug-disease interactions (DDDIs) attributed to simultaneous impairment of its multiple clearance pathways (Grillo et al., 2012).

This work was supported by the Singapore Ministry of Education Tier 1 Academic Research Funding [Grant R-148-000-193-112] (to E.C.Y.C.); National University of Singapore (NUS) President's Graduate Fellowship (to E.J.Y.C.); and NUS, Department of Pharmacy, Final Year Project Funding [Grant C-148-000-003-001] (to D.W.X.T. and D.X.Y.C.).

[1]E.J.Y.C., D.W.X.T., and D.X.Y.C. contributed equally to this work.

https://doi.org/10.1124/dmd.119.086918.

This article has supplemental material available at dmd.aspetjournals.org.

**ABBREVIATIONS:** AF, atrial fibrillation; AUC, area under the curve; CKD, chronic kidney disease; CL, clearance; CL/F, apparent clearance; $CL_{PD}$, passive diffusion clearance; $CL_R$, renal clearance; $CL_{u,int}$, unbound intrinsic clearance; $CL_{u,int,T}$, unbound intrinsic clearance of P-gp–mediated tubular secretion; DDDI, drug-drug-disease interaction; DDI, drug-drug interaction; GFR, glomerular filtration rate; INH, intact nephron hypothesis; IVIVE, in vitro to in vivo extrapolation; $J_{max}$, maximum rate of active transport; $K_m$, Michaelis constant; MDCK, Madin-Darby canine kidney; MDR1, multidrug resistance-1; OAT, organic anion transporter; PBPK, physiologically based pharmacokinetic; P-gp, P-glycoprotein; PK, pharmacokinetic; $P_{pass}$, passive permeability; PTCPGK, proximal tubular cells per gram of kidney.

The likelihood of drug-drug interactions (DDIs) is markedly increased when we consider that many rhythm and rate control agents (e.g., amiodarone, carvedilol, and diltiazem) likely to be coadministered with rivaroxaban in AF are known CYP3A4/2J2 and/or P-gp inhibitors (Wessler et al., 2013; US Food and Drug Administration, 2017). Furthermore, given that the prevalence of AF burgeons in the elderly population (Chugh et al., 2014), assessing the implications of age-related physiologic decline on the extent of these clinically relevant DDIs also becomes essential to guide pharmacotherapy. Nevertheless, practical constraints often restrict the number of dedicated trials that can be conducted to evaluate all clinically plausible permutations. Consequently, physiologically based pharmacokinetic (PBPK) modeling has emerged as a valuable tool in the quantitative rationalization of pharmacokinetic (PK) variabilities due to complex DDDIs.

By coupling the defining properties of rivaroxaban and the biologic system with trial design, the minimal PBPK models developed by Grillo et al. (2012) and Ismail et al. (2018) have prospectively established clinically significant DDDIs between rivaroxaban and erythromycin or verapamil in renal-impaired patients. The findings were instrumental in substantiating cautionary language discouraging concomitant administration of rivaroxaban with moderate CYP3A4/P-gp inhibitors in patients with renal dysfunction (US Food and Drug Administration, 2011b). Nevertheless, subsequent model verification using clinical DDI data uncovered a key limitation of the current minimal PBPK models where major physiologic compartments (except the liver) are combined with the plasma compartment. While these PBPK models incorporated interactions comprising both CYP3A4 and P-gp pathways, clinical urinary excretion data revealed negligible decreases in the renal clearance of rivaroxaban when it was coadministered with either erythromycin or verapamil in healthy patients (Moore et al., 2014; Greenblatt et al., 2018). This invalidated the initial assumption of a transporter-mediated component mediating the observed DDDI. Hence, to justify PBPK-guided extrapolation beyond the clinical trial population in the investigation of potential DDDIs involving rivaroxaban, mechanistic delineation of passive and active processes governing the renal clearance of rivaroxaban becomes essential.

Consequently, this study aims to develop and verify a full PBPK model for rivaroxaban via incorporation of both in vivo clinical PK data as well as in vitro experimental measurements, which can be used to inform drug-specific parameters through in vitro to in vivo extrapolation (IVIVE). Upon successful recapitulation of observed rivaroxaban PK and urinary excretion profiles in both healthy and renal-impaired patients, in vitro inhibitory parameters utilizing rivaroxaban as the probe substrate would be quantified and employed in retrospective DDI simulations linking rivaroxaban with prototypical CYP3A4/2J2 and P-gp inhibitors (ketoconazole and verapamil, which yield different quantitative effects on the renal clearance of rivaroxaban). We envision that this systematic approach to PBPK model verification would eventually instill confidence in acting on model-generated insights to support the rational dose selection of rivaroxaban in previously untested, albeit realistically complex clinical scenarios. The long-term aim is to minimize inadvertent increases in the systemic exposure of rivaroxaban while preserving its anticoagulant efficacy.

## Materials and Methods

The workflow schematic adopted for PBPK model development, verification, and iterative refinement is illustrated in Fig. 1. Mechanistic modeling of permeability and transport kinetics was implemented with the Simcyp In Vitro Analysis Toolkit (version 3). All PK simulations presented herein were conducted using a population-based absorption, distribution, metabolism, and excretion simulator (version 17; Simcyp, Sheffield, UK).

### Model Development

**PBPK Model of Rivaroxaban.** Key drug-dependent parameters necessary for simulation of the kinetics of rivaroxaban are delineated in Table 1. Oral absorption of rivaroxaban was predicted with the advanced dissolution, absorption, and metabolism model implemented in Simcyp. The effective permeability of rivaroxaban in human was derived from in vitro apparent permeability measured in Caco-2 cell monolayers (Gnoth et al., 2011) using the apparent permeability/effective permeability correlation model within the simulator. Upon defining its intrinsic solubility (Takács-Novák et al., 2013), the dissolution rate of rivaroxaban was estimated with the diffusion layer model developed by Wang and Flanagan (1999). The effects of bile on the in vivo solubility estimated in each segment of the gastrointestinal tract were quantified via the bile micelle:water partition coefficient, calculated from the predefined log P via a quantitative structure-activity relationship model developed by Glomme et al. (2007). Simulated solubility outputs were compared with experimental biorelevant solubility measurements (Takács-Novák et al., 2013) and the bile micelle:water partition coefficient was manually adjusted to achieve concordance. Subsequently, a whole body PBPK model was applied to describe the distribution of rivaroxaban, where the tissue-to-plasma distribution equilibrium ratios were calculated via mechanistic tissue composition equations developed by Rodgers and Rowland (2006). The volume of distribution at steady state was predicted to be 0.2 l/kg, which is lower than the observed in vivo volume of distribution at steady state of approximately 0.62 l/kg (Mueck et al., 2014). Hence, a tissue:plasma partition coefficient scalar (applied equally to all tissues) of 2.2 was applied to optimize the volume of distribution at steady state.

**Hepatic Metabolism.** The oral apparent clearance (CL/F) and renal clearance ($CL_R$) data were collated from primary literature sources following administration of rivaroxaban to healthy adult subjects (Supplemental Table 1). Overall weighted mean clearances were calculated using the following equation:

$$W\bar{X} = \frac{\sum_{j=1}^{J} n_j \cdot \bar{x}_j}{\sum_{j=1}^{J} n_j} \quad (1)$$

where $W\bar{X}$ is the weighted mean; $n_j$ is the number of subjects in the $j$th study; and $x_j$ is the mean of the $j$th study. Here, a study is defined as the data associated with a group of subjects being administered a specific dose and dosing regimen of rivaroxaban on a particular occasion with $n$ number of subjects. Based on a fractional metabolism in the liver of 0.37 for CYP3A4 and 0.29 for CYP2J2, as reported by Grillo et al. (2012), the unbound intrinsic clearance ($CL_{u,int}$) values of rivaroxaban mediated by CYP3A4 and CYP2J2 were derived from the weighted mean of CL/F after accounting for the contribution of $CL_R$ via retrograde application of the well-stirred model.

**Mechanistic Kidney Model Development.** The differential contribution of the primary processes governing the renal disposition of rivaroxaban (i.e., glomerular filtration, tubular secretion, and tubular reabsorption) was quantified via by the mechanistic kidney model within the simulator. In vitro transport assays investigating the P-gp–mediated efflux kinetics of rivaroxaban were first performed in Madin-Darby canine kidney (MDCK) subclone I cells transfected with multidrug resistance-1 (MDR1) protein. To account for the bidirectional passive permeability of rivaroxaban across the apical and basolateral membranes in addition to apical P-gp–mediated efflux driven by unbound intracellular rivaroxaban concentrations, time-dependent (60–420 minutes) and concentration-dependent (3–100 $\mu$M donor rivaroxaban) data, measured in the absorptive (apical-to-basolateral) direction, were fitted to a mechanistic model that dynamically simulates flux in rivaroxaban concentrations within the apical, basolateral, and intracellular compartments of the Transwell apparatus. Derived in vitro estimates of the maximum rate of active transport ($J_{max}$), Michaelis constant ($K_m$), and passive permeability ($P_{pass}$) were subsequently subjected to quantitative IVIVE scaling as highlighted in eqs. 2 and 3 to simulate the intrinsic clearance attributed to in vivo P-gp–mediated tubular secretion ($CL_{u,int,T\ per\ kidney}$) and passive diffusion clearances ($CL_{PD,kidney}$) that contribute to tubular reabsorption, respectively.

$$CL_{u,int,T\ per\ kidney} = \frac{J_{max}}{K_{m,u}} / CL_{u,int} \times REF_{PTC} \times PTCPGK \times \text{kidney weight} \quad (2)$$

$$CL_{PD,kidney} = \frac{P_{pass} \times \text{Nephron surface area based on two kidneys}}{PTCPGK \times \text{kidney weight}} \quad (3)$$

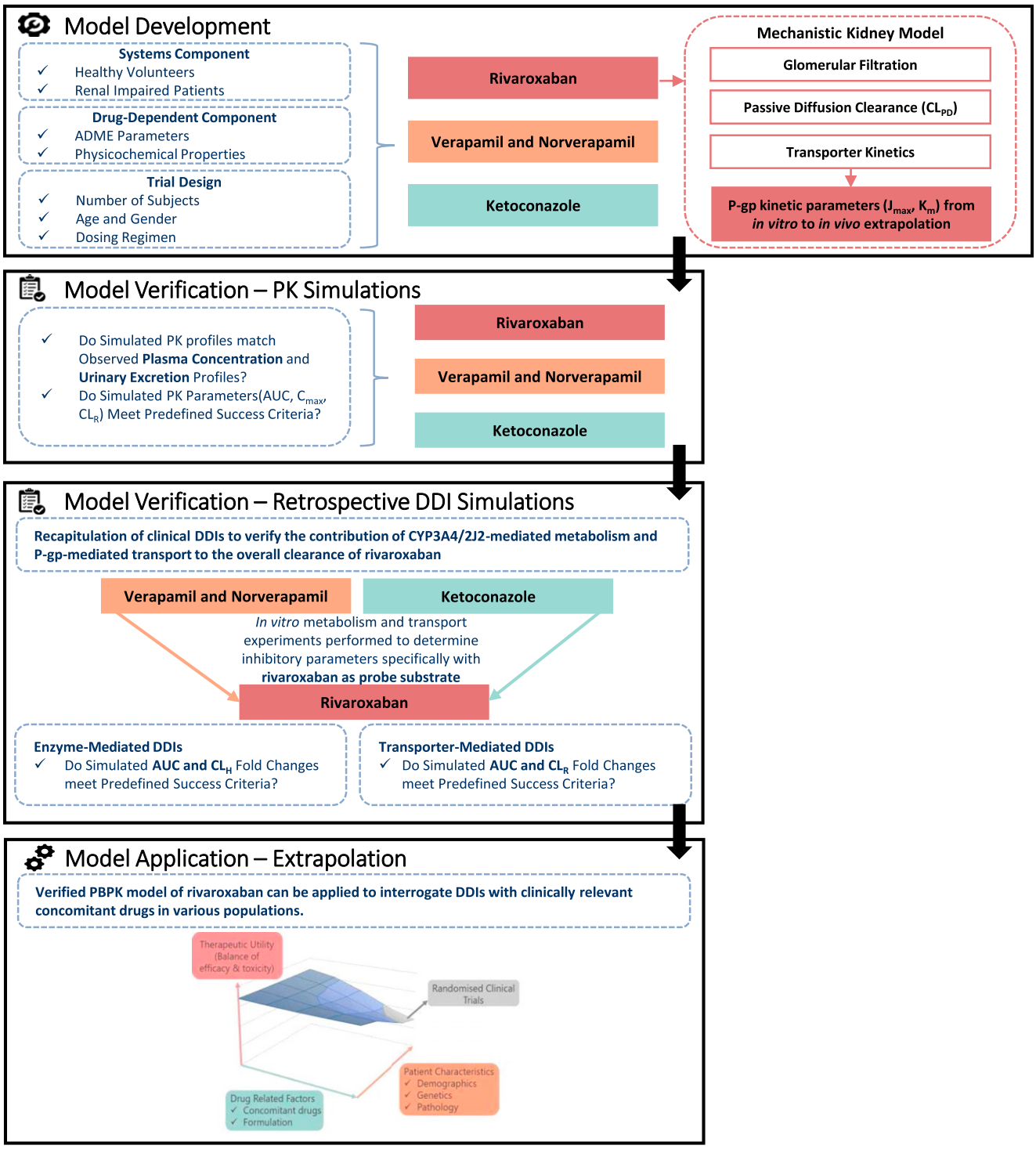


**Fig. 1.** PBPK modeling framework detailing the iterative processes of model development and verification that were performed in this study. Successful model verification must precede application of the PBPK model of rivaroxaban for prospective predictions of DDDIs.

In eq. 2, the $J_{max}$ value (picomoles per minute) generated was first normalized to the protein concentration in each Transwell insert, quantified using bicinchoninic acid protein assay. The $J_{max}$ value was subsequently converted from picomoles per minute per milligram of protein to picomoles per minute per $10^6$ of cells based on 1 million MDCK cells containing 0.08 mg of total protein (Scotcher et al., 2017). Differential P-gp mRNA expression data in the kidney, intestine, and MDCK cells was used to inform the relative expression factor of the proximal tubular cells (i.e., $REF_{PTC}$ in eq. 2) (Scotcher et al., 2017). In eq. 3, the total nephron surface area (291 $cm^2$), kidney weight (341.5 g), and number of proximal tubular cells per gram of kidney, [(PTCPGK), 60 million in a healthy population] were used as IVIVE scaling factors to convert the in vitro apparent permeability to $CL_{PD}$ (Emami Riedmaier et al., 2016).

Further details on the chemicals, culture techniques, modeling, and fitting procedures used are highlighted in the Supplemental Material.

**PBPK Models of Inhibitors (Ketoconazole and Verapamil).** Ketoconazole, verapamil, and its primary metabolite, norverapamil, are prototypical CYP3A4/2J2 as well as P-gp inhibitors that have been implicated in clinical DDIs with rivaroxaban (Mueck et al., 2013; Greenblatt et al., 2018). In the construction of

TABLE 1

Key input parameters for the PBPK model of rivaroxaban

| Parameter | Value | Method/Reference |
|---|---|---|
| Molecular weight (g/mol) | 435.88 | CAS ID: 366789-02-8 |
| Log P | 1.5 | Mueck et al., 2014 |
| Compound type | Neutral | |
| B/P | 0.71 | Grillo et al. 2012 |
| $f_u$ | 0.065 | Grillo et al., 2012 |
| Main plasma binding protein | Human serum albumin | (US Food and Drug Administration, 2011a)— |
| Absorption model | ADAM model | |
| $f_{u,gut}$ | 0.21 | Predicted |
| $P_{eff,man}$ ($10^{-4}$ cm/s) | 3.020492 | Predicted |
| Permeability assay | Caco-2 | Gnoth et al., 2011 |
| Apical pH: Basolateral pH | 7.4: 7.4 | Gnoth et al., 2011 |
| Activity | Passive and active | Gnoth et al., 2011 |
| $P_{app,A:B}$ ($10^{-6}$ cm/s) | 8 | Gnoth et al., 2011 |
| Reference compound | Multiple | Gnoth et al., 2011 |
| Reference compound $P_{app,A:B}$ ($10^{-6}$ cm/s) | 0 | Gnoth et al., 2011 |
| Scalar | 1.284077 | Predicted |
| Solubility pH Type | Intrinsic | |
| Solubility (mg/ml) | 0.01 | Takács-Novák et al., 2013 |
| Transporter | ABCB1 (P-gp/MDR1) | |
| $J_{max}$ (pmol/min) | 37.83 | Determined experimentally |
| $K_m$ ($\mu$M) | 9.416 | Determined experimentally |
| $f_{u,inc}$ | 1 | Predicted |
| Insert growth area of the Transwell ($cm^2$) | 0.33 | Determined experimentally |
| System | MDCK | Determined experimentally |
| RAF/REF | 1.5 | |
| Distribution model | Full PBPK model | |
| $V_{SS}$ (l/kg) | 0.3824139 | Predicted: method 2 |
| Enzyme | CYP3A4 | Predicted in Simcyp using the Retrograde Calculator |
| Pathway | Pathway 1 | |
| $CL_{int}$ ($\mu$l/min per picomoles) | 0.06353705 | |
| Enzyme | CYP2J2 | Predicted in Simcyp using the Retrograde Calculator |
| Pathway | Pathway 1 | |
| $CL_{int}$ ($\mu$l/min per picomoles) | 5.685421 | |
| $CL_{int}$ (HLM) ($\mu$l/min per milligram protein) | 7.998799 | Predicted in Simcyp using the Retrograde Calculator |
| Mechanistic kidney model | | |
| $CL_{PD,basal}$ (ml/min per million proximal tubular cells) | 1.09E−05 | Determined experimentally |
| $CL_{PD,apical}$ (ml/min per million proximal tubular cells) | 1.09E−05 | Determined experimentally |
| $f_{u,kidney,cell}$ | 0.3788975 | Predicted in Simcyp |
| $f_{u,urine}$ | 1 | |
| Transporter | SLC22A8 (OAT3) | |
| Function | Uptake | |
| $CL_{int,T}$ ($\mu$l/min per million cells) | 43 | Scaled using sensitivity analysis |
| Transporter | ABCB1 (P-gp/MDR1) | |
| Function | Efflux | |
| $J_{max}$ (pmol/min per million cells) | 80.921 | Determined experimentally |
| $K_m$ ($\mu$M) | 9.416 | Determined experimentally |
| RAF/REF | 4 | |

ADAM, advanced dissolution, absorption, and metabolism; B/P, blood to plasma partition ratio; CAS, Chemical Abstracts Service; $CL_{int}$, in vitro intrinsic clearance; $CL_{int,T}$, in vitro transporter-mediated intrinsic clearance; $f_u$, fraction unbound in plasma; $f_{u,gut}$, fraction unbound in the enterocytes; $f_{u,inc}$, fraction unbound in the in vitro incubation; $f_{u,urine}$, fraction unbound in the urine; $f_{u,kidney,cell}$, fraction unbound in the kidney cell; HLM, human liver microsomes; ID, identification; log P, common logarithm of the octanol:water partition coefficient; $P_{app,A:B}$, apical-basolateral in vitro apparent permeability; $P_{eff,man}$, human jejunum effective permeability; RAF/REF, relative activity factor/relative expression factor; $V_{ss}$, volume of distribution at steady state.

PBPK-DDI models, the verified compound file of ketoconazole provided in Simcyp (version 17) was used. In the case of verapamil, although the compound file provided in Simcyp (version 17) allowed adequate modeling of the PK profile of an immediate-release formulation, coadministration of rivaroxaban and sustained-release verapamil capsules in the trial by Greenblatt et al. (2018) necessitated further refinement of verapamil's absorption kinetics. As described in Supplemental Fig. 1, a sequential one-stage convolution procedure was implemented that models the relationship between the in vitro dissolution profile and the observed plasma concentration-time profile of verapamil. Final model parameters for ketoconazole and verapamil are summarized in Supplemental Tables 2.1–2.3.

### Model Verification: PK Simulations

**Verification of Basal PBPK Model of Rivaroxaban and Verapamil.** The PK profiles following single or multiple administrations of clinically relevant doses to healthy subjects using the default healthy NEurCaucasian population available within Simcyp were first simulated to verify the performance of the PBPK models of rivaroxaban and verapamil. During the model verification process, the population, number of participants, dose, and regimen selected for the simulations were matched to the corresponding clinical study designs (Supplemental Table 3). A total of 10 trials were simulated to assess variability across groups. The predictive accuracies of the PBPK models were evaluated via visual predictive checks against average plasma concentration-time data digitized using WebPlotDigitizer (version 4.0, https://automeris.io/WebPlotDigitizer). Additionally, a metric approach detailed by Abduljalil et al. (2014) that considers both the intrinsic variability of observed PK parameters [i.e., area under the curve (AUC) and peak plasma concentration, ($C_{max}$)] as well as the clinical sample size was also applied to assess simulated values.

**Simulation of Rivaroxaban's $CL_R$ Using the Mechanistic Kidney Model in a Healthy Population and in Patients with Mild Renal Impairment.** Simulations of rivaroxaban's plasma concentration-time and urinary excretion profiles in a healthy population using the final mechanistic model were first compared with the PBPK model of rivaroxaban, where the weighted mean $CL_R$ collated from seven independent studies was defined as a single input parameter

(Supplemental Table 1). Upon verification of the predictive capabilities of the mechanistic kidney model in healthy subjects, system-dependent parameters within the model were further modified to reflect potential physiologic changes synonymous with renal impairment. Based on the intact nephron hypothesis (INH) by Bricker (1969), damaged nephrons stop working completely while undamaged nephrons function normally; consequently, proportional reductions in tubular secretion and glomerular filtration would likely be observed in chronic kidney disease (CKD). In this study, a decline in PTCPGK was used to represent the loss of tubular cells, and hence active secretion that is consistent with the INH concept. Consequently, the default value of 60 million PTCPGK corresponding to the representative glomerular filtration rate (GFR) of a healthy population (136.4 ml/min) was scaled down proportionally to 28.6 million according to the median GFR that occurs in mild renal impairment (GFR = 65 ml/min in a range of 50–79 ml/min) (Scotcher et al., 2017; Hsueh et al., 2018) (Supplemental Table 4). This newly defined population was subsequently used to predict the observed attenuations in rivaroxaban's $CL_R$ in mild renal impairment (Supplemental Material).

### Model Verification: Retrospective DDI Simulations

Upon accurate recapitulation of rivaroxaban's PK, performance verification in both the uninhibited and inhibited states is essential to ascertain that rivaroxaban has been adequately characterized as a DDI victim (Shebley et al., 2018). Hence, PBPK-DDI models were constructed via the incorporation of in vitro inhibitory parameters describing the inhibitory potential of verapamil, norverapamil, and ketoconazole against the CYP3A4/2J2-mediated metabolism as well as P-gp–mediated secretion of rivaroxaban (Supplemental Material). For DDI simulations, statistical analyses were performed using SPSS version 22 (IBM Corp., Armonk, NY). The AUC, $C_{max}$, and clearance (CL) values of rivaroxaban were analyzed assuming log normally distributed data. Student's *t* test was used to analyze the difference in these parameters in the absence and presence of concomitant inhibitors. Point estimates and exploratory 90% confidence intervals for the ratios were calculated by retransformation of the logarithmic results. Based on these analyses, a refined predictive measure proposed by Guest et al. (2011) incorporating PK variability coupled with variable prediction boundaries dependent on the extent of interaction was applied in defining the success of the DDI simulations.

### Model Refinement

**Incorporation of Organic Anion Transporter 3–Mediated Basolateral Uptake of Rivaroxaban.** Consideration of glomerular filtration, tubular reabsorption via passive permeability clearances, and apical P-gp–mediated secretion resulted in an underestimation of rivaroxaban's $CL_R$, alluding to potential undefined mechanisms governing rivaroxaban's renal disposition. Tsuruya et al. (2017) reported the specific uptake of rivaroxaban in mouse organic anion transporter (OAT) 3–expressing cells, with $J_{max}$ and $K_m$ values in mouse OAT3-transfected cells determined to be 72.9 ± 46.8 pmol/min per mg of protein and 1.01 ± 0.70 $\mu$M, respectively. In the absence of transporter abundance or expression to facilitate allometric scaling, rivaroxaban uptake was independently investigated in this study using human OAT3-transfected human embryonic kidney cell lines obtained from Dr. Kathleen Giacomini (University of California, San Francisco, CA). Details on the culture techniques, uptake assay protocol, two-compartmental modeling, and fitting procedures are highlighted in the Supplemental Material. The derived in vitro active uptake clearance was similarly subjected to IVIVE using eq. 3 correcting for measured protein (0.15 mg) per million of human embryonic kidney cells. An alternative top-down approach was further used to estimate the $CL_{u,int}$ value governing OAT3-mediated uptake. Using sensitivity analysis optimization, the $CL_{u,int}$ value was determined to be the value producing a simulated $CL_R$ value that converged with the weighted mean $CL_R$ value of 3.1 l/h when serum creatinine was fixed at 80 $\mu$mol/l (corresponding to GFR = 120 ml/min in healthy volunteers) (Scotcher et al., 2017).

## Results

### Development and Verification of the PBPK Models of Rivaroxaban and Verapamil

**Basal PBPK Model of Rivaroxaban Recapitulated Clinically Observed PK Profiles.** The weighted mean CL/F and $CL_R$ values of rivaroxaban collated from seven independent studies in healthy volunteers were 8.6 and 3.1 l/h, respectively (Supplemental Table 1). Using the retrograde model, the $CL_{u,int}$ values attributed to CYP2J2 and CYP3A4 were calculated to be 5.69 and 0.064 $\mu$l/min per picomole of isoform, with additional liver clearance defined to be 8.00 $\mu$l/min per milligram of liver microsomal protein Table 1. The effect of food in enhancing rivaroxaban's bioavailability at the 20 mg dose strength was recapitulated by considering the differential influences of fasted versus fed conditions on the extent of bile micelle-mediated solubilization (Fig. 2A; Tables 2, 3, and 4). As highlighted in Table 2, the simulated geometric mean AUC was 1512 $\mu$g·h/l in the fasted state compared with 2127 $\mu$g·h/l in the fed state. This predicted 1.41-fold increase in the presence of food was aligned with the 1.39-fold change observed in a phase I confirmatory food-effect trial (Stampfuss et al., 2013). Model predictive performance was further assessed using external verification data sets from independent clinical trials not used in model development. Plasma concentration-time profiles of 10 mg (Fig. 2B) and 20 mg (Fig. 2C) doses of rivaroxaban (Supplemental Material) compared well with the referenced published studies by Mueck et al. (2013) and Greenblatt et al. (2018), respectively, with the observed PK parameters (AUC, $C_{max}$, and CL) falling within the prespecified PK prediction criteria (Tables 2–4).

**Three-Compartmental Analysis Enabled Accurate Determination of Kinetic Constants Governing the In Vitro P-gp–Mediated Efflux of Rivaroxaban.** Approximately one-third (36%) of the absorbed dose of rivaroxaban is excreted unchanged in the kidney, with active tubular secretion accounting for 30% (Mueck et al., 2013). As a result, accurate estimation of kinetic parameters governing the P-gp–mediated efflux of rivaroxaban based on in vitro data is critical for successful IVIVE of its renal disposition. Preliminary analyses of bidirectional MDCK-MDR1 transport assays via the conventional Michaelis-Menten approach established time-linear conditions for both absorptive (Supplemental Fig. 2A) and basolateral rivaroxaban transport (Supplemental Fig. 2B) as well as the superior sensitivity of absorptive flux (Supplemental Fig. 2C) compared with basolateral flux (Supplemental Fig. 2D) in response to apical P-gp efflux activity. However, as seen in Supplemental Fig. 2C, solubility limitations prevented saturation of rivaroxaban transport in the absorptive direction. Hence, to account for the interaction of P-gp with unbound intracellular concentrations of rivaroxaban, mechanistic three-compartmental modeling was subsequently applied to analyze both time- and concentration-dependent data describing rivaroxaban's absorptive transport. Unbound rivaroxaban concentrations in the extracellular and intracellular compartments, determined via ultrafiltration experiments to be 1 and 0.023, respectively, were incorporated as fixed drug-dependent parameters (Supplemental Table 5). The apparent $J_{max}$ and apparent $K_m$ values (97.98 pmol/min and 836.8 $\mu$M, respectively) determined using the conventional Michaelis-Menten approach were also used as a priori information for naive pooled fitting via both hybrid and local (Nelder-Mead) optimization procedures. As highlighted in Table 5, the convergence of $J_{max}$ and $K_m$ estimates from two different optimization methods attested to the robustness of the three-compartmental approach and established that fitting outcomes were minimally influenced by the initial $J_{max}$ and $K_m$ values. Visual predictive checks also demonstrated consistency between experimental measurements and simulated rivaroxaban concentration-time profiles in the basolateral compartment (Fig. 3, A and B). Given that the Nelder-Mead optimization resulted in lower corrected Akaike information criterion values, estimates of $J_{max}$ = 37.83 pmol/min, $K_m$ = 9.42 $\mu$M, and $P_{pass}$ = 12.88 × $10^6$ cm/s were subjected to quantitative IVIVE via eqs. 2 and 3 to generate $CL_{u,int,T\ per\ kidney}$ ($J_{max}$ = 80.921 pmol/min per $10^6$ of cells and $K_{m,u}$ = 9.42 $\mu$M) and $CL_{PD,kidney}$ (1.09 × $10^{-5}$ $\mu$l/min per $10^6$ of cells) for parameterization of the mechanistic kidney model (Table 1).

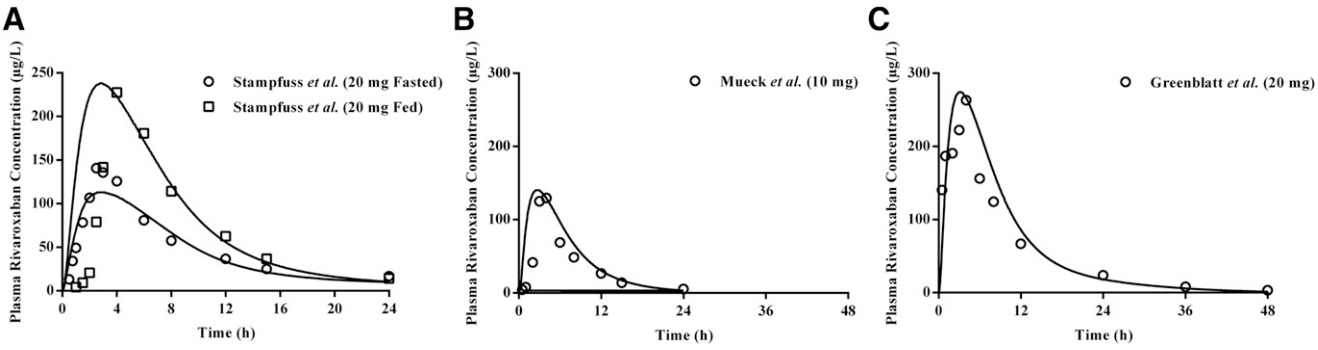


**Fig. 2.** Simulated pharmacokinetic profiles of rivaroxaban after single dose administration. Simulated mean (solid line) plasma drug concentration-time profiles of single dose rivaroxaban demonstrated (A) the effect of food in increasing bioavailability at the 20 mg dose and accurately recapitulated clinically observed profiles at 10 mg (B) and 20 mg (C) doses. Open symbols represent clinical data.

**IVIVE of Rivaroxaban's Renal Clearance Revealed the Pivotal Role of Basolateral Uptake.** Using the mechanistic kidney model, the relative contribution of various processes (i.e., glomerular filtration, tubular reabsorption, and active secretion) involved in rivaroxaban's renal excretion clearance was assessed in a stepwise manner. Expectedly, consideration of either glomerular filtration in isolation or both glomerular filtration and passive tubular reabsorption resulted in substantial underprediction of rivaroxaban's $CL_R$ (predicted $CL_R$ values of 0.41 and 0.36 l/h, respectively) (Fig. 4A) and a corresponding overestimation of its systemic exposure (Fig. 4B), underscoring the significance of active renal secretion in mediating rivaroxaban's renal disposition. However, sole incorporation of P-gp–mediated apical efflux demonstrated marginal effects on both $CL_R$ and systemic exposure (Fig. 4, A and B). As highlighted in Table 7, without OAT3-mediated basolateral uptake, the $CL_R$ value was underpredicted by 85% and the predicted AUC was 1.51-fold higher than that reported by Greenblatt et al. (2018), falling outside the prespecified success criteria. Hence, this provided the impetus for mechanistic investigation of OAT3-mediated rivaroxaban uptake.

**Kinetic Constants Governing In Vitro OAT3-Mediated Uptake of Rivaroxaban Were Comparable to Top-Down Estimates of OAT3-Mediated Intrinsic Clearance.** Upon establishing the functionality of the OAT3/OAT1-transfected systems (Supplemental Fig. 3, A and B), preliminary investigation of potential rivaroxaban uptake was performed. The uptake of rivaroxaban by human OAT3-expressing cells was higher than that by the empty vector transfected cells at 5 minutes and was further inhibited by a prototypical OAT inhibitor, probenecid (50 $\mu$M) (Supplemental Fig. 3C). In contrast, the uptake of rivaroxaban by human OAT1-expressing cells was comparable to that of the empty vector transfected cells at 5 minutes (Supplemental Fig. 3D). Taken together, rivaroxaban is a substrate of human OAT3 but not human OAT1. Time-dependent rivaroxaban uptake was subsequently evaluated, and linearity was preserved up to 2 minutes (Supplemental Fig. 3E). Consequently, concentration-dependent transport of rivaroxaban (0.5–100 $\mu$M) was investigated under time-linear conditions in both wild-type and OAT3-transfected cells (Supplemental Fig. 3G). Total rivaroxaban uptake (Supplemental Fig. 3H, solid black line) was fitted via the conventional two-step approach (Supplemental Material). Accounting for passive diffusion (Supplemental Fig. 3F), calculated to be 22.65 $\mu$l/min per $10^6$ of cells, saturable active uptake was observed with transporter-mediated intrinsic clearance estimated to be 33.91 $\mu$l/min per $10^6$ of cells (Supplemental Fig. 3H, gray solid line). Given that data from 2-minute incubations have been shown to produce large S.E. values in the estimation of $CL_{PD}$ (Ménochet et al., 2012), $CL_{PD,kidney}$ ($1.09 \times 10^{-5}$ $\mu$l/min per $10^6$ of cells obtained previously via IVIVE scaling) and transporter-mediated intrinsic clearance derived from the two-step approach were eventually used as initial estimates for naive pooled fitting of measured time- and concentration-dependent data via two-compartmental modeling. Visual predictive checks demonstrated consistency between experimental measurements and simulated intracellular rivaroxaban concentration-time profiles (Fig. 3, C and D). The OAT3 $CL_{u,int,T}$ value was determined to be 41.33 $\mu$l/min per $10^6$ of cells (Table 6) and compared well with estimates obtained via a sensitivity analysis–based approach that simulated variations in rivaroxaban's $CL_R$ as a function of OAT3 $CL_{u,int,T}$ and serum creatinine input parameter values. The optimal $CL_{u,int,T}$ for uptake governed by OAT3 (43 $\mu$l/min per $10^6$ of cells) was taken at the intersection of the simulated rivaroxaban $CL_R$ with the observed weighted $CL_R$ of 3.1 l/h at a serum creatinine level of 80 $\mu$mol/l (which corresponds to the simulated GFR value of ~120 ml/min in healthy volunteers) (Supplemental Fig. 4, green plane).

TABLE 2

Comparison of PK parameters between simulated and observed data for model verification of rivaroxaban (20 mg fasted and fed single doses) in healthy subjects

| PK Parameter | Fasted Single Dose (20 mg)[a] | | | | Fed Single Dose (20 mg)[a] | | | |
|---|---|---|---|---|---|---|---|---|
| | Simulated ($n$ = 220) | | Observed ($n$ = 22) | | Simulated ($n$ = 220) | | Observed ($n$ = 22) | |
| | AUC | $C_{max}$ | AUC | $C_{max}$ | AUC | $C_{max}$ | AUC | $C_{max}$ |
| | $\mu g \cdot h/l$ | $\mu g/l$ | $\mu g \cdot h/l$ | $\mu g/l$ | $\mu g \cdot h/l$ | $\mu g/l$ | $\mu g \cdot h/l$ | $\mu g/l$ |
| Geometric mean | 1512 | 111 | 1477 | 160 | 2127 | 234 | 2048 | 281 |
| CV (%) | 67 | 28 | 23 | 34 | 31 | 28 | 23 | 27 |
| Ratio of simulated/observed | 1.02 | 0.69 | | | 1.04 | 0.83 | | |
| Success criteria for ratio of simulated/observed | 0.81–1.23 | 0.74–1.35 | | | 0.81–1.23 | 0.79–1.27 | | |

CV, coefficient of variation.
[a]Stampfuss et al. (2013).

TABLE 3

Comparison of PK parameters between simulated and observed data for model verification of rivaroxaban (10 mg single dose) in healthy subjects

| PK Parameter | Single Dose (10 mg)[a] | | | | | |
|---|---|---|---|---|---|---|
| | Simulated ($n$ = 200) | | | Observed ($n$ = 20) | | |
| | AUC | $C_{max}$ | CL | AUC | $C_{max}$ | CL |
| | *μg·h/l* | *μg/l* | *l/h* | *μg·h/l* | *μg/l* | *l/h* |
| Geometric mean | 1103 | 139 | 9.06 | 892 | 138 | 11.20 |
| CV (%) | 31 | 24 | 41 | 27 | 22 | 27 |
| Ratio of simulated/observed | 1.24 | 1.01 | 0.81 | | | |
| Success criteria for ratio of simulated/observed | 0.78–1.29 | 0.81–1.23 | 0.78–1.29 | | | |

CV, coefficient of variation.
[a]Mueck et al. (2013).

**Concurrent Basolateral Uptake and Apical Efflux Were Necessary to Recapitulate Rivaroxaban's Renal Clearance.** The optimized $CL_{u,int,T}$ value of OAT3-mediated uptake was incorporated into the mechanistic kidney model. In a hypothetical scenario where basolateral OAT3 uptake was present but apical P-gp efflux was disregarded, although simulations managed to recapitulate the observed plasma concentration-time profile of rivaroxaban (Fig. 4B), the amount excreted unchanged in urine remained underestimated (Fig. 4A; Table 7). Hence, our simulations demonstrate that accounting for basolateral uptake in conjunction with apical efflux was crucial in ensuring that simulated plasma concentration-time (Fig. 4B) and urinary excretion rate profiles (Fig. 4A) matched the observed clinical data, with the PK parameters (AUC, $C_{max}$, and $CL_R$) satisfying the prespecified success criteria (Supplemental Material; Table 7 and 8).

**Simulations Using the Mild Renal Impairment Population Adequately Predicted Increases in the Systemic Exposure of Rivaroxaban.** Upon successful verification of the mechanistic kidney model in healthy subjects, which affirmed the accuracy of the drug-dependent parameters defined for rivaroxaban, the ability of the PBPK model to predict the altered PK of rivaroxaban in mild renal impairment was subsequently investigated. With the application of INH, assuming proportional reductions in GFR and tubular secretion, the simulated geometric mean rivaroxaban AUC and $CL_R$ fold changes were 1.20- and 0.54-fold, respectively (Table 9). These point estimates fell within the range of clinical success determined based on the clinically observed AUC and $CL_R$ fold changes of 1.11 and 0.93, respectively (Supplemental Material; Table 9). The modeled plasma-concentration time profiles also reasonably characterized the increase in rivaroxaban's systemic exposure with concomitant mild renal impairment (Fig. 4C).

**PBPK Models of Immediate-Release Verapamil and Norverapamil Recapitulated Clinically Observed PK Profiles.** In the first step of the two-stage in vivo to in vitro correlation framework (Supplemental Fig. 1), using the verified verapamil and norverapamil compound files provided within the Simcyp simulator, simulated PK profiles following a single 80 mg immediate-release dose of verapamil were aligned with the referenced published study by Haeri et al. (2014) (Fig. 5A). Additionally, the model effectively predicted the observed AUC data within the calculated prediction criteria (Supplemental Table 6). This affirms that the in vivo disposition parameters were accurately defined before proceeding with the in vitro to in vivo correlation.

**PBPK Models of Verapamil and Norverapamil Described Absorption Kinetics following Administration of a Sustained-Release Formulation.** In vitro to in vivo correlation convolution was subsequently applied to predict the PK following administration of a single 120 mg dose of controlled-release verapamil based on an initial in vitro dissolution input (Fig. 5B) (Wise, 2000). Simulated and observed plasma concentrations reported by Frishman and Lazar (1992) were compared and the discrepancies prompted iterative refinement of the dissolution parameters to produce an in vivo dissolution profile (Fig. 5B) that adequately described the absorption kinetics following single dose administration of a sustained-release verapamil capsule (Fig. 5C). Accumulation of verapamil following multiple dosing (i.e., 120 mg on day 1, 240 mg on day 2, and 360 mg from day 3 to 10) was also in line with the clinical data (Fig. 5D) (Greenblatt et al., 2018).

## Retrospective Simulations of Enzyme- and Transporter-Mediated DDIs between Rivaroxaban and Verapamil/Ketoconazole

Although preliminary PK simulations verified the predictive potential of the basal compound model of rivaroxaban, given that the PBPK model of rivaroxaban is intended to be applied for the characterization of complex DDIs involving potential enzyme-transporter interplay, it becomes essential to further evaluate its predictive performance against observed DDIs with CYP3A4/2J2 and/or P-gp inhibitors (Shebley et al., 2018).

TABLE 4

Comparison of PK parameters between simulated and observed data for model verification of rivaroxaban (20 mg single dose) in healthy subjects

| PK Parameter | Single Dose (20 mg)[a] | | | | | |
|---|---|---|---|---|---|---|
| | Simulated ($n$ = 130) | | | Observed ($n$ = 13) | | |
| | AUC | $C_{max}$ | CL | AUC | $C_{max}$ | CL |
| | *μg·h/l* | *μg/l* | *l/h* | *μg·h/l* | *μg/l* | *l/h* |
| Geometric mean | 2685 | 266 | 7.45 | 2583 | 263 | 7.92 |
| CV (%) | 40 | 29 | 49 | 21 | 26 | 23 |
| Ratio of simulated/observed | 1.04 | 1.01 | 0.94 | | | |
| Success criteria for ratio of simulated/observed | 0.78–1.29 | 0.74–1.35 | 0.76–1.31 | | | |

CV, coefficient of variation.
[a]Greenblatt et al. (2018).

TABLE 5

$J_{max}$ and $K_m$ values of P-gp–mediated efflux activity and passive permeability of rivaroxaban in MDCK-MDR1 cell monolayers derived from three-compartmental analysis of absorptive transport

*Confidence intervals (95%) are described in brackets. The dashes indicate that values are not applicable for the efined column.*

| Parameter | Absorptive Transport | | |
|---|---|---|---|
| | In Vitro Data (Initial Estimates) | Nelder-Mead | Hybrid |
| $J_{max}$ (pmol/min) | 97.98[a] | 37.83 (24.3, 51.4) | 41.63 (26.2, 57.1) |
| $K_m$ ($\mu$M) | 836.80[a] | 9.42 (7.0, 11.8) | 12.36 (8.9, 15.8) |
| $P_{pass}$ ($\times 10^{-6}$ cm/s) | 6.37[b] | 12.88 (9.8, 15.9) | 12.48 (9.5, 15.4) |
| $R^2$ | — | 0.97 | 0.97 |
| AIC | — | 49.80 | 59.47 |
| $AIC_c$ | — | 50.82 | 60.40 |

AIC, Akaike information criterion; $AIC_c$, Akaike information criterion corrected.
[a]The apparent $J_{max}$ and $K_m$ values were derived from conventional Michaelis Menten analysis.
[b]The $P_{pass}$ values were determined from inhibition of the in vitro apparent permeability measured in the absorptive direction in the presence of 100 $\mu$M of verapamil.

**DDDIs between Rivaroxaban and Verapamil Were Successfully Modeled.** The capability of verapamil and its major metabolite norverapamil to elicit both mechanism-based inactivation (MBI) as well as reversible inhibition of CYP3A4 has been established previously (Orr et al., 2012). Nevertheless, in our study, the in vitro inhibitory parameters (i.e., $k_{inact}$: the theoretical maximum inactivation rate constant at infinite inactivator concentration; $K_I$: the inactivator concentration yielding an inactivation rate at one-half of $k_{inact}$; and $K_i$: the equilibrium dissociation constant for the enzyme inhibitor complex) were quantified using rivaroxaban as the probe substrate.

Collectively, the in vitro inhibition studies affirmed the MBI (Supplemental Fig. 5, A–D) and reversible inhibition (Supplemental Fig. 6, A–D) of CYP3A4-mediated metabolism of rivaroxaban by verapamil and norverapamil. A summary of the in vitro inhibition parameters derived is presented in Table 10. Conversely, our preliminary studies suggest the absence of MBI of CYP2J2 by verapamil and norverapamil (Supplemental Fig. 5, E and F). Similarly, reversible inhibition by verapamil and norverapamil against CYP2J2 yielded large $K_i$ values of 12.2 and 161.8 $\mu$M, respectively (Supplemental Fig. 6, E–H). The $R_1$ ratios (Table 10) were both less than the threshold of 1.02

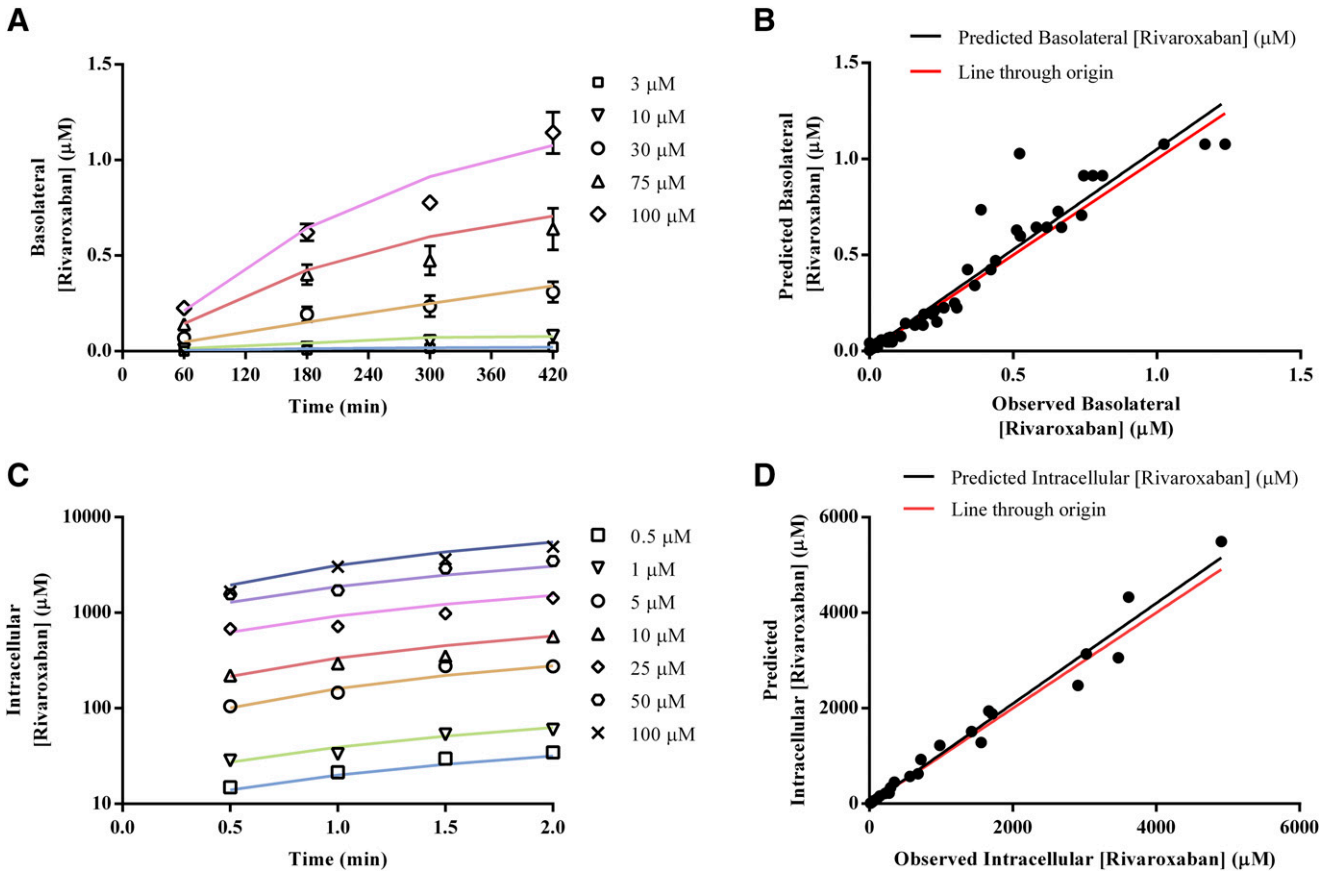


**Fig. 3.** In vitro investigation of the P-gp–mediated and OAT3-mediated transport kinetics of rivaroxaban. For efflux kinetics, time- and concentration-dependent data in the absorptive direction were analyzed via mechanistic three-compartmental modeling. Goodness of fit between experimentally measured (symbols) and simulated (solid lines) basolateral rivaroxaban concentrations is presented in (A and B). For uptake kinetics, time- and concentration-dependent rivaroxaban uptake into OAT3-transfected human embryonic kidney cells was analyzed via mechanistic two-compartmental modeling. Goodness of fit between experimentally measured (symbols) and simulated (solid lines) intracellular rivaroxaban concentrations is presented in (C and D).

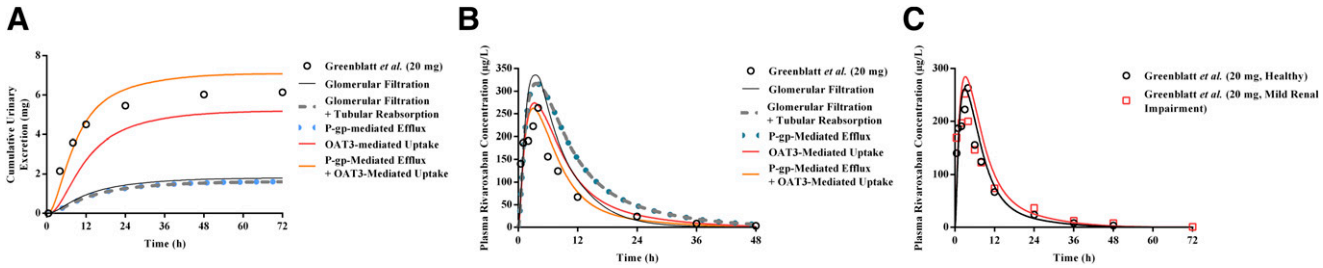


**Fig. 4.** Development of the mechanistic kidney model (MechKiM) for simulation of rivaroxaban PK in healthy and renal-impaired patients. Simulated cumulative urinary excretion of rivaroxaban (A) and its corresponding plasma concentration-time profile (B) using MechKiM following a single 20 mg dose. Accounting for glomerular filtration (black solid line), glomerular filtration, and reabsorption (gray dashed line); glomerular filtration, reabsorption, and apical P-gp–mediated active efflux (blue dotted line); as well as glomerular filtration, reabsorption, and basolateral OAT3-mediated uptake (red line) were unsuccessful in recapitulating observed clinical profiles (open circles). Recapitulation of observed clinical plasma rivaroxaban concentrations and urinary excretion data required the consideration of basolateral uptake in tandem with apical efflux (orange line). Upon verification of the drug-dependent parameters within the MechKiM model, adjustment of system parameters (glomerular filtration and PTCPGK) allowed accurate prediction of the increase in rivaroxaban's systemic exposure in mild renal impairment (C). Open symbols represent clinical data.

recommended by the Food and Drug Administration, hence eliminating the need for further assessment of DDI potential.

Notably, despite a previous in vitro study demonstrating an inhibitory effect of verapamil against the P-gp–mediated efflux of rivaroxaban (Table 10) (Gnoth et al., 2011), the in vivo data revealed that the amount of rivaroxaban excreted unchanged in urine was elevated in the presence of verapamil (Greenblatt et al., 2018). This in vitro to in vivo disconnect alluded to the negligible role of transporters in perpetrating the eventual DDI between rivaroxaban and verapamil. Subsequent assimilation of the derived CYP3A4 inhibitory parameters into the PBPK-DDI model accurately recapitulated the observed DDI magnitude (Fig. 6A) and the increase in $CL_R$ (Fig. 6B). The simulated geometric mean (90% confidence interval) AUC and CL ratios of 1.46 (1.33, 1.61) and 0.68 (0.62, 0.75) were within the range of acceptable performance calculated based on the clinically observed AUC and CL fold changes of rivaroxaban in the presence of verapamil (Table 11). In patients with underlying mild renal impairment, verapamil coadministration resulted in simulated geometric mean AUC and CL fold changes of 1.70 and 0.59, respectively, meeting the success criteria defined in Table 12, hence attesting to the ability of the PBPK-DDI model to accurately recapitulate an enzymatic DDDI scenario (Fig. 6C).

**Extent of DDIs between Rivaroxaban and Ketoconazole Was Underestimated Despite Consideration of CYP3A4, CYP2J2, and P-gp Inhibition.** In vitro investigations verified the inhibition of CYP3A4 and CYP2J2-mediated metabolism as well as P-gp–mediated efflux of rivaroxaban with coadministration of ketoconazole (Supplemental Fig. 7, A–F). The simulated fold reduction in hepatic CL met the success criteria delineated in Table 13, reliably supporting conclusions that the extent of enzyme-mediated DDI was accurately reproduced. Nevertheless, as illustrated in Fig. 6D (blue solid line), the modeled plasma concentration-time profile in the presence of ketoconazole evidently demonstrated an underestimation of DDI magnitude. Moreover, the PK parameters (AUC, $C_{max}$, and $CL_R$) fell outside the prespecified acceptance criteria (Table 13), suggesting that the nature and potency of transporter-mediated interactions between rivaroxaban and ketoconazole have not been adequately elucidated. The results of a subsequent sensitivity analysis (Supplemental Fig. 8A) corroborated this postulation and demonstrated that the sole inhibition of P-gp–mediated efflux is unlikely to substantially affect rivaroxaban's systemic exposure. In contrast, the AUC fold change was highly sensitive to inhibition of OAT3-mediated basolateral uptake. In vitro inhibition experiments further established inhibition of OAT3-mediated uptake by ketoconazole ($IC_{50}$ = 15.77 $\mu$M) (Supplemental Fig. 7G). Nevertheless, direct incorporation of the measured in vitro $K_i$ was unable to recapitulate the clinically observed DDI magnitude (data not shown) and further optimization of the $K_i$ value of ketoconazole to 0.01 $\mu$M was eventually required (Fig. 6D, blue dashed line; Supplemental Material; Table 14).

TABLE 6

Intrinsic OAT3-mediated uptake clearance of rivaroxaban in OAT3-transfected HEK cells derived from two-compartmental analysis of uptake transport. The dashes indicate that values are not applicable for the defined column.

*Confidence intervals (95%) are described in brackets.*

| Parameter | Uptake Transport | | |
|---|---|---|---|
| | In Vitro Data (Initial Estimates) | Nelder-Mead | Hybrid |
| $CL_{int,T}$ ($\mu$l/min per $10^6$ cells)[a] | 33.91 | 41.33 (40.18, 42.47) | — |
| $CL_{PD}$ ($\mu$l/min per $10^6$ cells)[b] | $1.09 \times 10^{-5}$ (Fixed) | | |
| $R^2$ | | 0.97 | — |
| AIC | | −16.92 | — |
| $AIC_c$ | | −16.44 | — |

AIC, Akaike information criterion; $AIC_c$, Akaike information criterion corrected.

[a]The $CL_{int,T}$ estimates were derived from the conventional two-step approach (Supplemental Fig. 2).

[b]Fixed using the $CL_{PD}$ value estimated from $P_{pass} = 12.88 \times 10^{-6}$ cm/s using eq. 3 since large S.E. values have been observed with $CL_{PD}$ values estimated using 2-minute incubations (Ménochet et al., 2012).

## Discussion

In the United States, 30%–50% of adverse drug reactions are due to dosing errors (Neely, 2017), largely implicating vulnerable populations that incidentally constitute the exclusion criteria of pivotal clinical trials (Darwich et al., 2017). PBPK modeling has proven to be a panacea for the perennial challenge of suboptimal therapeutic outcomes in such complex and untested, albeit clinically relevant scenarios. Its unique ability to quantitatively integrate the multitude of drug- and system-dependent parameters that can influence an individual's dose response has guided refined dosing in multiple clinical applications, particularly involving DDIs and special populations (Sager et al., 2015; Jamei, 2016).

Using PBPK modeling, Grillo et al. (2012) predicted clinically significant increases in rivaroxaban exposure due to renal impairment and moderate CYP3A4/P-gp inhibition by erythromycin. The findings informed current product labeling where concomitant use of rivaroxaban with a combined weak to moderate inhibitor of CYP3A4 and an inhibitor of P-gp and/or breast cancer resistance protein should be avoided under any degree of renal impairment. Given that such cautionary language

TABLE 7

Comparison of PK parameters between simulated and observed data for model verification of the mechanistic kidney model of rivaroxaban after a 20 mg single dose in healthy subjects

*Healthy controls are defined as having creatinine clearance > 80 ml/min.*

| PK Parameter | Single Dose (20 mg) | | | | | |
|---|---|---|---|---|---|---|
| | Simulated ($n$ = 130) | | | Observed ($n$ = 13) | | |
| | AUC | $C_{max}$ | $CL_R$ | AUC | $C_{max}$ | $CL_R$ |
| | *μg·h/l* | *μg/l* | *l/h* | *μg·h/l* | *μg/l* | *l/h* |
| Healthy, P-gp only[a] | | | | | | |
| Geometric mean | 3901 | 311 | 0.37 | 2583 | 263 | 2.42 |
| CV (%) | 52 | 31 | 27 | 21 | 26 | 23 |
| Ratio of simulated/observed | 1.51 | 1.18 | 0.15 | | | |
| Success criteria for ratio of simulated/observed | 0.78–1.29 | 0.74–1.35 | 0.76–1.31 | | | |
| Healthy, OAT3 only[a] | | | | | | |
| Geometric mean | 2946 | 269 | 1.60 | 2583 | 263 | 2.42 |
| CV (%) | 45 | 30 | 46 | 21 | 26 | 23 |
| Ratio of simulated/observed | 1.14 | 1.02 | 0.66 | | | |
| Success criteria for ratio of simulated/observed | 0.78–1.29 | 0.74–1.35 | 0.76–1.31 | | | |
| Healthy, P-gp, and OAT3[a] | | | | | | |
| Geometric mean | 2563 | 263 | 2.70 | 2583 | 263 | 2.42 |
| CV (%) | 43 | 30 | 49 | 21 | 26 | 23 |
| Ratio of simulated/observed | 0.99 | 1 | 1.12 | | | |
| Success criteria for ratio of simulated/observed | 0.78–1.29 | 0.74–1.35 | 0.76–1.31 | | | |

CI, confidence interval; CV, coefficient of variation.
[a]Greenblatt et al. (2018).

hampers the utility of relevant drug combinations in AF management, Ismail et al. (2018) proposed dosing modifications in renal impairment and concomitant verapamil administration via correlating PBPK-predicted increases in rivaroxaban exposure with bleeding risk outcomes. Finally, Xu et al. (2018) interrogated the exacerbation of rivaroxaban DDIs by hepatic dysfunction.

Prior to application, a PBPK model must be qualified as fit for purpose (Shebley et al., 2018) (Fig. 1). The four principal aspects essential for robust model qualification are, namely, 1) evaluating model relevance to research context; 2) assessing sources of uncertainty and implications; 3) capturing known variabilities in clinical outcomes; and 4) ensuring that model results are qualitatively and quantitatively consistent with test data (Friedrich, 2016). Fulfilling the third and fourth criteria of the aforementioned aspects, our developed models demonstrated qualitative and quantitative reproduction of rivaroxaban's essential clinical PK characteristics, such as rapid and near complete oral absorption, dose proportional increases in rivaroxaban exposure under fed conditions (Fig. 2, B and C), lack of accumulation upon multiple dosing (Kubitza et al., 2005a,b; Zhao et al., 2009), and true representation of interindividual variability (Jamei et al., 2009; US Food and Drug Administration, 2011a). Nevertheless, the intended application of the PBPK model of rivaroxaban to the interrogation of DDIs importantly entails that the first and second criteria are also adequately satisfied. Ensuring that the model scope is sufficiently mechanistic in delineating 1) the renal disposition of rivaroxaban and 2) inhibition of the metabolic/transport pathways of rivaroxaban elimination is required to facilitate rigorous identification and assessment of biologic uncertainties that may result in incongruities between predictions and actual outcomes.

Our PBPK model is novel and mechanistically detailed in parameterizing the renal disposition of rivaroxaban. Previously, its $CL_R$ value was defined as a function of glomerular filtration and net secretion (calculated as the difference between absolute secretion and absolute reabsorption) (Grillo et al., 2012; Ismail et al., 2018; Xu et al., 2018). Conflating these distinct processes precludes mechanistic characterization of their differential contributions to the $CL_R$ value of rivaroxaban. Additionally, by ascribing renal elimination of rivaroxaban to the apparent plasma compartment (i.e., minimal PBPK model), both Grillo et al. (2012) and Ismail et al. (2018) were unable to predict urinary excretion data for direct assessment of model-predicted $CL_R$. The

TABLE 8

Comparison of PK parameters between simulated and observed data for model verification of the mechanistic kidney model of rivaroxaban after a 10 mg single dose in healthy subjects

*Healthy controls are defined as having creatinine clearance > 80 ml/min*

| PK Parameter | Single Dose (10 mg), Healthy, P-gp, and OAT3[a] | | | | | |
|---|---|---|---|---|---|---|
| | Simulated ($n$ = 200) | | | Observed ($n$ = 20) | | |
| | AUC | $C_{max}$ | $CL_R$ | AUC | $C_{max}$ | $CL_R$ |
| | *μg·h/l* | *μg/l* | *l/h* | *μg·h/l* | *μg/l* | *l/h* |
| Geometric mean | 1060 | 120 | 3.05 | 892 | 138 | 2.5 |
| CV (%) | 40 | 29 | 55 | 27 | 22 | 26 |
| Ratio of simulated/observed | 1.19 | 0.87 | 1.22 | | | |
| Success criteria for ratio of simulated/observed | 0.78–1.29 | 0.81–1.23 | 0.78–1.28 | | | |

CI, confidence interval; CV, coefficient of variation.
[a]Mueck et al. (2013).

TABLE 9

Comparison of PK parameters between simulated and observed data for model verification of the mechanistic kidney model of rivaroxaban after a 20 mg single dose in renal impaired patients

*Healthy controls are defined as having creatinine clearance > 80 ml/min; mild renal impairment is defined as having creatinine clearance of 50–79 ml/min.*

| PK Parameter | Single Dose (20 mg), Mild Renal Impairment[a] | | | | | |
|---|---|---|---|---|---|---|
| | Simulated ($n$ = 140) | | | Observed ($n$ = 14) | | |
| | AUC | $C_{max}$ | $CL_R$ | AUC | $C_{max}$ | $CL_R$ |
| | *μg·h/l* | *μg/l* | *l/h* | *μg·h/l* | *μg/l* | *l/h* |
| Geometric mean | 2899 | 279 | 1.46 | 2864 | 252 | 2.25 |
| CV (%) | 43 | 29 | 50 | 29 | 29 | 42 |
| Ratio of simulated/observed | 1.01 | 1.11 | 0.65 | | | |
| Success criteria for ratio of simulated/observed | 0.72–1.38 | 0.72–1.38 | 0.63–1.58 | | | |
| Fold change vs. healthy (90% CI)[b] | 1.20 (1.09, 1.31) | | 0.54 (0.49, 0.60) | 1.11 | | 0.93 - |
| Success criteria for simulated fold change | 0.80–1.81 | | 0.30–1.03 | | | |

CI, confidence interval; CV, coefficient of variation.
[a]Greenblatt et al. (2018).
[b]PK parameters in healthy controls used for comparison were obtained from simulations where the mechanistic kidney model incorporating both P-gp and OAT-3 was used to simulate the plasma concentration-time profile of rivaroxaban after a single 20 mg dose.

significance of such mechanistic detail is further underscored with in vitro evidence demonstrating how consideration of P-gp–mediated efflux and passive permeability produced adequate fits for high-permeability compounds (e.g., amprenavir and quinidine) but not for low-permeability substrates (e.g., loperamide and digoxin) (Acharya et al., 2008). For loperamide and digoxin, the observed efflux kinetics were substantially greater than could be fitted by passive permeability alone and improvement in fitting outcomes was contingent on the addition of a basolateral uptake transporter (Acharya et al., 2008). Consistently, evaluating the extent of passive permeability becomes diagnostic for the kinetic necessity of basolateral uptake (Lumen et al., 2013; Huang and Isoherranen, 2018). In this study, incorporating passive permeability ($P_{pass}$ = 12.88 × $10^{-6}$ cm/s) (Table 5) estimates from three-compartment modeling yielded a $CL_{PD}$ value of 1.09 × $10^{-5}$ μl/min per $10^6$ of cells when scaled using the tubular surface area. When considered in tandem with P-gp efflux kinetics (Table 5), the clinically observed $CL_R$ value of rivaroxaban remained underestimated by our simulation (Fig. 4A). Nevertheless, without independent verification

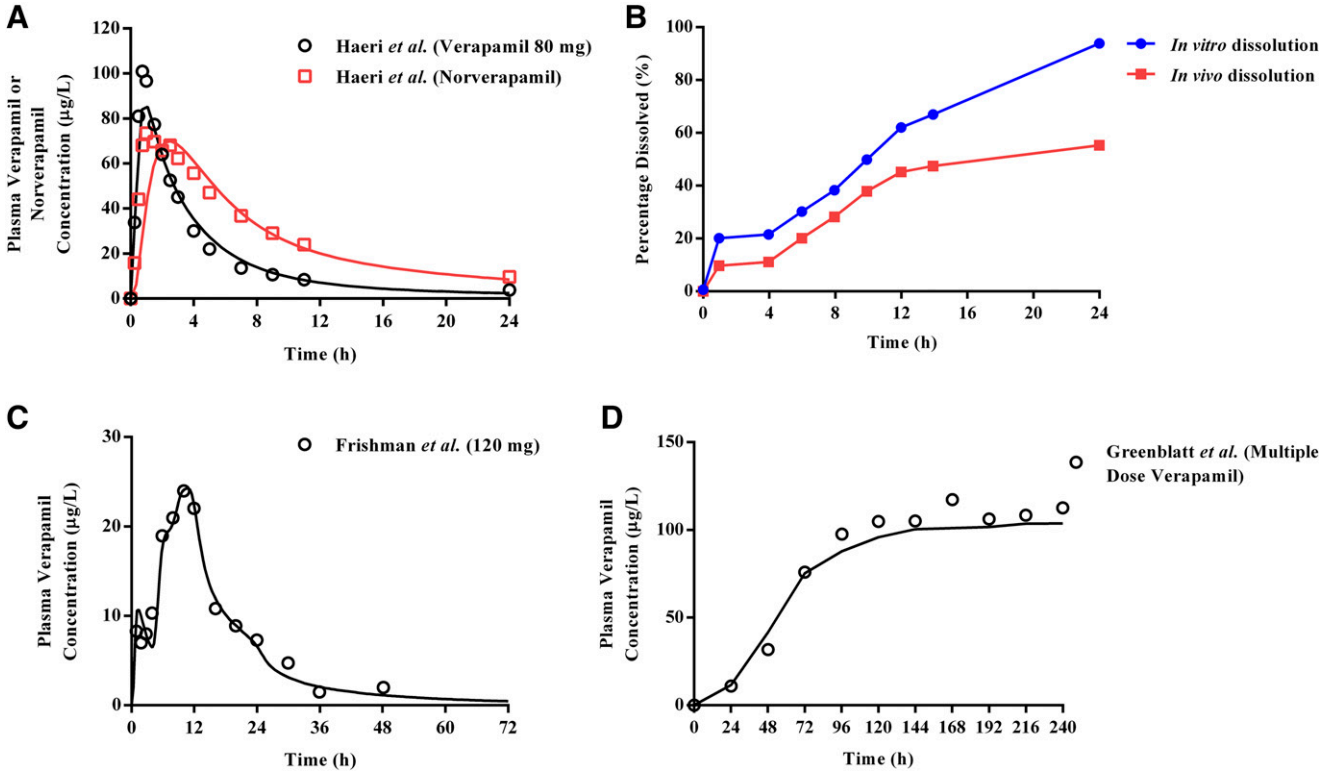


**Fig. 5.** Simulated pharmacokinetic profiles of verapamil and its major metabolite norverapamil. (A) Simulated plasma concentration-time profiles of 80 mg immediate-release verapamil and norverapamil in healthy volunteers verified the basal PBPK model of verapamil provided within Simcyp. (B) In vivo to in vitro correlation convolution using the reported in vitro dissolution profile of a controlled-release capsule was unable to recapitulate clinically observed plasma concentration-time profiles following a single 120 mg dose. Iterative refinement of the dissolution parameters yielded an in vivo dissolution profile (B) that adequately described absorption kinetics after single (C) and multiple (D) dosing based on the administration schedule delineated by Greenblatt et al. (2018). Open symbols represent clinical data while solid lines depict simulations.

TABLE 10

Summary of CYP450,P-gp and OAT3 inhibition parameters with rivaroxaban as the probe substrate. The dashes indicate that values are not applicable for the defined column.

| In Vitro Parameter | Verapamil | Norverapamil | Ketoconazole |
|---|---|---|---|
| MBI of CYP3A4 | | | |
| $K_I$ ($\mu$M) | 1.65 | 0.28 | — |
| $k_{inact}$ ($h^{-1}$) | 3.92 | 2.44 | — |
| $k_{inact}/K_I$ ($h^{-1}/\mu M^{-1}$) | 2.38 | 8.59 | — |
| Reversible inhibition of CYP3A4 | | | |
| Mode | Mixed | Mixed | Mixed |
| $K_i$ ($\mu$M) | 0.487 | 0.270 | 0.094 |
| $\alpha$ | 1.19 | 1.15 | 3.28 |
| Reversible inhibition of CYP2J2 | | | |
| Mode | Competitive | Competitive | Competitive |
| $K_i$ ($\mu$M) | 12.2 | 162 | 0.082 |
| $\alpha$ | — | — | — |
| $R_1^a$ | 1.00 | 1.00 | |
| Fraction unbound in the in vitro incubation | | | |
| $f_{u,inc}$ | 0.67 | 0.78 | 1 |
| Inhibition of P-gp | | | |
| $IC_{50}$ ($\mu$M) | 4.3[b] | — | 0.22 |
| Inhibition of OAT3 | | | |
| $IC_{50}$ ($\mu$M) | — | — | 15.77 |

$f_{u,inc}$, fraction unbound in the in vitro incubation; $R_1$, predicted ratio of the victim drug's area under the plasma concentration-time curve in the presence and absence of an inhibitor for basic models of reversible inhibition.

[a] $R_1 = 1 + (I_{max,u}/K_i)$, where $I_{max,u}$ is the maximal unbound plasma concentration of the interacting drug.

[b] The $IC_{50}$ value of verapamil on the P-gp–mediated efflux of rivaroxaban (1 $\mu$M) across L-MDR1 cells after 2-hour incubation at 37°C (Gnoth et al., 2011).

of specific model assumptions governing passive diffusion clearance in the kidneys, it is inevitable that certainty in the quantitative contribution of active transport to renal clearance remains low and is interdependent on the error in predicted diffusion clearance (Huang and Isoherranen, 2018). Hence, using a 35-compartment mechanistic kidney model developed by Huang and Isoherranen (2018), where in vitro to in vivo predictions of renal clearance using plasma unbound fraction and permeability data have been systematically verified for a set of 46 compounds, we demonstrate that renal clearance predicted via the mechanistic kidney model in the Simcyp simulator was within 2-fold of that simulated using the 35-compartment model when a $P_{pass}$ value of $12.88 \times 10^{-6}$ cm/s

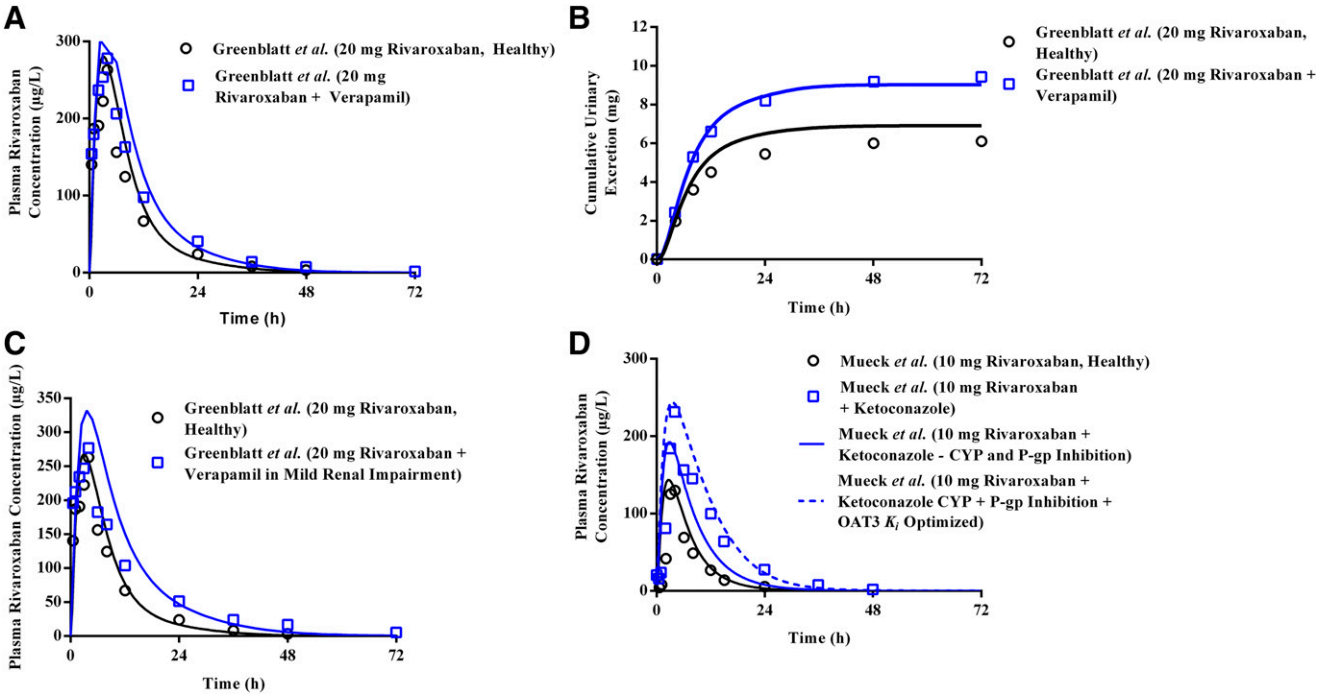


**Fig. 6.** Predicted DDIs between rivaroxaban and verapamil or ketoconazole in healthy and renal-impaired patients. Simulated mean plasma concentration-time profiles of (A) 20 mg rivaroxaban in the absence and presence of CYP3A4 inhibitor verapamil demonstrated accurate estimation of DDI magnitude, including (B) an increase in the cumulative urinary excretion of rivaroxaban with verapamil coadministration. (C) Mild renal impairment potentiated the extent of DDI between rivaroxaban and verapamil. (D) Consideration of the inhibitory potential of ketoconazole on CYP3A4/2J2-mediated metabolism and P-gp–mediated efflux of rivaroxaban underestimated the observed DDI magnitude (blue solid line). Optimization of the $K_i$ value of ketoconazole against OAT3-mediated rivaroxaban uptake was required to accurately recapitulate the clinically observed DDI (blue dashed line). Open symbols represent clinical data.

TABLE 11

Simulated change in rivaroxaban PK parameters in the presence of drug-drug interactions with verapamil

| PK Parameter | Rivaroxaban (20 mg) and Verapamil[a] | | | | | |
|---|---|---|---|---|---|---|
| | Simulated ($n$ = 100) | | | Observed ($n$ = 10) | | |
| | AUC | $C_{max}$ | CL | AUC | $C_{max}$ | CL |
| | *μg·h/l* | *μg/l* | *l/h* | *μg·h/l* | *μg/l* | *l/h* |
| Geometric mean | 3488 | 314 | 5.73 | 3600 | 278 | 5.70 |
| CV (%) | 43 | 28 | 56 | 20 | 27 | 22 |
| Ratio of simulated/observed | 0.97 | 1.13 | 1.01 | | | |
| Success criteria for ratio of simulated/observed | 0.77–1.31 | 0.70–1.43 | 0.75–1.34 | | | |
| Fold change (90% CI) [b] | 1.46 (1.33, 1.61) | | 0.68 (0.62, 0.75) | 1.39 | | 0.72 |
| Success criteria for simulated fold change | 0.94–2.05 | | 0.45–1.04 | | | 2 |
| | | | 0.45–1.04 | | | |

CV, coefficient of variation.
[a]Greenblatt et al. (2018).
[b]PK parameters in healthy controls used for calculation of fold changes were obtained from simulations where the mechanistic kidney model incorporating both P-gp and OAT-3 was used to simulate the plasma concentration-time profile of rivaroxaban after a 20 mg dose (Table 7).

was incorporated (Supplemental Table 8), verifying the passive diffusion component of the mechanistic kidney model constructed for rivaroxaban in this study.

With a verified passive diffusion process, the inability to recapitulate the $CL_R$ value of rivaroxaban can be thus confidently attributed to the presence of knowledge gaps in transporter-mediated clearance that impose constraints on the exclusive utilization of bottom-up approaches. In such scenarios, the utility of a middle-out approach has received increasing recognition (Rostami-Hodjegan, 2018). Using reverse translational modeling, clinical data of rivaroxaban obtained with coadministration of ketoconazole revealed surprising fold reductions in $V_d$/F (0.53) in addition to CL/F (0.39), such that the half-life was minimally affected (US Food and Drug Administration, 2011a). Coupled with experimental demonstration of rivaroxaban uptake in human OAT3-expressing cells, the convergence of evidences reinforces the plausibility of our postulated renal basolateral uptake process. Sensitivity analyses in this study further underscored the relative insensitivity of the observed $CL_R$ to the P-gp relative expression factor (Supplemental Fig. 8B) and confirmed that the sole inhibition of P-gp–mediated efflux is unlikely to produce significant increases in rivaroxaban's systemic exposure (Fig. 6D; Supplemental Fig. 8A). Hence, it becomes apparent that reliable quantitative extrapolation of in vitro–derived OAT3-mediated values of $J_{max}$ and $K_m$ is essential to accurately define the renal excretion of rivaroxaban. With the emergence of quantitative transporter abundance data in kidney samples (reported OAT3 abundance of 3.5 ± 1.6 pmol/mg of total membrane protein) (Prasad et al., 2016), IVIVE scaling factors can be accurately determined, removing the need for top-down optimization (Supplemental Fig. 4), where estimates of OAT3 $CL_{u,int}$ may be biased based on the mean $CL_R$ and serum creatinine parameters defined.

Acknowledging the pivotal role of basolateral uptake in mediating the renal disposition of rivaroxaban enables informed analysis of the likelihood of observing transporter-mediated DDIs with rivaroxaban. A case in point would be verapamil, a known P-gp inhibitor that demonstrated in vitro inhibition of rivaroxaban's efflux in L-MDR1 cells (Gnoth et al., 2011; US Food and Drug Administration, 2017). However, concomitant verapamil administration did not result in a significant decrease in rivaroxaban's renal clearance, as highlighted in the DDI study by Greenblatt et al. (2018). This observation is substantiated by verapamil having a high mouse OAT3 $K_i$ value of 31 μM (Ahn et al., 2009). Consistently, our in vitro experiments also demonstrated negligible inhibition of OAT3-mediated uptake of rivaroxaban by verapamil up to 100 μM (Supplemental Fig. 7H). Furthermore, examining the drugs that have been shown to produce significant transporter-mediated DDIs with rivaroxaban (i.e., ketoconazole and ritonavir) (Mueck et al., 2013) revealed in vitro evidence of OAT3 inhibition. Both ketoconazole and ritonavir inhibit estrone sulfate transport in transfected human embryonic kidney/OAT3 cell lines ($IC_{50}$ = 0.86 and 8.1 μM for ketoconazole and ritonavir, respectively) (Vermeer et al., 2016; Shebley et al., 2017). When rivaroxaban was used as the probe substrate in this study, uptake inhibition by ketoconazole was also observed (Supplemental Fig. 7G). Nevertheless, further

TABLE 12

Simulated change in rivaroxaban PK parameters in the presence of drug-drug-disease interactions with verapamil

Mild renal impairment is defined as having creatinine clearance of 50–79 ml/min.

| PK Parameter | Rivaroxaban (20 mg) and Verapamil in Mild Renal Impairment[a] | | | | | |
|---|---|---|---|---|---|---|
| | Simulated ($n$ = 110) | | | Observed ($n$ = 11) | | |
| | AUC | $C_{max}$ | CL | AUC | $C_{max}$ | CL |
| | *μg·h/l* | *μg/l* | *l/h* | *μg·h/l* | *μg/l* | *l/h* |
| Geometric mean | 4057 | 327 | 4.93 | 4093 | 267 | 5.04 |
| CV (%) | 41 | 27 | 73 | 29 | 29 | 26 |
| Ratio of simulated/observed | 0.99 | 1.22 | 0.98 | | | |
| Success criteria for ratio of simulated/observed | 0.69–1.44 | 0.60–1.44 | 0.72–1.39 | | | |
| Fold change (90% CI)[b] | 1.70 (1.54, 1.87) | | 0.59 (0.53, 0.65) | 1.58 | | 0.64 |
| Success criteria for simulated fold change | 0.97–2.57 | | 0.40–1.01 | | | |

CV, coefficient of variation.
[a]Greenblatt et al. (2018).

TABLE 13

Simulated change in rivaroxaban PK parameters in the presence of drug-drug interactions with ketoconazole incorporating apical efflux inhibition

| PK Parameter | Rivaroxaban (10 mg) and Ketoconazole[a] | | | | | | | |
|---|---|---|---|---|---|---|---|---|
| | Simulated ($n$ = 200) | | | | Observed ($n$ = 20) | | | |
| | AUC | $C_{max}$ | $CL_H$ | $CL_R$ | AUC | $C_{max}$ | $CL_H^b$ | $CL_R$ |
| | $\mu g \cdot h/l$ | $\mu g/l$ | $l/h$ | $l/h$ | $\mu g \cdot h/l$ | $\mu g/l$ | $l/h$ | $l/h$ |
| Geometric mean | 1676 | 189 | 2.66 | 3.05 | 2298 | 237 | 2.75 | 1.60 |
| CV (%) | 39 | 23 | 38 | 54 | 26 | 20 | 26 | 33 |
| Ratio of simulated/observed | 0.73 | 0.80 | 0.97 | 1.91 | | | | |
| Success criteria for ratio of simulated/observed | 0.78–1.28 | 0.83–1.21 | 0.78–1.28 | 0.74–1.36 | | | | |
| Fold change (90% CI)[c] | 1.56 (1.46, 1.66) | | 0.45 (0.42, 0.49) | 1.01 (0.92, 1.09) | 2.58 | | 0.32 | 0.64 |
| Success criteria for simulated fold change | 1.48–4.50 | | 0.17–0.58 | 0.38–1.07 | | | | |

$CL_H$, hepatic clearance; CV, coefficient of variation.
[a]Mueck et al. (2013).
[b]$CL_H$ calculated from ($CL/F - CL_R$) assuming F = 1 since rivaroxaban is known to have high absolute bioavailability (80%–100%) for the 10 mg dose (Mueck et al., 2013).
[c]PK parameters in healthy controls used for calculation of fold changes were obtained from simulations where the mechanistic kidney model Incorporating both P-gp and OAT-3 was used to simulate the plasma concentration time profile of rivaroxaban after a 10 mg dose (Table 8).

optimization of the $K_i$ value of ketoconazole was required to recapitulate the clinically observed DDI magnitude (Fig. 6D; Tables 11–14). Our observed underprediction in transporter $K_i$ remains aligned with previous attempts to recapitulate transporter-mediated DDIs for solute carriers (Hsu *et al.*, 2014; Burt *et al.*, 2016). Such incongruity may reflect the incorrect assumption of a competitive mode of inhibition. Additionally, although the assumed concentration for inhibition (that added to the incubation media) should be largely consistent with that at the transporter binding site, the lipophilic nature of ketoconazole could have resulted in nonspecific binding processes both in vitro and in vivo, further confounding interpretation of the inhibition data. Given that drugs likely to be coadministered with rivaroxaban have been reported to be P-gp inhibitors with unknown effects on OAT3-mediated uptake (e.g., amiodarone), elucidating the dynamic interplay between apical P-gp efflux and basolateral OAT3 uptake using alternative approaches such as double-transfected cell lines with rivaroxaban as the probe substrate becomes imperative.

Our second novelty lies in our adoption of rivaroxaban as the probe substrate when quantifying inhibition of metabolic and/or transport processes by verapamil and ketoconazole. In the previous PBPK-DDI model developed by Grillo et al. (2012), a $K_i$ value of 11 $\mu$M derived from an in vitro study using digoxin as the substrate was used to describe the inhibitory potential of erythromycin on the P-gp–mediated efflux of rivaroxaban. However, Gnoth et al. (2011) reported that the directed efflux of rivaroxaban across P-gp–overexpressing L-MDR1 cells was unaffected by erythromycin. A clinical DDI study by Moore et al. (2014) further demonstrated negligible inhibition of the active renal secretion of rivaroxaban by erythromycin, underscoring how the nature and potency of DDIs are often unique to each substrate-inhibitor pair. This probe substrate specificity was similarly reflected in our in vitro experiments. For instance, verapamil has been reported to exhibit reversible inhibition against CYP2J2 when index substrates were used (Lee et al., 2012; Ren et al., 2013), but yielded minimal inhibition against CYP2J2-mediated metabolism of rivaroxaban (Supplemental Fig. 6, E–H; Table 10). Additionally, the in vitro MBI potencies of verapamil and norverapamil against CYP3A4 using index substrates were less potent ($k_{inact}/K_I$ ratio of 0.9 and 1.74 $h^{-1}/\mu M^{-1}$, respectively) than our experimentally derived parameters when rivaroxaban was used as the probe substrate ($k_{inact}/K_I$ ratio of 2.37 and 8.59 $h^{-1}/\mu M^{-1}$, respectively) (Supplemental Table 7). Finally, the in vitro reversible inhibition potency of ketoconazole against CYP3A4 using the index substrate was more potent ($K_i$ value of 0.015 $\mu$M) than our experimentally measured potency using rivaroxaban as the substrate ($K_i$ value of 0.094 $\mu$M) (Supplemental Table 7). Hence, it is evident that accurate recapitulation of enzyme- and transporter-mediated DDIs involving rivaroxaban is contingent on generating reliable in vitro inhibitory estimates for parameterization of the PBPK-DDI model.

The future intended application of the current PBPK model of rivaroxaban is in extrapolation to untested scenarios implicating both enzyme- and transporter-mediated DDDIs. Assuming the INH and

TABLE 14

Simulated change in rivaroxaban PK parameters in the presence of drug-drug interactions with ketoconazole incorporating both basolateral uptake and apical efflux inhibition

| PK Parameter | Rivaroxaban (10 mg) and Ketoconazole (OAT3 $K_i$ Optimized)[a] | | | | | | | |
|---|---|---|---|---|---|---|---|---|
| | Simulated ($n$ = 200) | | | | Observed ($n$ = 20) | | | |
| | AUC | $C_{max}$ | $CL_H$ | $CL_R$ | AUC | $C_{max}$ | $CL_H^b$ | $CL_R$ |
| | $\mu g \cdot h/l$ | $\mu g/l$ | $l/h$ | $l/h$ | $\mu g \cdot h/l$ | $\mu g/l$ | $l/h$ | $l/h$ |
| Geometric mean | 2850 | 241 | 2.70 | 0.81 | 2298 | 237 | 2.75 | 1.60 |
| CV (%) | 35 | 21 | 36 | 30 | 26 | 20 | 26 | 33 |
| Ratio of simulated/observed | 1.24 | 1.02 | 0.98 | 0.51 | | | | |
| Success criteria for ratio of simulated/observed | 0.78–1.28 | 0.83–1.21 | 0.78–1.28 | 0.74–1.36 | | | | |
| Fold change (90% CI)[c] | 2.65 (2.49, 2.82) | | 0.44 (0.41, 0.48) | 0.27 (0.25, 0.29) | 2.58 | | 0.32 | 0.64 |
| Success criteria for simulated fold change | 1.48–4.50 | | 0.17–0.58 | 0.38–1.07 | | | | |

$CL_H$, hepatic clearance; CV, coefficient of variation.
[a]Mueck et al. (2013).
[b]$CL_H$ calculated from ($CL/F - CL_R$) assuming F = 1 since rivaroxaban is known to have high absolute bioavailability (80%–100%) for the 10 mg dose (Mueck et al., 2013).
[c]PK parameters in healthy controls used for calculation of fold changes were obtained from simulations where the mechanistic kidney model incorporating both P-gp and OAT-3 was used to simulate the plasma concentration-time profile of rivaroxaban after a 10 mg dose (Table 8).

investigating the effect of mild renal impairment alone, our simulated AUC and $CL_R$ fold changes of rivaroxaban fell within predefined success criteria (Fig, 4C; Table 9). Additionally, as presented in Supplemental Fig. 8C, alterations in either PTCPGK or transporter abundance (Supplemental Table 9), two independent pathophysiological mechanisms that have been proposed to account for the reduction in tubular secretion (Naud et al., 2011; Hsu et al., 2014), yielded comparable effects on the renal clearance of rivaroxaban. Hence, it is conceptually reasonable to predict transporter-mediated DDDIs in mild-to-moderate CKD by empirically applying a scaling factor to account for the linear reduction in tubular secretion in accordance with the GFR (either via PTCPGK or adjustment of transporter abundance) while accounting for inhibition against OAT3/P-gp–mediated transport. However, it is important to note that reductions in GFR and tubular secretion become disproportional in severe CKD, with the activity of OATs directly inhibited by uremic solutes at clinically relevant concentrations (Hsueh et al., 2016, 2018), Although rivaroxaban is currently contraindicated in severe CKD (creatinine clearance $<30$ ml/min), the possibility of expanding rivaroxaban use to such patients has been raised (Dias et al., 2016). Therefore, improved understanding of underlying mechanisms behind changes in tubular secretion in severe CKD is crucial.

In conclusion, the iteratively verified PBPK model of rivaroxaban is applicable to the investigation of enzyme and transporter-mediated DDDIs involving clinically relevant inhibitors and mild-to-moderate CKD, except in severe CKD where additional understanding of the effects of the pathophysiology on transporter-mediated processes is required.

### Acknowledgments

The authors thank Dr. Kathleen Giacomini (University of California, San Francisco, CA) for the kind donation of the human OAT1- and human OAT3-transfected human embryonic kidney cell lines.

### Authorship Contributions

*Participated in research design:* Cheong, Teo, Chua, Chan.

*Conducted experiments:* Cheong, Teo, Chua.

*Performed data analysis:* Cheong, Teo, Chua, Chan.

*Wrote or contributed to the writing of the manuscript:* Cheong, Teo, Chua, Chan.

### References

Abduljalil K, Cain T, Humphries H, and Rostami-Hodjegan A (2014) Deciding on success criteria for predictability of pharmacokinetic parameters from in vitro studies: an analysis based on in vivo observations. *Drug Metab Dispos* **42**:1478–1484.

Acharya P, O'Connor MP, Polli JW, Ayrton A, Ellens H, and Bentz J (2008) Kinetic identification of membrane transporters that assist P-glycoprotein-mediated transport of digoxin and loperamide through a confluent monolayer of MDCKII-hMDR1 cells. *Drug Metab Dispos* **36**: 452–460.

Ahn S-Y, Eraly SA, Tsigelny I, and Nigam SK (2009) Interaction of organic cations with organic anion transporters. *J Biol Chem* **284**:31422–31430.

Bricker NS (1969) On the meaning of the intact nephron hypothesis. *Am J Med* **46**:1–11.

Burt HJ, Neuhoff S, Almond L, Gaohua L, Harwood MD, Jamei M, Rostami-Hodjegan A, Tucker GT, and Rowland-Yeo K (2016) Metformin and cimetidine: Physiologically based pharmacokinetic modelling to investigate transporter mediated drug-drug interactions. *Eur J Pharm Sci* **88**: 70–82, doi: 10.1016/j.ejps.2016.03.020 27019345.

Chugh SS, Havmoeller R, Narayanan K, Singh D, Rienstra M, Benjamin EJ, Gillum RF, Kim YH, McAnulty JH Jr, Zheng ZJ, et al. (2014) Worldwide epidemiology of atrial fibrillation: a Global Burden of Disease 2010 Study. *Circulation* **129**:837–847.

Darwich AS, Ogungbenro K, Vinks AA, Powell JR, Reny JL, Marsousi N, Daali Y, Fairman D, Cook J, Lesko LJ, et al. (2017) Why has model-informed precision dosing not yet become common clinical reality? Lessons from the past and a roadmap for the future. *Clin Pharmacol Ther* **101**:646–656.

Dias C, Moore KT, Murphy J, Ariyawansa J, Smith W, Mills RM, and Weir MR (2016) Pharmacokinetics, pharmacodynamics, and safety of single-dose rivaroxaban in chronic hemodialysis. *Am J Nephrol* **43**:229–236.

Emami Riedmaier A, Burt H, Abduljalil K, and Neuhoff S (2016) More power to OATP1B1: an evaluation of sample size in pharmacogenetic studies using a rosuvastatin PBPK model for intestinal, hepatic, and renal transporter-mediated clearances. *J Clin Pharmacol* **56** (Suppl 7): S132–S142.

Friedrich CM (2016) A model qualification method for mechanistic physiological QSP models to support model-informed drug development. *CPT Pharmacometrics Syst Pharmacol* **5**: 43–53.

Frishman WH and Lazar EJ (1992) Sustained-release verapamil formulations for treating hypertension. *J Clin Pharmacol* **32**:455–462.

Glomme A, März J, and Dressman JB (2007) Predicting the intestinal solubility of poorly soluble drugs, in *Pharmacokinetic Profiling in Drug Research* (Bernard Testa DSDK, Wunderli-Allenspach H, and Folkers G eds) pp 259–280, Wiley, Zürich, Switzerland.

Gnoth MJ, Buetehorn U, Muenster U, Schwarz T, and Sandmann S (2011) In vitro and in vivo P-glycoprotein transport characteristics of rivaroxaban. *J Pharmacol Exp Ther* **338**:372–380.

Greenblatt DJ, Patel M, Harmatz JS, Nicholson WT, Rubino CM, and Chow CR (2018) Impaired rivaroxaban clearance in mild renal insufficiency with verapamil coadministration: potential implications for bleeding risk and dose selection. *J Clin Pharmacol* **58**:533–540.

Grillo JA, Zhao P, Bullock J, Booth BP, Lu M, Robie-Suh K, Berglund EG, Pang KS, Rahman A, Zhang L, et al. (2012) Utility of a physiologically-based pharmacokinetic (PBPK) modeling approach to quantitatively predict a complex drug-drug-disease interaction scenario for rivaroxaban during the drug review process: implications for clinical practice. *Biopharm Drug Dispos* **33**:99–110.

Guest EJ, Aarons L, Houston JB, Rostami-Hodjegan A, and Galetin A (2011) Critique of the two-fold measure of prediction success for ratios: application for the assessment of drug-drug interactions. *Drug Metab Dispos* **39**:170–173.

Haeri A, Javadian B, Saadati R, and Dadashzadeh S (2014) Metabolite parameters as an appropriate alternative approach for assessment of bioequivalence of two verapamil formulations. *Iran J Pharm Res* **13**:383–389.

Hsu V, de L T Vieira M, Zhao P, Zhang L, Zheng JH, Nordmark A, Berglund EG, Giacomini KM, and Huang SM (2014) Towards quantitation of the effects of renal impairment and probenecid inhibition on kidney uptake and efflux transporters, using physiologically based pharmacokinetic modelling and simulations. *Clin Pharmacokinet* **53**:283–293.

Hsueh CH, Hsu V, Zhao P, Zhang L, Giacomini KM, and Huang SM (2018) PBPK modeling of the effect of reduced kidney function on the pharmacokinetics of drugs excreted renally by organic anion transporters. *Clin Pharmacol Ther* **103**:485–492.

Hsueh C-H, Yoshida K, Zhao P, Meyer TW, Zhang L, Huang S-M, and Giacomini KM (2016) Identification and quantitative assessment of uremic solutes as inhibitors of renal organic anion transporters, OAT1 and OAT3. *Mol Pharm* **13**:3130–3140.

Huang W and Isoherranen N (2018) Development of a dynamic physiologically based mechanistic kidney model to predict renal clearance. *CPT Pharmacometrics Syst Pharmacol* **7**:593–602.

Ismail M, Lee VH, Chow CR, and Rubino CM (2018) Minimal physiologically based pharmacokinetic and drug-drug-disease interaction model of rivaroxaban and verapamil in healthy and renally impaired subjects. *J Clin Pharmacol* **58**:541–548.

Jamei M (2016) Recent advances in development and application of physiologically-based pharmacokinetic (PBPK) models: a transition from academic curiosity to regulatory acceptance. *Curr Pharmacol Rep* **2**:161–169.

Jamei M, Dickinson GL, and Rostami-Hodjegan A (2009) A framework for assessing inter-individual variability in pharmacokinetics using virtual human populations and integrating general knowledge of physical chemistry, biology, anatomy, physiology and genetics: a tale of 'bottom-up' vs 'top-down' recognition of covariates. *Drug Metab Pharmacokinet* **24**:53–75.

January CT, Wann LS, Alpert JS, Calkins H, Cigarroa JE, Cleveland JC Jr, Conti JB, Ellinor PT, Ezekowitz MD, Field ME, et al. American College of Cardiology/American Heart Association Task Force on Practice Guidelines (2014) 2014 AHA/ACC/HRS guideline for the management of patients with atrial fibrillation: a report of the American College of Cardiology/American Heart Association Task Force on Practice Guidelines and the Heart Rhythm Society [published correction appears in *J Am Coll Cardiol* (2014) 64:2305–2307]. *J Am Coll Cardiol* **64**:e1–e76.

Kubitza D, Becka M, Voith B, Zuehlsdorf M, and Wensing G (2005a) Safety, pharmacodynamics, and pharmacokinetics of single doses of BAY 59-7939, an oral, direct factor Xa inhibitor. *Clin Pharmacol Ther* **78**:412–421.

Kubitza D, Becka M, Wensing G, Voith B, and Zuehlsdorf M (2005b) Safety, pharmacodynamics, and pharmacokinetics of BAY 59-7939—an oral, direct Factor Xa inhibitor—after multiple dosing in healthy male subjects. *Eur J Clin Pharmacol* **61**:873–880.

Lee CA, Jones JP 3rd, Katayama J, Kaspera R, Jiang Y, Freiwald S, Smith E, Walker GS, and Totah RA (2012) Identifying a selective substrate and inhibitor pair for the evaluation of CYP2J2 activity. *Drug Metab Dispos* **40** (5):943–951, doi: 10.1124/dmd.111.043505 22328583.

Lumen AA, Li L, Li J, Ahmed Z, Meng Z, Owen A, Ellens H, Hidalgo IJ, and Bentz J (2013) Transport inhibition of digoxin using several common P-gp expressing cell lines is not necessarily reporting only on inhibitor binding to P-gp. *PLoS One* **8**:e69394.

Ménochet K, Kenworthy KE, Houston JB, and Galetin A (2012) Simultaneous assessment of uptake and metabolism in rat hepatocytes: a comprehensive mechanistic model. *J Pharmacol Exp Ther* **341**:2–15.

Moore KT, Vaidyanathan S, Natarajan J, Ariyawansa J, Haskell L, and Turner KC (2014) An open-label study to estimate the effect of steady-state erythromycin on the pharmacokinetics, pharmacodynamics, and safety of a single dose of rivaroxaban in subjects with renal impairment and normal renal function. *J Clin Pharmacol* **54**:1407–1420.

Mueck W, Kubitza D, and Becka M (2013) Co-administration of rivaroxaban with drugs that share its elimination pathways: pharmacokinetic effects in healthy subjects. *Br J Clin Pharmacol* **76**: 455–466.

Mueck W, Stampfuss J, Kubitza D, and Becka M (2014) Clinical pharmacokinetic and pharmacodynamic profile of rivaroxaban. *Clin Pharmacokinet* **53**:1–16.

Naud J, Michaud J, Beauchemin S, Hébert MJ, Roger M, Lefrancois S, Leblond FA, and Pichette V (2011) Effects of chronic renal failure on kidney drug transporters and cytochrome P450 in rats. *Drug Metab Dispos* **39**:1363–1369.

Neely M (2017) Scalpels not hammers: the way forward for precision drug prescription. *Clin Pharmacol Ther* **101**:368–372.

Orr STM, Ripp SL, Ballard TE, Henderson JL, Scott DO, Obach RS, Sun H, and Kalgutkar AS (2012) Mechanism-based inactivation (MBI) of cytochrome P450 enzymes: structure-activity relationships and discovery strategies to mitigate drug-drug interaction risks. *J Med Chem* **55**: 4896–4933.

Prasad B, Johnson K, Billington S, Lee C, Chung GW, Brown CDA, Kelly EJ, Himmelfarb J, and Unadkat JD (2016) Abundance of drug transporters in the human kidney cortex as quantified by quantitative targeted proteomics. *Drug Metab Dispos* **44**:1920–1924.

Ren S, Zeng J, Mei Y, Zhang JZH, Yan SF, Fei J, and Chen L (2013) Discovery and characterization of novel, potent, and selective cytochrome P450 2J2 inhibitors. *Drug Metab Dispos* **41** (1):60–71, doi: 10.1124/dmd.112.048264 23033255.

Rodgers T and Rowland M (2006) Physiologically based pharmacokinetic modelling 2: predicting the tissue distribution of acids, very weak bases, neutrals and zwitterions. *J Pharm Sci* **95**: 1238–1257.

Rostami-Hodjegan A (2018) Reverse translation in PBPK and QSP: going backwards in order to go forward with confidence. *Clin Pharmacol Ther* **103**:224–232.

Sager JE, Yu J, Ragueneau-Majlessi I, and Isoherranen N (2015) Physiologically based pharmacokinetic (PBPK) modeling and simulation approaches: a systematic review of published models, applications, and model verification. *Drug Metab Dispos* **43**:1823–1837.

Scaglione F (2013) New oral anticoagulants: comparative pharmacology with vitamin K antagonists. *Clin Pharmacokinet* **52**:69–82.

Scotcher D, Jones CR, Galetin A, and Rostami-Hodjegan A (2017) Delineating the role of various factors in renal disposition of digoxin through application of physiologically based kidney model to renal impairment populations. *J Pharmacol Exp Ther* **360**:484–495.

Shebley M, Fu W, Badri P, Bow D, and Fischer V (2017) Physiologically based pharmacokinetic modeling suggests limited drug-drug interaction between clopidogrel and dasabuvir. *Clin Pharmacol Ther* **102**:679–687.

Shebley M, Sandhu P, Emami Riedmaier A, Jamei M, Narayanan R, Patel A, Peters SA, Reddy VP, Zheng M, de Zwart L, et al. (2018) Physiologically based pharmacokinetic model qualification and reporting procedures for regulatory submissions: a consortium perspective. *Clin Pharmacol Ther* **104**:88–110.

Stampfuss J, Kubitza D, Becka M, and Mueck W (2013) The effect of food on the absorption and pharmacokinetics of rivaroxaban. *Int J Clin Pharmacol Ther* **51**:549–561.

Takács-Novák K, Szőke V, Völgyi G, Horváth P, Ambrus R, and Szabó-Révész P (2013) Biorelevant solubility of poorly soluble drugs: rivaroxaban, furosemide, papaverine and niflumic acid. *J Pharm Biomed Anal* **83**:279–285.

Tsuruya Y, Nakanishi T, Komori H, Wang X, Ishiguro N, Kito T, Ikukawa K, Kishimoto W, Ito S, Schaefer O, et al. (2017) Different involvement of OAT in renal disposition of oral anticoagulants rivaroxaban, dabigatran, and apixaban. *J Pharm Sci* **106**:2524–2534.

US Food and Drug Aministration (2011a) XARELTO (rivaroxaban), Clinical Pharmacology and Biopharmaceutics Review, U.S. Food and Drug Administration, Silver Spring, MD.

US Food and Drug Aministration (2011b) XARELTO (rivaroxaban) product information, U.S. Food and Drug Administration, Silver Spring, MD.

US Food and Drug Aministration (2017) Drug development and drug interactions: table of substrates, inhibitors and inducers, Center for Drug Evaluation and Research, Silver Spring, MD.

Vermeer LMM, Isringhausen CD, Ogilvie BW, and Buckley DB (2016) Evaluation of ketoconazole and its alternative clinical CYP3A4/5 inhibitors as inhibitors of drug transporters: the in vitro effects of ketoconazole, ritonavir, clarithromycin, and itraconazole on 13 clinically-relevant drug transporters. *Drug Metab Dispos* **44**:453–459.

Wang J and Flanagan DR (1999) General solution for diffusion-controlled dissolution of spherical particles. 1. Theory. *J Pharm Sci* **88**:731–738.

Wessler JD, Grip LT, Mendell J, and Giugliano RP (2013) The P-glycoprotein transport system and cardiovascular drugs [published correction appears in *J Am Coll Cardiol* (2014) 63:2176]. *J Am Coll Cardiol* **61**:2495–2502.

Wise DL (2000) *Handbook of Pharmaceutical Controlled Release Technology*, CRC Press, Boca Raton, FL.

Xu R, Ge W, and Jiang Q (2018) Application of physiologically based pharmacokinetic modeling to the prediction of drug-drug and drug-disease interactions for rivaroxaban. *Eur J Clin Pharmacol* **74**:755–765.

Zhao X, Sun P, Zhou Y, Liu Y, Zhang H, Mueck W, Kubitza D, Bauer RJ, Zhang H, and Cui Y (2009) Safety, pharmacokinetics and pharmacodynamics of single/multiple doses of the oral, direct Factor Xa inhibitor rivaroxaban in healthy Chinese subjects. *Br J Clin Pharmacol* **68**:77–88.

**Address correspondence to:** Eric Chun Yong Chan, Department of Pharmacy, Faculty of Science, National University of Singapore, 18 Science Drive 4, Singapore 117543, Singapore. E-mail: phaccye@nus.edu.sg

**Supplemental Data:**

# Systematic Development and Verification of A Physiologically-Based Pharmacokinetic Model of Rivaroxaban

Eleanor Jing Yi Cheong[1], Denise Wun Xi Teo[1], Denise Xin Yi Chua[1] and Eric Chun Yong Chan[1,2]

[1]Department of Pharmacy, Faculty of Science, National University of Singapore, 18 Science Drive 4, Singapore 117543; [2]Singapore Institute for Clinical Sciences (SICS), Brenner Centre for Molecular Medicine, 30 Medical Drive, Singapore 117609

***Drug Metabolism and Disposition***

## Supplemental Methods

### 1 Model Development

### 1.1 PBPK Model of Rivaroxaban

**Supplemental Table 1**. Clearance parameters of rivaroxaban utilized for retrograde analysis within the Simcyp simulator

| Trial | No. of subjects | Dose (mg) | $AUC_{0h-\infty}$ (ng.h/mL) | Apparent Oral Clearance (L/h) |
|---|---|---|---|---|
| **(Kubitza, Becka, *et al.*, 2013)** | 6 | 10 | | 8.26 |
| | 6 | 10 | | 6.77 |
| **(Kubitza, Becka, Mueck, Halabi, Maatouk, Klause, Lufft, Dominic D. Wand, *et al.*, 2010)** | 8 | 10 | | 8 |

| | | | | |
|---|---|---|---|---|
| **(Kubitza, Roth, *et al.*, 2013)** | 16 | 10 | | 6.6 |
| **(Kreutz *et al.*, 2017)** | 24 | 20 | | 10.9 |
| **(Dias *et al.*, 2016)** | 8 | 15 | | 8.31 |
| **(Moore *et al.*, 2014)** | 45 | 20 | 2277 | 8.78 |
| **(Stampfuss *et al.*, 2013)** | 24 | 10 | 1201 | 8.33 |
| | 24 | 15 | 1801 | 8.33 |
| | 24 | 20 | 2294 | 8.72 |
| | | | Weighted Mean Clearance: | 8.61 L/h |
| | | | Weighted Mean Renal Clearance: | 36% × 8.61 L/h = 3.1 L/h |

**Mechanistic Kidney Model Development via *In Vitro In Vivo* Extrapolation**

**Materials for *In Vitro* Uptake and Efflux Assays**. Madin-Darby canine kidney sub-clone I cells transfected with multi drug resistance gene (MDCK-MDR1) were donated by A/P Gigi Chiu. Human embryonic kidney 293 (HEK293) cells transfected with OAT1 and OAT3 were obtained from Dr. Kathleen Giacomini (University of California, San Francisco, San Francisco, CA). Dulbecco's modified eagle's medium (DMEM) with L-Glutamine (DMEM Glutamax) and DMEM (high glucose), 4-(2-hydroxyethyl)-1-piperazineethanesulfonic acid (HEPES), heat inactivated foetal bovine serum (FBS), penicillin/streptomycin 10,000 IU antibiotic solution (pen/strep), 10× trypsin-EDTA, hygromycin B, lucifer yellow CH dilithium salt and Hank's balanced salt solution (HBSS) were from Gibco® Life Technologies (Waltham, MA, USA). 1 M stock solution of phosphate buffer saline (PBS) was purchased from Vivantis (Subang Jaya, Malaysia). Lucifer yellow was dissolved in milli-Q water obtained using a milli-Q water purification system (Millipore, Billerica, MA). Rivaroxaban was purchased from Carbosynth (Compton, Oxford, England) and was reconstituted in dimethyl sulfoxide (DMSO). 4-aminohippuric acid was from Cayman Chemical (Ann Arbor, Michigan, USA) Propranolol, quinidine, estrone-3-sulfate and probenecid were from Sigma Aldrich (St. Louis, MO, USA) and were reconstituted in either DMSO or methanol. Subsequent dilutions for all compounds were carried out using DMSO. All other reagents were of analytical grade.

**MDCK-MDR1 Cell Culture**. MDCK-MDR1 cells were cultured at 37°C and were maintained in DMEM Glutamax culture media supplemented with 10% FBS and 1% pen/strep in humidified air-5% $CO_2$. Cells were passaged upon reaching approximately 100% confluence using 5× trypsin–EDTA and seeded in T75 flasks. For transport studies, MDCK-MDR1 cells (passage number 20 to 29) were seeded at a density of 200,000 cells on 24 well ThinCert™ cell culture inserts (8.4 mm id, 0.1 µm pore size). After allowing the cells to settle for at least 24 h, the culture media was refreshed. Transport assays were conducted approximately 48 h after seeding (Shirasaka *et al.*, 2008).

**Setup of the Bidirectional Transport Assay.** Culture media was first removed and each well and insert were washed with PBS before initiation of transport assays to minimize residual metabolic waste. As shown in the setup below, for absorptive transport, solutions (300 µL) containing test drugs and lucifer yellow in DMEM were added to the donor apical compartment (A), with culture media (600 µL) in the receiver basolateral compartment (B). In parallel wells measuring secretory transport, test solutions were added to the donor basolateral compartment (B) with culture media in the receiver apical compartment (A).

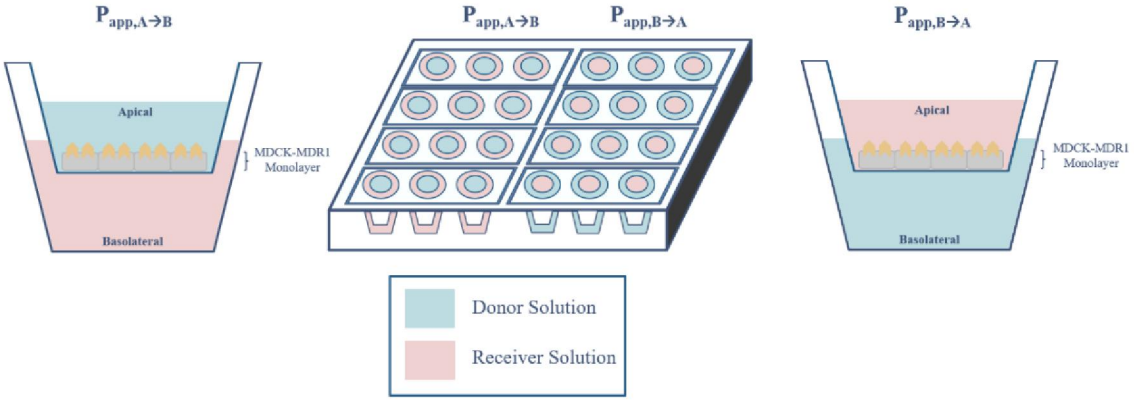


Bidirectional transport assay experimental setup.

**Validation of Transport Assay Functionality.** To ascertain the functionality of the proposed *in vitro* system in quantifying the P-gp-mediated transport of rivaroxaban, rigorous assay validation was also performed (Volpe, 2016; FDA/CDER, 2017). Monolayer integrity was established via the calculation

of the paracellular flux of low permeability compound lucifer yellow as described in **eq. S1** (Polli *et al.*, 2008).

$$P_{app,AB} \text{ of lucifer yellow (nm/s)} = -\left(\frac{V_D V_R}{(V_D + V_R)At}\right) ln\left[1 - \frac{(V_D + V_R)C_R(t)}{V_D C_D(t) + V_R C_R(t)}\right] \times 10^7 \quad \textbf{(S1)}$$

where $V_D$ is the volume of donor solution (mL), $V_R$ is the volume of receiver solution (mL), A is the surface area of monolayer ($cm^2$), $t$ is the incubation time (s), $C_D(t)$ is the measured concentration in the donor well at time $t$ (nM), $C_R(t)$ is the measured concentration in the receiver well at time $t$ (nM). Acceptance criteria was defined as a passive permeability ($P_{app}$) of < 5 x $10^6$ cm/s (Ellens *et al.*, 2017). Efflux ratios of positive control (quinidine 10 μM) and negative control propranolol (10 μM) were assessed and compared with literature reported values. As accuracy of the transport ratios could be compromised by poor recovery which can be calculated by **eq. S2**, a mass balance cut-off exceeding 70% was deemed acceptable according to previously published guidelines by the International Transporter Consortium (Brouwer *et al.*, 2013).

$$\text{Percentage recovery (\%)} = \frac{D_t + R_t}{D_0} \times 100\% \quad \textbf{(2)}$$

where $D_t$ and $R_t$ represent the amount of substrate in the donor and receiver chambers at the end of experiment respectively, and $D_0$ is the amount of substrate in the donor chamber at $t$ = 0 min.

**Investigation of the *In Vitro* P-gp-mediated Transport of Rivaroxaban.** To ensure that transport studies were conducted under conditions where flux was linearly related to time, time-dependent changes in rivaroxaban transport (10 μM in donor) in both absorptive and secretory directions were monitored by quantifying receiver compartment concentrations at 30, 60, 120, 180, 240, 300 and 360 min. Subsequent concentration-dependent permeation experiments were conducted with 5 different concentrations of rivaroxaban (3, 10, 30, 75, 100 μM) using the optimized incubation time of 90 min. Absorptive ($J_{AB}$) or secretory ($J_{BA}$) flux was calculated using **eq. S3**:

$$J_{AB} \text{ or } J_{BA} = \frac{dQ}{dt} \quad \textbf{(S3)}$$

where Q is the amount of compound transported over time t of the experiment. Apparent passive permeability ($P_{app}$) was derived from flux using **eq. S4**:

$$P_{app} = \frac{J}{S \times C_D} \quad \textbf{(S4)}$$

where $C_D$ is the initial concentration of the test compound added to the donor compartment and S is the surface area of the porous membrane in $cm^2$. The efflux ratio (ER) was calculated using **eq. S5** (Troutman and Thakker, 2003):

$$Efflux\ Ratio = \frac{P_{app,BA}}{P_{app,AB}} \quad \textbf{(S5)}$$

Rivaroxaban flux ($J_{pass}$) and apparent permeability solely due to passive diffusion ($P_{pass}$) were approximated in the presence of 100 μM of verapamil (~20× greater than the reported half maximal inhibitory concentration ($IC_{50}$) in L-MDR1 cells = 4.3 ± 1.9 μM) (Gnoth *et al.*, 2011), ensuring abolishment of P-gp efflux activity.

**Analyzing P-gp Mediated Efflux of Rivaroxaban Using the Conventional Michaelis-Menten Approach.** Overall flux during absorptive ($J_{AB}$) and secretory transport ($J_{BA}$) can be quantified using **eqs. S6** and **S7**, where $J_{pass}$ and $J_{P-gp,X}$ represent passive and P-gp-mediated flux respectively (Troutman and Thakker, 2003). X denotes transport direction, either A to B or B to A.

$$J_{AB} = J_{pass} - J_{P-gp,AB} \quad \textbf{(S6)}$$

$$J_{BA} = J_{P-gp,BA} + J_{pass} \quad \textbf{(S7)}$$

Relationships specified in e**qs. S4**, **S6** and **S7** can be further modified to obtain permeability equations describing the concentration dependence of clearance ($P_{app}$×S) derived from both absorptive and secretory directions. **Eqs. S8** and **S9** comprise a saturable component that describes P-gp-mediated efflux where $J_{max,app}$ and $K_{m,app}$ represent the maximal achievable transport rate and the donor chamber concentration associated with half-maximal transport rate respectively. Additionally, passive permeability was quantified via the term denoting first order passive diffusion clearance ($P_{pass}$×S).

$$P_{app,AB} \times S = P_{pass} \times S - \frac{1000 \times J_{max,app}}{K_{m,app} + C_D} \quad \textbf{(S8)}$$

$$P_{app,BA} \times S = \frac{1000 \times J_{max,app}}{K_{m,app} + C_D} + P_{pass} \times S \quad \textbf{(S9)}$$

$P_{app}$ obtained from concentration-dependent transport experiments along with $P_{pass}$ obtained in the presence of P-gp inhibitor verapamil were fitted to **Eqs. S8** and **S9** using GraphPad PRISM® software version 7.01 (San Diego, CA, USA) to calculate initial estimates of $J_{max,app}$ and $K_{m,app}$.

**Analyzing P-gp Mediated Efflux of Rivaroxaban Using A Three Compartmental Model.** Measured time- and concentration-dependent data for the absorptive and secretory transport of rivaroxaban were fitted separately to a three-compartment model using the Simcyp *In Vitro* Analysis (SIVA) Toolkit Version 3, where a system of differential equations (**Eqs. S10, S11 and S12**) was applied to dynamically model changes in drug concentration ($\frac{dS}{dt}$) in the apical, intracellular and basolateral compartments respectively (**refer to table and diagram for additional details on system-dependent parameters required**). Given that only unbound concentrations are involved in bidirectional passive diffusion across the apical and basolateral membranes, and apical efflux is also driven by the intracellular unbound concentrations, ultrafiltration was performed to determine the fraction unbound of rivaroxaban in media ($fu_{media}$) as well as within the cell ($fu_{cell}$) (**More details on the ultrafiltration protocol are highlighted in the subsequent section**). Naïve pooled fitting was performed to estimate $J_{max}$, $K_m$ and passive diffusion clearance ($CL_{PD}$) based on the initial values of $J_{max,app}$, $K_{m,app}$ and $P_{pass,app}$ obtained from the Michaelis-Menten model. Given the potential uncertainty associated with initial estimates, both hybrid (global followed by Nelder-Mead) and local Nelder-Mead optimization were used to minimize the objective function value (OFV), defined by the overall sum of square residuals between the experimental and simulated data which are weighted by the reciprocal of predicted squared. Model performance was assessed via goodness of fit between observed and predicted values, the coefficient of determination ($R^2$), Akaike information criterion (AIC) and difference in small sample size corrected version of AIC (ΔAICc). Confidence intervals around final estimated parameters were employed as diagnostics of parameter certainty.

$$V_{ap}.\frac{dS_{ap}}{dt} = \frac{J_{max}.SA.[S]_{cell,u}}{K_{m,u} + [S]_{cell,u}} + P_{pass} \times SA \times 60/1000([S]_{cell,u} - [S]_{ap,u}] \quad \textbf{(S10)}$$

$$V_{cell}.\frac{dS_{cell}}{dt} = -\frac{J_{max}.SA.[S]_{cell,u}}{K_{m,u} + [S]_{cell,u}} + P_{pass} \times SA \times 60/1000([S]_{ap,u}] + [S]_{bl,u} - 2[S]_{cell,u}] \quad \textbf{(S11)}$$

$$V_{bl}.\frac{dS_{bl}}{dt} = P_{pass} \times SA \times 60/1000([S]_{cell,u} - [S]_{bl,u}] \quad \textbf{(S12)}$$

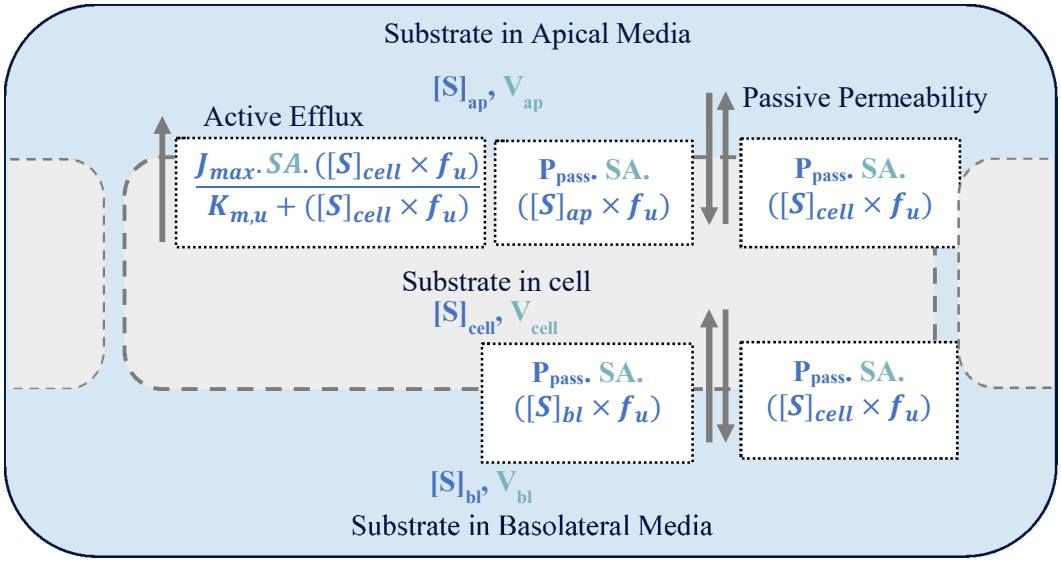


Three-compartment permeability and transport model in the Simcyp *in vitro* analysis (SIVA) toolkit. Drug-dependent parameters include $J_{max}$: *In vitro* maximal rate of transporter mediated efflux; $K_m$: Michaelis Menten constant; $P_{pass}$: Passive permeability, $f_u$: fraction unbound. System dependent parameters include the surface area occupied (SA) and volumes of the intracellular ($V_{cell}$), apical ($V_{ap}$) and basolateral ($V_{bl}$) compartments respectively.

**System-dependent parameters utilized for three-compartmental analysis**

| Parameter | Value | Method/Reference |
|---|---|---|
| Surface area ($cm^2$) | 0.33 | Greiner Bio-one Thincert™ Tissue Culture Inserts for 24-well plates |
| Volume of the apical compartment ($V_{ap}$) (µL) | 300 | Defined experimentally |
| Volume of the basolateral compartment ($V_{bl}$) (µL) | 600 | Defined experimentally |
| Volume of the intracellular compartment ($V_{cell}$) (µL) | 0.47 | (von Bonsdorff *et al.*, 1985) |

**HEK293 Cell Culture.** HEK wild type cells were cultured at 37°C and were maintained in DMEM culture media supplemented with 10% FBS and 1% pen/strep in humidified air - 5% CO2. Similar culture conditions were utilized for HEK-OAT3 and OAT1 culture albeit with the addition of hygromycin B (50 µg/mL). For transport studies, wild type and OAT1/3-transfected cells (passage number 3-15) were directly seeded into Biocoat 24-well poly-D-lysine coated plates (Corning, NY) 48 hours before each experiment, at densities of 2.4 (wild type) and $3.6\times10^5$ (OAT3/1-transfected) cells/well in a volume of 400 µL. Transport assays were conducted approximately 48 h after seeding upon verification of monolayer confluence as described previously (Mathialagan, Piotrowski, *et al.*, 2017; Mathialagan, Rodrigues, *et al.*, 2017).

**Setup of the Uptake Assay and Verification of Assay Functionality.** Transport buffer was prepared at pH 7.4 using Hank's balanced salt solution supplemented with 20 mM HEPES. Estrone 3-sulfate (2 µM) and para aminohippuric acid (3 µM) were used as control probe substrates for OAT3 and OAT1 respectively, to monitor the functionality of the cells. Immediately before the experiment, the cells were washed twice with 200 µL of transport buffer, leaving the final rinse volume for 10 min to allow equilibration. Uptake was initiated by incubating with 200 µL transport buffer (containing 0.5 -100 µM rivaroxaban) at 37°C. At four different time points from 0.5 to 2 min, cellular uptake was terminated by washing the cells twice with 200 µL of ice-cold PBS and lysed directly on the plate with 100% methanol containing internal standard (IS).

**Analyzing OAT-3 Mediated Uptake of Rivaroxaban Using the Conventional Two-Step Approach.** Initial estimates for clearances via passive diffusion ($CL_{PD}$) and active uptake ($CL_{int,T} = J_{max}/K_m$) were derived based on the two-step approach. Uptake rates of rivaroxaban in both wild type and transfected HEK cells were calculated over 2 min (time-linear conditions) and expressed as the slope of the linear regression of the rates of transport versus time plot. Passive diffusion clearance ($CL_{PD}$) was calculated from the uptake rates measured in wild type cells (**eq. S13**) and inserted into **eq. S14**, which describes total cellular uptake measured at 37°C as a composite of both saturable active uptake and non-saturable passive transport.

$$v = CL_{PD} \times S \tag{S13}$$

$$v = \frac{J_{max} \times [S]}{K_m + [S]} + CL_{PD} \times [S] \tag{S14}$$

v represents the rate of uptake (pmol/min/mg), [S] is the substrate concentration (µM), $J_{max}$ is the maximum rate of active transport (pmol/min/mg), $K_m$ is the Michaelis constant (µM) and $CL_{PD}$ is the passive diffusion clearance (µL/min/mg).

**Determination of Uptake Kinetics Parameters using a Mechanistic Two-Compartmental Model.** To facilitate the dynamic evaluation of flux in rivaroxaban concentrations due to active transport, bidirectional passive diffusion and intracellular/extracellular binding processes occurring during uptake, naïve pooled concentration-time data of rivaroxaban in the intracellular compartment was fitted to a mechanistic two-compartmental model using the Simcyp *In Vitro* Analysis (SIVA) Toolkit Version 3 (figure above) as described by **eqs. S15** and **S16** (**refer to table and diagram for additional details on system-dependent parameters required**).

$$V_{media} + K_{mem} \times No\ of\ cells\left(\frac{d[S]_{media}}{dt}\right) = -CL_{int,u,uptake}.No\ of\ cells.S_{media}.f_{u,media} + CL_{PD}([S]_{cell} \times f_{u,cell} - [S]_{media}.f_{u,media}) \tag{S15}$$

$$(V_{cell}.No\ of\ cells)\frac{d[S]_{cell}}{dt} = CL_{int,u,uptake}.No\ of\ cells.S_{media}.f_{u,media} + CL_{PD}([S]_{media}.f_{u,media} - f_{u,cell} \times [S]_{cell}) \tag{S16}$$

Initial $CL_{PD}$ and $CL_{int,T}$ values derived from the two-step approach were converted from units of µL/min/mg protein to µL/min/$10^6$ cells on the basis that 1 million HEK293 cells contain 0.15 mg of total protein (measured). Naïve pooled fitting of measured time-and concentration-dependent uptake data was performed to estimate $CL_{int,u,uptake}$, with $CL_{PD}$ and the surface binding constant ($K_{mem}$) inserted as constants into the model (see table below). The unbound fraction of rivaroxaban in media and the cellular homogenate was also fixed at 1 and 0.023 respectively.

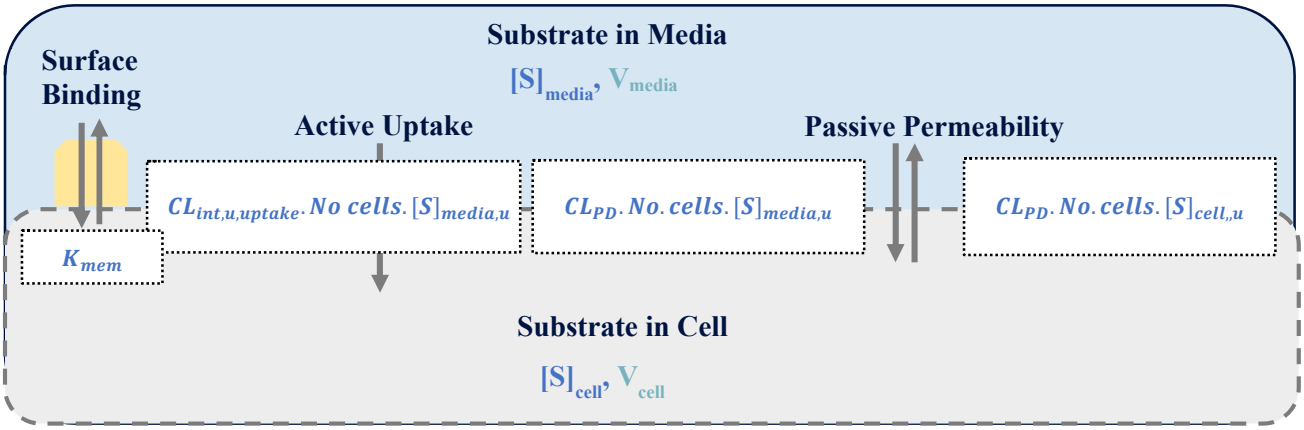


Two-compartment permeability and transport model in the Simcyp *in vitro* analysis (SIVA) toolkit. Drug-dependent parameters include $CL_{int,u,uptake}$: unbound intrinsic clearance for active uptake; $CL_{PD}$: Passive diffusion clearance, $f_{umedia/cell}$: fraction unbound in media/within the cell and $K_{mem}$; surface binding constant. System dependent parameters include the volumes of the intracellular ($V_{cell}$), and media compartments as well as the number of cells.

**System-dependent parameters utilized for two compartmental analysis**

| Parameter | Value | Method/Reference |
|---|---|---|
| ***System-Dependent*** | | |
| **$V_{media}$ (µL)** | **300** | Defined experimentally |
| **$V_{cell}$ (µL/$10^6$ cells)** | **1.7** | Measured assuming spherical structure and a cell diameter of 14.8 µm (Mathialagan, Piotrowski, *et al.*, 2017) |
| **No. of cells ($10^6$ cells)** | **0.06** | Calculated based on average measured protein concentration per well and the number of cells per measured protein (0.15 mg/$10^6$ cells) |
| ***Drug-Dependent*** | | |
| **$K_{mem}$ (µL/$10^6$ cells)** | **0.001** | Default value in SIVA |
| **$fu_{media}$** | **1** | Assumed to be 1 despite known non-specific binding to test apparatus for many compounds |
| **$fu_{cell}$** | **0.023** | Assumed to be the same as that measured using ultrafiltration in the MDCK-MDR1 homogenate |
| **$CL_{PD}$ (µL/min/$10^6$ cells)** | **22.64** | Calculated from linear regression of uptake rates across rivaroxaban concentrations measured in wild type HEK cells to be 159.4 µL/min/mg protein (**Supplemental Fig. 2F**)<br>Corrected to units of µL/min/$10^6$ cells based on 0.15 mg protein/$10^6$ HEK cells |

## 1.2 PBPK Models of Verapamil, Norverapamil and Ketoconazole

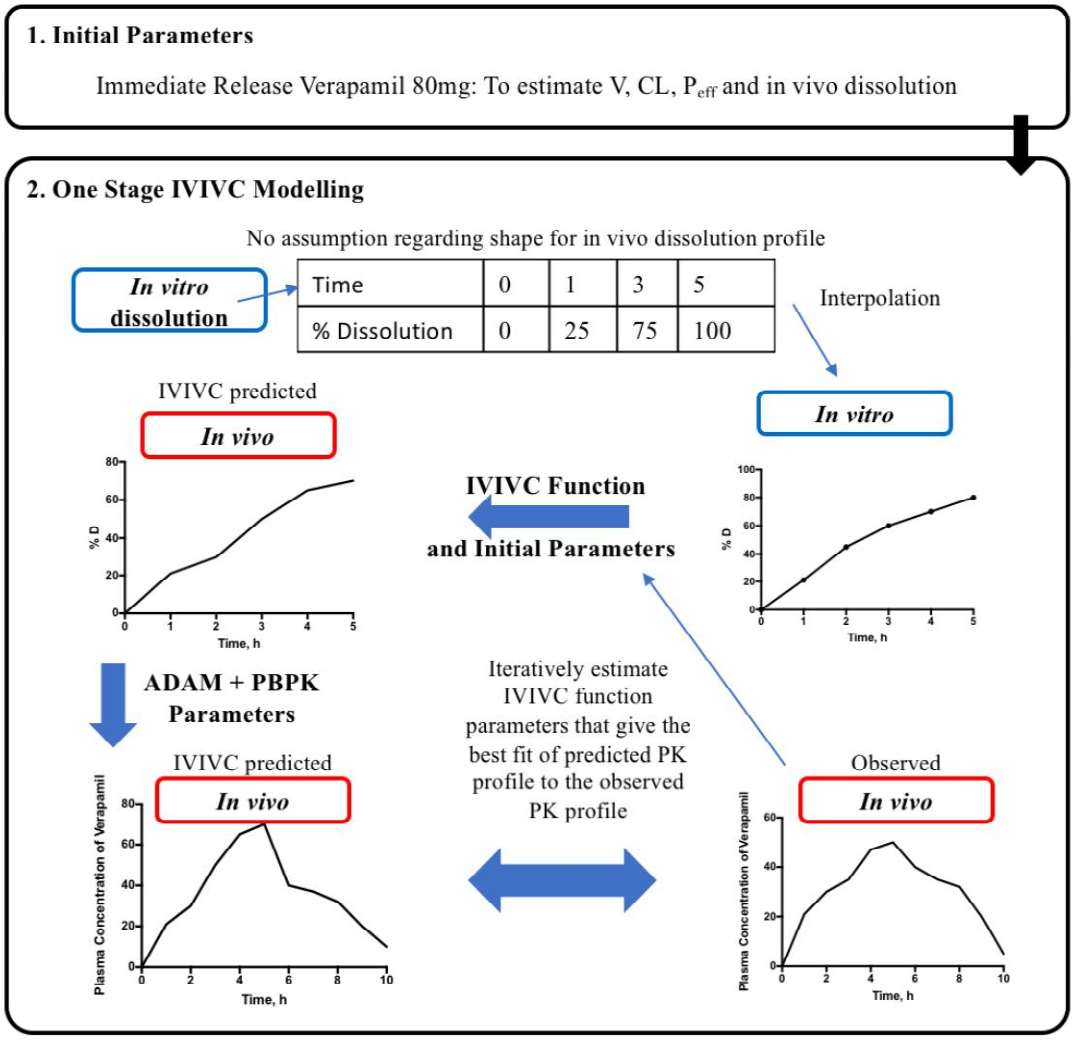


**Supplemental Fig. 1** *In vitro in vivo* correlation workflow to recapitulate the PK of a controlled release formulation of verapamil.

**Supplemental Table 2.1.** Key input parameters for the PBPK model of verapamil

| **Parameter** | **Value** | **Method/Reference** |
|---|---|---|
| Molecular weight (g/mol) | 454.6 | Simcyp compound file |
| log P | 4.46 | Simcyp compound file |
| Compound type | Monoprotic Base | Simcyp compound file |
| pKa | 8.78 | Simcyp compound file |
| B/P | 0.709 | Simcyp compound file |
| fu | 0.09 | Simcyp compound file |
| Main plasma binding protein | Human serum albumin | Simcyp compound file |
| | | |
| **Absorption Model** | **ADAM Model** | |
| $fu_{gut}$ | 1 | Predicted |
| $P_{eff,man}$ ($10^{-4}$cm/s) | 6.08477 | Predicted, Simcyp compound file |
| Permeability Assay | Caco-2 | |
| Apical pH : Basolateral pH | 7.4 : 7.4 | |
| Activity | Passive & Active | |
| $P_{appaA:B}$($10^{-6}$ cm/s) | 50 | |
| Reference Compound | Propranolol | |
| Reference Compound $P_{appaA:B}$ ($10^{-6}$ cm/s) | 109 | |
| Scalar | 0.3944954 | |
| Solubility pH Type | Intrinsic | Predicted |
| Solubility (mg/mL) | 0.022 | (Popović-Nikolić *et al.*, 2017) |
| | | |
| Transporter | ABCB1 (P-gp/MDR1) | Simcyp compound file |
| $J_{max}$ (pmol/min/cm$^2$) | 2.814 | |
| $K_m$ (μM) | 0.734 | |
| fuinc | 1 | |
| Insert growth area of the Transwell (cm²) | 1 | |
| System | User | |
| RAF/REF | 0.608 | |

| | | |
|---|---|---|
| Transporter | ABCC2 (MRP2) | Simcyp compound file |
| $CL_{int,T}$ (µL/min/cm$^2$) | 18 | |
| fuinc | 1 | |
| Insert growth area of the Transwell (cm$^2$) | 1 | |
| System | User | |

| **Distribution Model** | **Full PBPK Model** | |
|---|---|---|
| $V_{SS}$ (L/kg) | 5.366168 | Predicted - Method 2 |

| | | |
|---|---|---|
| Enzyme | CYP2C8 | Simcyp compound file |
| Pathway | Norverapamil | |
| $V_{max}$ (pmol/min/pmol) | 221.2 | |
| $K_m$ (µM) | 140.5 | |

| | | |
|---|---|---|
| Enzyme | CYP3A4 | Simcyp compound file |
| Pathway | Norverapamil | |
| $V_{max}$ (pmol/min/pmol) | 154.3 | |
| $K_m$ (µM) | 122 | |

| | | |
|---|---|---|
| Enzyme | CYP3A5 | Simcyp compound file |
| Pathway | Norverapamil | |
| $V_{max}$ (pmol/min/pmol) | 169.3 | |
| $K_m$ (µM) | 87.5 | |

| | | |
|---|---|---|
| Enzyme | CYP2C8 | Simcyp compound file |
| Pathway | D-617 | |
| $V_{max}$ (pmol/min/pmol) | 218.9 | |
| $K_m$ (µM) | 156 | |

| | | |
|---|---|---|
| Enzyme | CYP3A4 | Simcyp compound file |
| Pathway | D-617 | |
| $V_{max}$ (pmol/min/pmol) | 174 | |
| $K_m$ (µM) | 99.5 | |

| | | |
|---|---|---|
| Enzyme | CYP3A5 | Simcyp compound file |
| Pathway | D-617 | |
| $V_{max}$ (pmol/min/pmol) | 117.7 | |
| $K_m$ (µM) | 73 | |
| | | |
| $CL_{int}$ (HLM) (µL/min/mg protein) | 79.57 | Simcyp compound file |
| | | |
| $CL_R$ (L/h) | 2.52 | Simcyp compound file |
| | | |
| | | |
| Enzyme | CYP3A4 | Internal Data |
| $K_i$ (µM) | 0.487 | |
| $fu_{mic}$ | 0.67 | |
| $K_I$ (µM) | 1.653 | |
| $k_{inact}$ (1/h) | 3.924 | |
| $fu_{mic}$ | 0.67 | |
| | | |
| Enzyme | CYP2J2 | Internal Data |
| $K_i$ (µM) | 12.2 | |

**Supplemental Table 2.2.** Key input parameters for the PBPK model of norverapamil

| **Parameter** | **Value** | **Method/Reference** |
|---|---|---|
| Molecular weight (g/mol) | 440.575 | Simcyp compound file |
| log P | 4.66 | Simcyp compound file |
| Compound type | Monoprotic Base | Simcyp compound file |
| pKa | 10.29 | Simcyp compound file |
| B/P | 0.675 | Simcyp compound file |
| fu | 0.083 | Simcyp compound file |
| Main plasma binding protein | Human serum albumin | Simcyp compound file |
| | | |
| $fu_{gut}$ | 1 | |
| | | |
| Distribution Model | Minimal PBPK Model | |
| $V_{SS}$ (L/kg) | 4.166812 | Predicted - Method 1 |
| Q (L/h) | 18 | |
| $V_{SAC}$ (L/kg) | 2 | |
| | | |
| Enzyme | CYP2C8 | Simcyp compound file |
| Pathway | D-620 | |
| $V_{max}$ (pmol/min/pmol) | 38.5 | |
| $K_m$ (µM) | 68 | |
| | | |
| Enzyme | CYP3A4 | Simcyp compound file |
| Pathway | D-620 | |
| $V_{max}$ (pmol/min/pmol) | 46 | |
| $K_m$ (µM) | 90 | |
| | | |
| Enzyme | CYP3A5 | Simcyp compound file |
| Pathway | D-620 | |
| $V_{max}$ (pmol/min/pmol) | 18.8 | |
| $K_m$ (µM) | 19.5 | |
| | | |
| Enzyme | CYP2C8 | Simcyp compound file |
| Pathway | D-715 | |

| | | |
|---|---|---|
| $V_{max}$ (pmol/min/pmol) | 113.2 | |
| $K_m$ (μM) | 59 | |
| | | |
| $CL_R$ (L/h) | 1.91 | Simcyp compound file |
| | | |
| Enzyme | CYP3A4 | Determined experimentally |
| $K_i$ (μM) | 0.27 | |
| $fu_{mic}$ | 0.78 | |
| $K_I$ (μM) | 0.28 | |
| $k_{inact}$ (1/h) | 2.44 | |
| $fu_{mic}$ | 0.78 | |
| | | |
| Enzyme | CYP2J2 | Determined experimentally |
| $K_i$ (μM) | 162 | |

**Supplemental Table 2.3.** Key input parameters for the PBPK model of ketoconazole

| **Parameter** | **Value** | **Method/Reference** |
|---|---|---|
| Molecular weight (g/mol) | 531.4 | Simcyp compound file |
| log P | 4.04 | Simcyp compound file |
| Compound type | Diprotic Base | Simcyp compound file |
| pKa | 2.94, 6.51 | Simcyp compound file |
| B/P | 0.62 | Simcyp compound file |
| fu | 0.029 | Simcyp compound file |
| Main plasma binding protein | Human serum albumin | Simcyp compound file |
| | | |
| $fu_{gut}$ | 0.06 | Simcyp compound file |
| | | |
| Distribution Model | Minimal PBPK Model | |
| $V_{SS}$ (L/kg) | 0.345 | Simcyp compound file |
| $CL_{po}$ (L/h) | 7.4 | Simcyp compound file |
| | | |
| $CL_R$ (L/h) | 0.147 | Simcyp compound file |
| | | |
| Enzyme | CYP2J2 | |
| $K_i$ (μM) | 0.082 | Determined experimentally |
| | | |
| Enzyme | CYP3A4 | |
| $K_i$ (μM) | 0.094 | Determined experimentally |
| | | |
| Transporter | ABCB1 (P-gp/MDR1) | |
| Organ | Gut | |
| $K_i$ (μM) | 0.17 | Determined experimentally |
| | | |
| Transporter | OAT3 | |
| Organ | Kidney | |
| $K_i$ (μM) | 0.01 | Optimized based on experimentally derived $IC_{50}$ of 15.77 μM and reported $IC_{50}$ of 0.86 μM with estrone-3-sulfate |

| | |
|---|---|
| | as the probe substrate (Vermeer *et al.*, 2016) |

**2 Model Verification – PK and Retrospective DDI Simulations**

**Supplemental Table 3.** Details of clinical study designs for PBPK model verification

| Reference Study | Dosing Regimen | Study conditions | Subjects |
|---|---|---|---|
| **(Greenblatt *et al.*, 2018)** | Rivaroxaban: Single dose of 20 mg on the mornings of day 1 and day 15<br><br>Extended Release Verapamil: 120 mg (Day 8), 240 mg (Day 9), 360 mg (Days 10-17) | Fed | Normal renal function: 13 Caucasians (Male/Female: 8/5)<br><br>Mild renal impairment: 14 Caucasians (Male/Female: 8/6)<br><br>Age: 38-72 |
| **(Kubitza, Becka, Mueck, Halabi, Maatouk, Klause, Lufft, Dominic D Wand, *et al.*, 2010)** | Single dose of 10 mg rivaroxaban | Fasted | Normal renal function: 8 Caucasians (Male/Female: 5/3)<br><br>Mild renal impairment: 8 Caucasians (Male/Female: 5/3)<br><br>Age: 36-69 |
| **(Mueck *et al.*, 2013)** | Rivaroxaban: 10 mg once daily (Days 1-10)<br>Ketoconazole: 400 mg once daily (Days 5-10) | Fed | 20 healthy Caucasian males<br><br>Age: 22-45 |
| **(Haeri *et al.*, 2014)** | Single dose of 80 mg verapamil | Fasted | 24 healthy volunteers (Male/Female: 12/12)<br><br>Age: 21-29 |
| **(Frishman and Lazar, 1992)** | Single dose of 120 mg controlled release verapamil capsule | Fasted | 28 patients with mild to moderate hypertension |

**Supplemental Table 4.** Serum creatinine input for mild renal impaired population

| | **GFR 30 to 60 mL/min Population in Simcyp** | | **GFR 50 to 79 mL/min Created Population** | |
|---|---|---|---|---|
| Age Group (years) | Serum Creatinine (μmol/L) | GFR (mL/min) | GFR (mL/min) | Serum Creatinine (μmol/L) |
| Male < 61 yo | 152 | 48.8 | 68.8 | 107.9 |
| Male > 61 yo | 143 | 51.9 | 71.9 | 103.2 |
| Female < 60 yo | 152 | 33.5 | 53.5 | 95.2 |
| Female > 60 yo | 148 | 34.4 | 54.4 | 93.6 |
| Female > 75 yo | 143 | 28.5 | 48.5 | 83.9 |

**Parameterizing the PBPK-DDI Models via *In Vitro* Inhibitory Parameters**

***In Vitro* Enzymatic and Transport Inhibition Assays.** The verified PBPK models of rivaroxaban, verapamil, norverapamil and ketoconazole were subsequently used for PBPK-DDI model development. Inhibition potencies ($K_i$ for reversible inhibition and $K_I$ and $k_{inact}$ for mechanism-based inhibition) were derived using rivaroxaban as the probe substrate (FDA/CDER, 2017).

**Chemicals.** High performance liquid chromatography (HPLC)-grade acetonitrile (ACN) was purchased from Tedia Company Inc (Fairfield, OH). Formic acid was purchased from BDH Chemicals (Radnor, PA). Ketoconazole, verapamil hydrochloride, prednisolone vetranal and dexamethasone were acquired from Sigma-Aldrich (St. Louis, MO). Norverapamil hydrochloride was purchased from Cayman Chemicals (Ann Arbor, MI). Human recombinant cytochrome P450 supersomes (rCYP) and NADPH regenerating system consisting of NADPH A ($NADP^+$ and glucose-6-phosphare) and B (glucose-6-phosphate dehydrogenase) were obtained from BD Gentest (Woburn, MA). All other reagents were of analytical grade.

**Mechanism-Based Inactivation of CYP3A4/2J2.** Incubations (n=3) were conducted in 96-well plates. In the primary inactivation incubation, either verapamil or norverapamil (0.1 to 5 µM or 2.5 µM for rCYP3A4 and rCYP2J2 respectively) were pre-incubated at 37°C for 5 min with rCYP3A4 (40 pmol/mL) or rCYP2J2 (20 pmol/mL) and NADPH B in potassium phosphate buffer (100 mM, pH 7.4). Reactions were initiated by the addition of 5 µL of NADPH A. The final primary incubation mixture had a total volume of 100 µL and the final organic concentration in the mixture was 1% ACN (v/v). At 0, 3, 8, 15, 22, 30 and 45 min after the addition of NADPH A, 5 µL of the primary incubation was transferred to 95 µL of the secondary incubation containing saturating rivaroxaban concentrations ([S]=50 µM >> $K_m$), effecting a 20× dilution. Apart from rivaroxaban, the secondary incubation mixture comprised the NADPH regenerating system and 100 mM potassium phosphate buffer (pH 7.4). The secondary incubation mixture was incubated for 2 h (rCYP3A4) or 30 min (rCYP2J2) at 37°C before an 80 µL aliquot was removed and quenched with an equal volume of ice-cold ACN containing 4 µM dexamethasone (internal standard). Quenched samples were subjected to centrifugation at 2755 *g*, 4°C for 30 min. Subsequently, the supernatants were removed for the determination of hydroxylated-rivaroxaban metabolite (main metabolite) by liquid chromatography tandem mass spectrometry (LC/MS/MS).

**Calculation of Inactivation Kinetic Parameters ($K_I$ and $k_{inact}$).** The natural logarithm of percentage of enzyme activity remaining versus inactivation pre-incubation time was plotted for each inactivator concentration and $k_{obs}$ values (apparent inactivation rate constants) were described as the negative slopes of the lines. Subsequently, a plot of observed inactivation rate constants ($k_{obs}$) against inactivator concentration [I] allowed for inactivation kinetic parameters, $K_I$ and $k_{inact}$ to be fitted with non-linear least squares regression using **eq. S13.**

$$k_{obs} = \frac{k_{inact} \times [I]}{K_I + [I]} \quad \textbf{(S13)}$$

**Reversible Inhibition of CYP3A4 and CYP2J2.** Incubations (n=3) were conducted in 96-well plates. Rivaroxaban (0.5 to 100 µM) was pre-incubated at 37°C for 5 min with rCYP3A4 (40 pmol/mL) and rCYP2J2 (20 pmol/mL), NADPHB and 100 mM potassium phosphate buffer (pH 7.4) in the presence of several concentrations of the test inhibitor (i.e. verapamil, norverapamil). The reactions were commenced by the addition of 5 µL NADPHA and the final mixture had a total volume of 100 µL comprising 1% ACN (v/v). Incubation was carried out for 2 h and 30 min for rCYP3A4 and rCYP2J2 respectively at 37°C and quenched with an equal volume of ice-cold ACN containing 4 µM dexamethasone (internal standard). The quenched samples were subjected to centrifugation at 2755 *g*, 4°C for 30 min. The same protocol was adopted to determine $IC_{50}$ of ketoconazole with rivaroxaban concentration at $K_m$ (10 µM). Subsequently, the supernatants were removed for the determination of hydroxylated-rivaroxaban metabolite (main metabolite) by LC/MS/MS.

**Calculation of Reversible Inhibition Parameters ($K_i$).** A series of Michaelis-Menten (substrate-velocity) curves were generated in the presence of various concentrations of the inhibitor. Lineweaver-Burk transformations were used to discern the type of inhibition that was exhibited by the inhibitor-enzyme interaction. The derived inhibition modality dictated the selection of appropriate equations to determine the $K_i$ value via non-linear regression analyses. $IC_{50}$ values computed from log(inhibitor) vs. response variable slope (four parameters) analysis were also corrected to $K_i$ based on the mode of inhibition identified (**eq. S17a** for competitive and **eq. S17b** for mixed mode inhibition)

$$IC_{50} = K_i \times (1 + \frac{[S]}{K_m}) \quad \textbf{(S17a)}$$

$$IC_{50} = \frac{Ki \times (1+\frac{[S]}{K_m})}{1+\frac{K_i}{K_i'} \times \frac{[S]}{K_m}} \quad \textbf{(S17b)}$$

**Inhibition of P-gp-mediated Efflux of Rivaroxaban.** The inhibitory potential of ketoconazole (0.1-50 µM) on the absorptive transport of rivaroxaban (10 µM) was assessed after the incubation period of 90 min. A model-based approach detailed by Kishimoto *et al* was used for calculation of the $IC_{50}$ value of ketoconazole (**eq. S18**) (Kishimoto *et al.*, 2016).

$$\frac{1}{CL_{AtoB,i}} - \frac{1}{CL_{AtoB(-P-gp)}} = \frac{PS_{P-gp,I=0}}{P_{pass}S_1 \times P_{pass}S_3} \times \frac{1}{1 + \frac{[I]_{cell,u}}{IC_{50}}} \quad \textbf{(S18)}$$

where $CL_{AtoB,i}$ and $CL_{AtoB(-P-gp)}$ represent the observed A to B clearance with inhibitor and complete P-gp inhibition respectively, $P_{pass}S_1$ and $P_{pass}S_3$ represent permeability-surface area products (PS) for influx across apical membrane and efflux across basolateral membrane of MDCK-MDR1 cell monolayers, $PS_{P-gp,I=0}$ represents PS of P-gp in the absence of inhibitor and is defined by $\frac{J_{max}}{K_m}$. $J_{max}$, $K_m$ *and* $P_{pass}$ estimates were derived from previous three-compartmental analysis. $[I]_{cell,u}$ represents the unbound intracellular ketoconazole concentrations obtained from three-compartmental modelling of ketoconazole's bidirectional transport at t = 90 min. All regression analyses were performed using GraphPad Prism version 7 (GraphPad Software, San Diego, CA).

**Inhibition of OAT3-mediated Uptake of Rivaroxaban.** Investigation of the potential inhibition of OAT3-mediated rivaroxaban uptake by ketoconazole and verapamil adhered to the protocol previously outlined by Vermeer *et al* (Vermeer *et al.*, 2016). Prior to addition of ketoconazole, OAT3-transfected HEK cells were washed once with HBSS containing 20 mM HEPES (pH 7.4). Subsequently, HBSS containing varying concentrations of ketoconazole and verapamil (0.1 – 100 µM) was added for 15 min. Following pre-incubation, inhibitor solutions were aspirated and replaced with HBSS containing the inhibitors (or solvent control, dimethylsulfoxide) and rivaroxaban (1 µM) probe substrate . After 5 min, cellular uptake was terminated by washing the cells twice with 200 µL of ice-cold PBS and lysed directly on the plate with 100% methanol containing internal standard. $IC_{50}$ values were determined from the average percent inhibition values fitted to log(inhibitor) vs. response variable slope (four parameters) analysis.

**Ultrafiltration in the Determination of Fraction Unbound.** To estimate the extent of non-specific binding of rivaroxaban (victim substrate) and inhibitors within the *in vitro* system, ultrafiltration was performed using the Centrifree® device. The calculated fraction unbound was subsequently used to correct the apparent kinetic and inhibition constants previously derived.

**Non-Specific Binding (NSB) of Substrates and Inhibitors to Centrifree Device.** Binding to the Centrifree tube sample reservoir and collection cup (as annotated in the diagram below) was determined by adding rivaroxaban 100 µM and the inhibitors (verapamil, norverapamil and ketoconazole) in protein free buffer (pH 7.4) directly to the reservoir (1000 µL) and cup (500 µL) followed by incubation for 20 min (Ballard and Rowland, 2011).

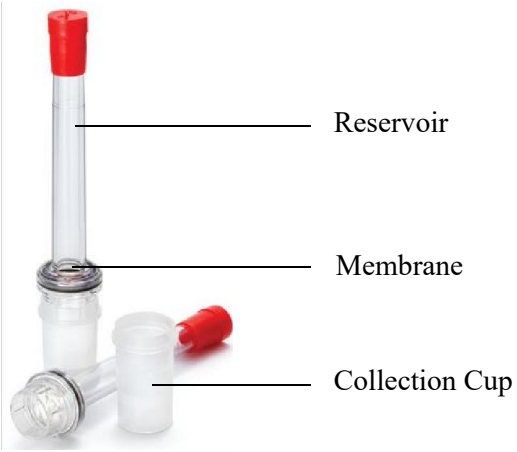


Centrifree device consisting of sample reservoir, membrane and collection cup.

Fraction unbound to the sample reservoir ($fu_R$) and collection cup ($fu_C$) was obtained using **eqs. S19a** and **S19b**.

$$fu_R = \frac{Cu_R}{C_{tot}} \quad \textbf{(19a)} \qquad fu_C = \frac{Cu_C}{C_{tot}} \quad \textbf{(19b)}$$

Where $Cu_R$, $Cu_C$ and $C_{tot}$ represent the unbound concentration of drug in the sample reservoir, collection cup and total concentration of test substrate respectively. Fraction unbound to the membrane, $fu_{mem}$, determined from a control filtration containing no protein in the supernatant, can be calculated using **eq. S20**.

$$fu_{mem} = \frac{Cu_C}{Cu_R \times fu_C} \quad \textbf{(S20)}$$

**Unbound Fraction of Rivaroxaban in Media and within the Cell.** Binding of rivaroxaban to culture media (DMEM + 10% FBS) and the MDCK-MDR1 cell homogenate was determined by the addition of rivaroxaban 100 µM to media and cell homogenate respectively. After incubation at 37℃ for 90 min, aliquots of the solutions were added to the reservoir, incubated for 20 min to ensure equilibration and subsequently centrifuged (2000 *g*) using a swing bucket for 30 min at 37℃. The ultrafiltrate was incubated for another 20 min to ensure equilibration with the collection cup. Both fraction unbound to DMEM ($fu_{media}$) as well as the diluted intracellular fraction unbound ($fu_{cell,d}$) were obtained using **eq. S21**.

$$fu_{media}/fu_{cell,d} = \frac{1}{1 + [\left(\frac{C_{tot,X} \times fu_{mem} \times fu_C}{Cu_{UF}}\right) - \frac{1}{fu_R}]} \quad \textbf{(S21)}$$

Where $C_{tot,X}$ represent the total concentration measured in DMEM or cell homogenate and $Cu_{UF}$ is the concentration measured in the ultrafiltrate (Ballard and Rowland, 2011).

***Calculation of $fu_{cell}$.*** $fu_{cell,d}$ that is determined under incubation conditions needs to be corrected by the dilution factor, D, to obtain the intrinsic undiluted $f_{u\,cell}$ (**Eq. S22**) (Riccardi *et al.*, 2018).

$$fu_{cell} = \frac{{}^1/_D}{\left(\left({}^1/_{fu_{cell,d}}\right) - 1\right) + {}^1/_D} \quad \textbf{(S22)}$$

Where D at $10 \times 10^6 cells/mL = \frac{Total\ suspension\ volume}{Cell\ volume}$ and $Cell\ volume = \frac{4}{3}\pi(\frac{Cell\ diameter}{2})^3$

**Unbound Fraction of Verapamil, Norverapamil and Ketoconazole in the *In Vitro* Enzymatic Incubation.** Binding of the inhibitors (1 μM) in the enzymatic incubation containing 40 pmol/mL of rCYP3A4 or 20 pmol/mL of rCYP2J2 was determined via the same protocol defined above.

**Sample Processing for LC/MS/MS Quantitation**

**Efflux Assay**. A calibration curve was built using 0.001, 0.005, 0.01, 0.1, 0.3, 0.5, 0.75, 1, 2, 5 μM of rivaroxaban. For sample concentrations above 5 μM, samples were diluted using media before sample processing to minimize any matrix effects during quantitation. To ascertain accuracy, quality control (QC) samples were prepared in triplicates using a similar method where low and high QCs were 0.05 and 3.5 μM respectively. To account for chemical degradation that might have occurred during the cell assay, the calibrants were also exposed at room temperature for the same duration as the transport assay. For rivaroxaban samples, calibration standards and controls, the samples were spiked with 2.02 μL of 50 μM prednisolone (IS) and subjected to a 2-step liquid-liquid extraction (LLE). In the first extraction, 1 mL of methyl tert butyl ether (MTBE) was aliquoted into each tube and vortexed at high speed for 5 min. Samples were then centrifuged using a microfuge at 18 000 *g* for 5 min at 4°C to ensure complete separation of the media from the extraction solvent. 800 μL of MTBE was carefully aliquoted from each tube to a corresponding 2 mL Eppendorf tube. For the second extraction, another 500 μL of MTBE was added, vortexed and spun down in a similar manner before 600 μL of MTBE was aliquoted and added to the same corresponding tube. The extraction solvent was then dried down in a turbovap using nitrogen gas at 3-5 psi before reconstitution in 100 μL of a 0.1% formic acid in ACN and 0.1% formic acid in water mixture (85:15 v/v) for LC/MS/MS analysis.

**Uptake Assay.** For *in vitro* studies of rivaroxaban uptake, the matrix was a mammalian cell lysate derived from HEK293 cells. Confluent monolayers were lysed with 100 μL of ice-cold methanol/cm$^2$ for 1 h before centrifugation at 18000 *g* for 15 min to pellet precipitated protein. Culture lysates were spiked with rivaroxaban working solutions to obtain final rivaroxaban concentrations of 0,0025, 0,005, 0.0125, 0.025, 0.05, 0.1, 0.25, 0.75, 1, 2 and 2.5 μM, containing the IS prednisolone at a concentration of 1 μM. QC samples were prepared independently at concentrations of 0.01 (low), 0.5 (medium) and 1.5 (high) μM of rivaroxaban.

**NSB Assay.** Collected samples were quenched by the addition of ACN containing 1 μM of prednisolone as IS. All samples were centrifuged at 4℃, 18000 *g* for 30 min and the supernatant was subjected to LCMS/MS analysis.

**LC/MS/MS Quantitation**

All samples were analysed using an Agilent 1290 Infinity ultra-high pressure liquid chromatography (UHPLC) (Agilent Technologies Inc., Santa Clara, CA, USA) interfaced with the AB SCIEX QTRAP 5500 tandem mass spectrometry (MS/MS) system (AB SCIEX, Framingham, MA, USA). The ACQUITY UPLC BEH $C_{18}$, 1.7 µM, 2.1 × 50 mm column (Waters, Mildord, MA, USA) was used for chromatographic separation. Samples were delivered using injection volumes of 1-4 µL. The aqueous mobile phase (A) was 0.1% formic acid in milli-Q water whereas the organic mobile phase (B) consisted of 0.1% formic acid in ACN. Mobile phases were delivered at a flow rate of 0.6 ml/min. The column was maintained at 45°C.

**Transport Assay**. The gradient program for rivaroxaban, propranolol, quinidine and prednisolone was as follows: linear gradient from 15 % to 85 % B (0-1.2 min), isocratic at 100 % B (1.21-2 min), linear gradient from 100 % to 15 % B (2-2.01 min) and isocratic at 15 % B (2.01-2.5 min).

**Enzymatic Inhibition Assay.** The gradient program for hydroxylated rivaroxaban metabolite and dexamethasone was as follows: linear gradient from 20% B to 80% B (0-1.2 min), isocratic at 100% B (1.21–2 min), linear gradient from 100% to 20% B (2-2.01 min) and isocratic at 20% B (2.01 – 2.5 min).

**Transport Inhibition Assay**. The gradient program for rivaroxaban, ketoconazole and prednisolone was as follows: linear gradient from 30 % to 70 % B (0 – 1.2 min), isocratic at 100 % (1.21 – 2 min) and isocratic at 20 % B (2.01 – 2.5 min).

**NSB to PBS, DMEM culture media and cell homogenates.** The gradient program for rivaroxaban, ketoconazole and prednisolone was as follows: linear gradient from 15% to 85% B (0 – 1.2 min), isocratic at 100% B (1.21 – 2 min) and isocratic at 15% B (2.01 – 2.5 min).

The MS source conditions were: source temperature 500 °C, curtain gas 30 psi, ion source gas 1 (sheath gas) 25 psi, ion source gas 2 (drying gas) 25 psi, ion spray voltage +5000V, collision gas (nitrogen) medium. All analyses were performed in ESI positive mode. Acquisition and analysis of data were performed with Analyst software ver. 1.6.2 (Applied Biosystems). For all LC/MS/MS analyses, the peak area of the analyte was expressed as a ratio to the peak area of the internal standard. The MRM transitions and compound dependent MS parameters of the analytes are summarized in the following table.

**Optimized compound-specific MS parameters for LC/MS/MS analysis**

| Compound | MRM Transition (*m/z*) | Collision Energy (CE) (*V*) | Declustering Potential (DP) (*V*) | Entrance Potential (EP) (*V*) | Collision Exit Potential (CXP) (*V*) | Dwell Time (ms) |
|---|---|---|---|---|---|---|
| Rivaroxaban | 436.200→145.000 | 33 | 95 | 10 | 9 | 100 |
| Rivaroxaban Metabolite | 452.200→406.100 | 25 | 100 | 10 | 9 | 100 |
| Ketoconazole | 531.200→489.200 | 40 | 103 | 9 | 25 | 100 |
| Quinidine | 325.300→172.100 | 27 | 100 | 7 | 6 | 100 |
| Propranolol | 260.300→116.200 | 23 | 45 | 11 | 6 | 100 |
| Estrone-3-Sulfate (E3S) | 349.200→269.200 | -40 | -116 | -11 | -8 | 100 |
| Pregnenolone Sulfate (IS for E3S) | 395.300→97.000 | -79 | -136 | -8 | -6 | 100 |
| Para-aminohippuric acid (PAH) | 195.300→120.200 | 18 | 34 | 7 | 8 | 100 |
| Acetaminophen (IS for PAH) | 152.100→110.000 | 23 | 64 | 12 | 8 | 100 |
| Prednisolone | 361.200→147.000 | 29 | 100 | 6 | 9 | 100 |
| Dexamethasone | 393.200→355.100 | 14 | 112 | 4 | 14 | 100 |

## Supplemental Results

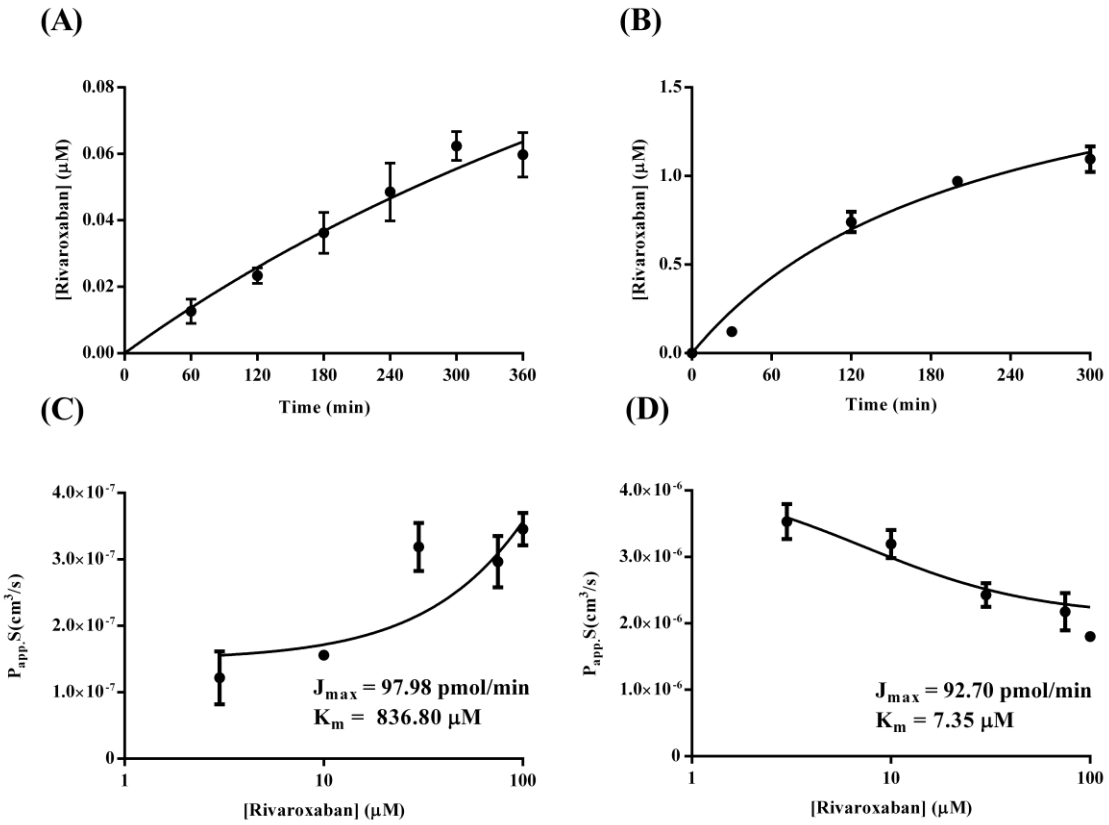


**Supplemental Fig 2.** Investigation of the P-gp-mediated transport kinetics of rivaroxaban. Time-dependent (**A**) A to B and (**B**) B to A transport of rivaroxaban. Both graphs were fitted with nonlinear regression Michaelis-Menten models. Concentration-dependent (**C**) A to B and (**D**) B to A transport of rivaroxaban was investigated at 180 min and 120 min respectively. Fitting of concentration-dependent absorptive and secretory clearances using **eqs. S8** and **S9** yielded $J_{max,app}$ and $K_{m,app}$ values. Each point represents the mean of triplicate determinations.

**Supplemental Table 5.** Non-specific binding of rivaroxaban and ketoconazole to ultrafiltration apparatus, culture media and cell homogenate.

| | ***Rivaroxaban*** | ***Ketoconazole*** |
|---|---|---|
| ***fuR*** | 0.94 | 0.80 |
| ***fuC*** | 0.90 | 1 |
| $fu_{mem}$ | 0.88 | 0.49 |
| $fu_{media}$ | 1 | 0.57 |
| $fu_{cell}$ | 0.023 | 0.01 |
| ***Cell diameter (µm)*** | 13.6 | 13.6 |
| ***Cell volume (µL/million cells)*** | 1.317 | 1.317 |
| ***D*** | 75.9 *at* $10 \times 10^6$ *cells/mL* | 25.3 *at* $30 \times 10^6$ *cells/mL* |

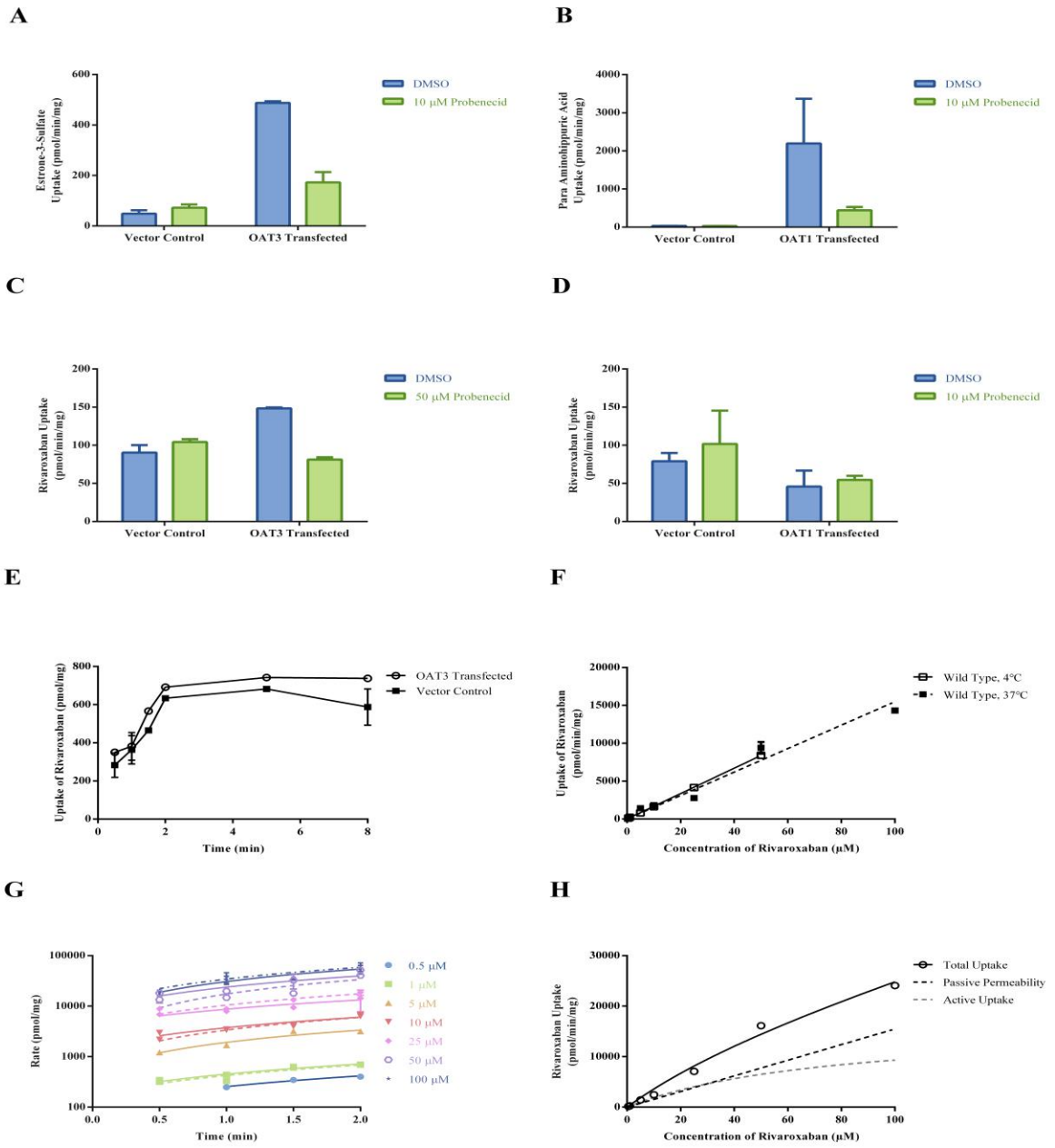


**Supplemental Fig. 3.** Investigation of the hOAT-mediated uptake transport kinetics of rivaroxaban. Uptake for 5 min by wild type HEK293 cells and those stably expressing hOAT3/1 was determined at 37°C for (**A**) estrone-3-sulfate (2 µM) and (**B**) para-aminohippuric acid (3 µM) to verify uptake functionality. Uptake of rivaroxaban (1 µM) in the absence and presence of prototypical OAT inhibitor, probenecid was subsequently investigated in (**C**) hOAT3-expressing HEK293 cells compared to wild type cells and (**D**) hOAT1-expressing HEK293 cells compared to wild type cells. Time course of uptake kinetics in wild type and OAT3-transfected cells is presented in (**E**). Time-dependent passive permeability up to 2 min was determined across 0.5 to 100 µM of rivaroxaban in wild type cells at both 4°C and 37°C (data not shown). Uptake rates obtained in wild type cells were plotted against rivaroxaban concentration in (**F**) to obtain the passive diffusion clearance ($CL_{PD}$) via linear regression (**eq. S13**). (**G**) Time-dependent total uptake up to 2 min was also quantified across 0.5 to 100 µM of rivaroxaban in OAT3-transfected HEK cells at 37°C. (**H**) Total uptake (black solid line) in OAT3-transfected HEK cells was analyzed via non-linear regression (**eq. 14**), and active uptake (grey dashed line) was obtained after subtracting the passive diffusion component (black dashed line) determined in wild type HEK cells. Uptake experiments carried out in (**E-H**) are represented as the mean ± SD of two experiments. All other data are results from a single experiment carried out in triplicate.

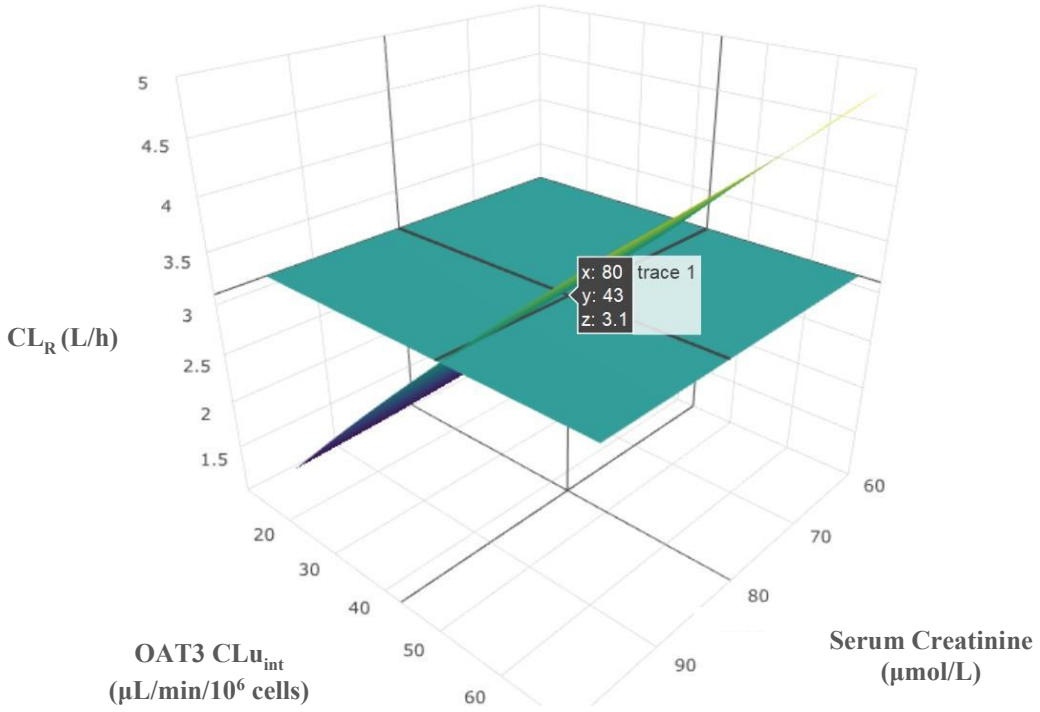


**Supplemental Fig. 4.** Top-down optimization of the OAT3-mediated basolateral uptake of rivaroxaban. Estimates of OAT3 $CLu_{int}$ were obtained via a sensitivity analysis approach and was defined to be 43 µL/min/$10^6$ cells where simulated $CL_R$ converged with the weighted mean $CL_R$ of 3.1L/h when serum creatinine was fixed at 80 µmol/L (healthy volunteers).

**Supplemental Table 6.** Comparison of PK parameters between simulated and observed data for model verification of verapamil and norverapamil

| | **Simulated (n=200)** | **Observed (n=20)** |
|---|---|---|
| **Verapamil 80 mg** | **AUC (µg.h/L)** | **AUC (µg.h/L)** |
| **Geometric mean** | 404 | 389 |
| **CV (%)** | 45 | 66 |
| **Ratio of simulated/observed** | 1.04 | |
| **Success criteria for ratio of simulated/observed** | 0.58-1.73 | |
| | **Simulated (n=200)** | **Observed (n=20)** |
| **Norverapamil 80 mg** | **AUC (µg.h/L)** | **AUC (µg.h/L)** |
| **Geometric mean** | 722 | 674 |
| **CV (%)** | 42 | 38 |
| **Ratio of simulated/observed** | 1.07 | |
| **Success criteria for ratio of simulated/observed** | 0.72-1.39 | |

AUC, area under the concentration-time curve from time zero to infinity; CV, coefficient of variation

**Supplemental Table 7.** Comparison between Simcyp and experimental inhibitory parameters

| | | **Simcyp (Index substrate)** | | | **Experimental (Rivaroxaban Substrate)** | | |
|---|---|---|---|---|---|---|---|
| *In vitro* parameter | | V | NV | K | V | NV | K |
| MBI on CYP3A4 | $K_I$ (μM) | 2.21 | 10.3 | - | 1.653 | 0.284 | - |
| | $k_{inact}$ ($h^{-1}$) | 2 | 18 | - | 3.924 | 2.440 | - |
| | Potency | 0.90 | 1.74 | - | 2.37 | 8.59 | - |
| Reversible Inhibition on CYP3A4 | $K_i$ (μM) | - | - | 0.015 | 0.487 | 0.270 | 0.094 |
| Fraction Unbound | $fu_{inc}$ | 1 | 1 | 1 | 0.67 | 0.78 | 1 |

V, verapamil; NV, norverapamil; K, ketoconazole

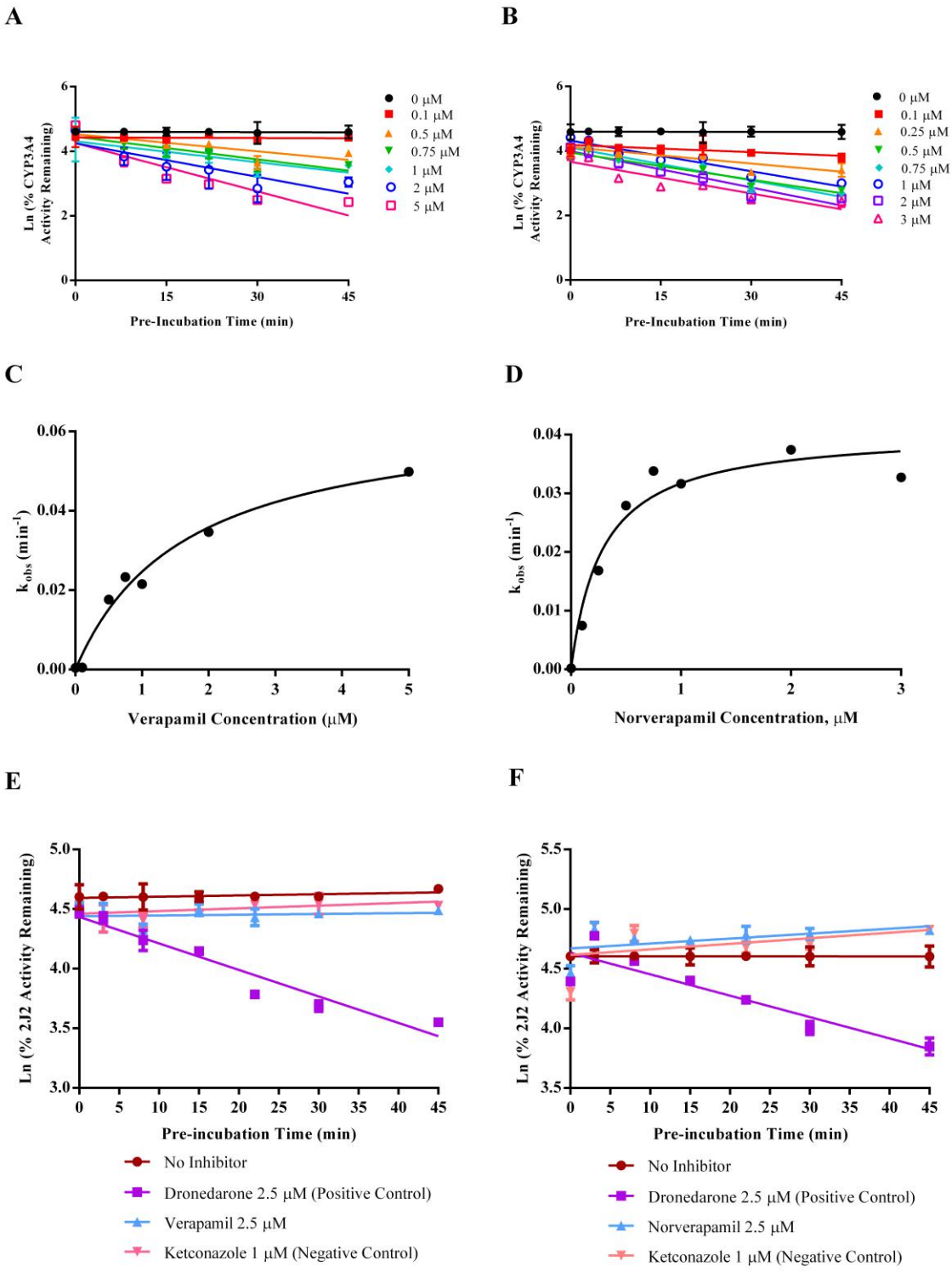


**Supplemental Fig. 5.** MBI of CYP3A4 and CYP2J2-mediated metabolism of rivaroxaban by verapamil and norverapamil. Semi-logarithmic plots demonstrate time- and concentration-dependent inhibition of CYP3A4 by **(A)** verapamil and **(B)** norverapamil using rivaroxaban as probe substrate and enabled the determination of pseudo-first order rates of inactivation ($k_{obs}$) at various verapamil and norverapamil concentrations. In **(C)** and **(D)**, the relationship between $k_{obs}$ values determined from **(A)** and **(B)** and inhibitor concentration was further investigated via non-linear regression analysis to derive inactivation kinetic constants, $K_I$ and $k_{inact}$. In contrast, time-dependent decrease in CYP2J2 activity across pre-incubation times was not apparent with verapamil (**E**) and norverapamil (**F**) as the putative inhibitors. Each point in the semi-logarithmic plots represents the mean of triplicate determinations.

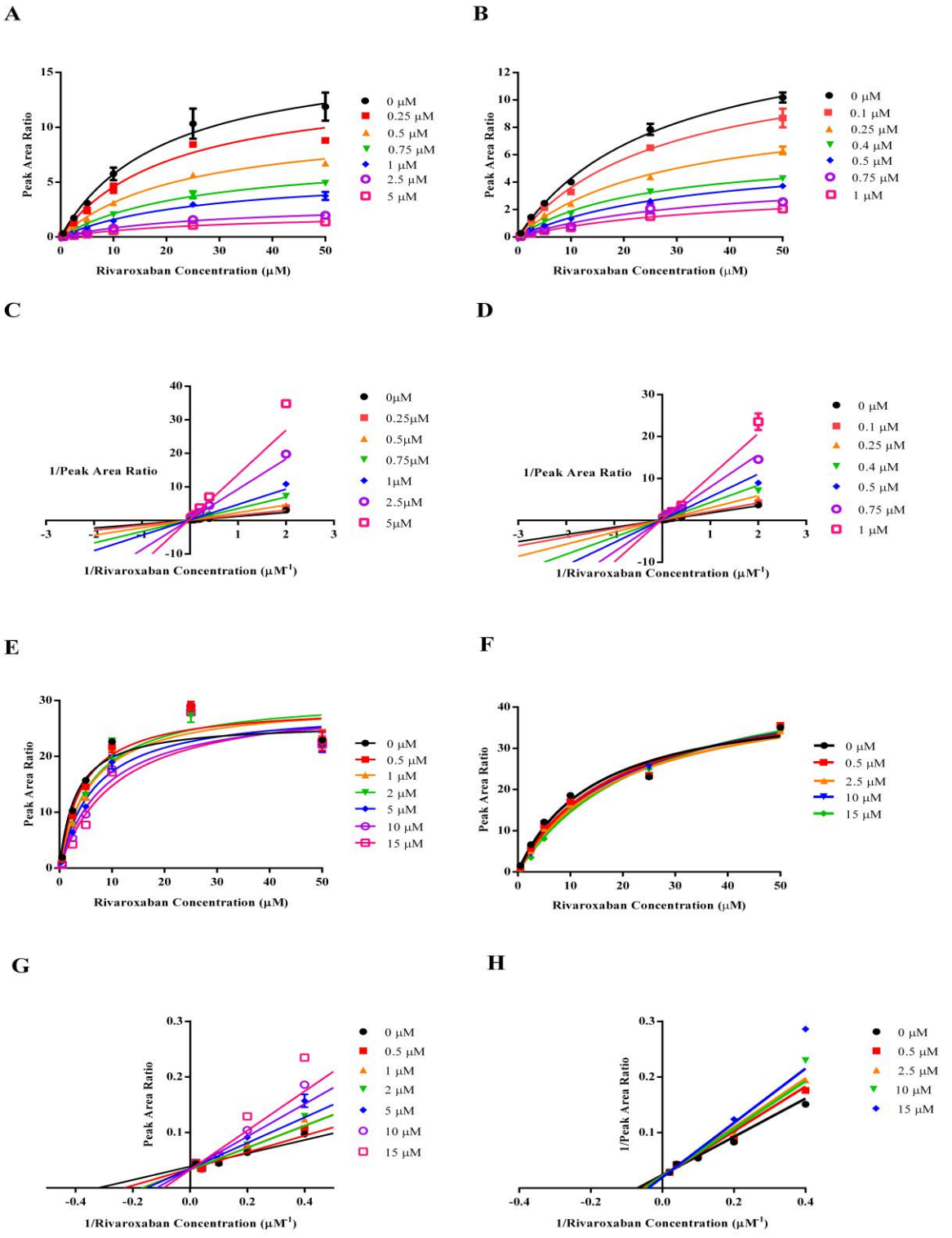


**Supplememtal Fig. 6.** Reversible inhibition of CYP3A4 and CYP2J2-mediated metabolism of rivaroxaban by verapamil and norverapamil. Michaelis-Menten plots illustrate reversible inhibition of CYP3A4 and CYP2J2 in the presence of (**A and E**) verapamil as well as (**B and F**) norverapamil. Data from (**A, B, E and F**) were transformed to corresponding Lineweaver-Burk plots in to reveal mixed mode inhibition of CYP3A4 in (**C, D**) and competitive inhibition of CYP2J2 in (**G, H**) when rivaroxaban was used as the probe substrate. Each point represents the mean of triplicate determinations.

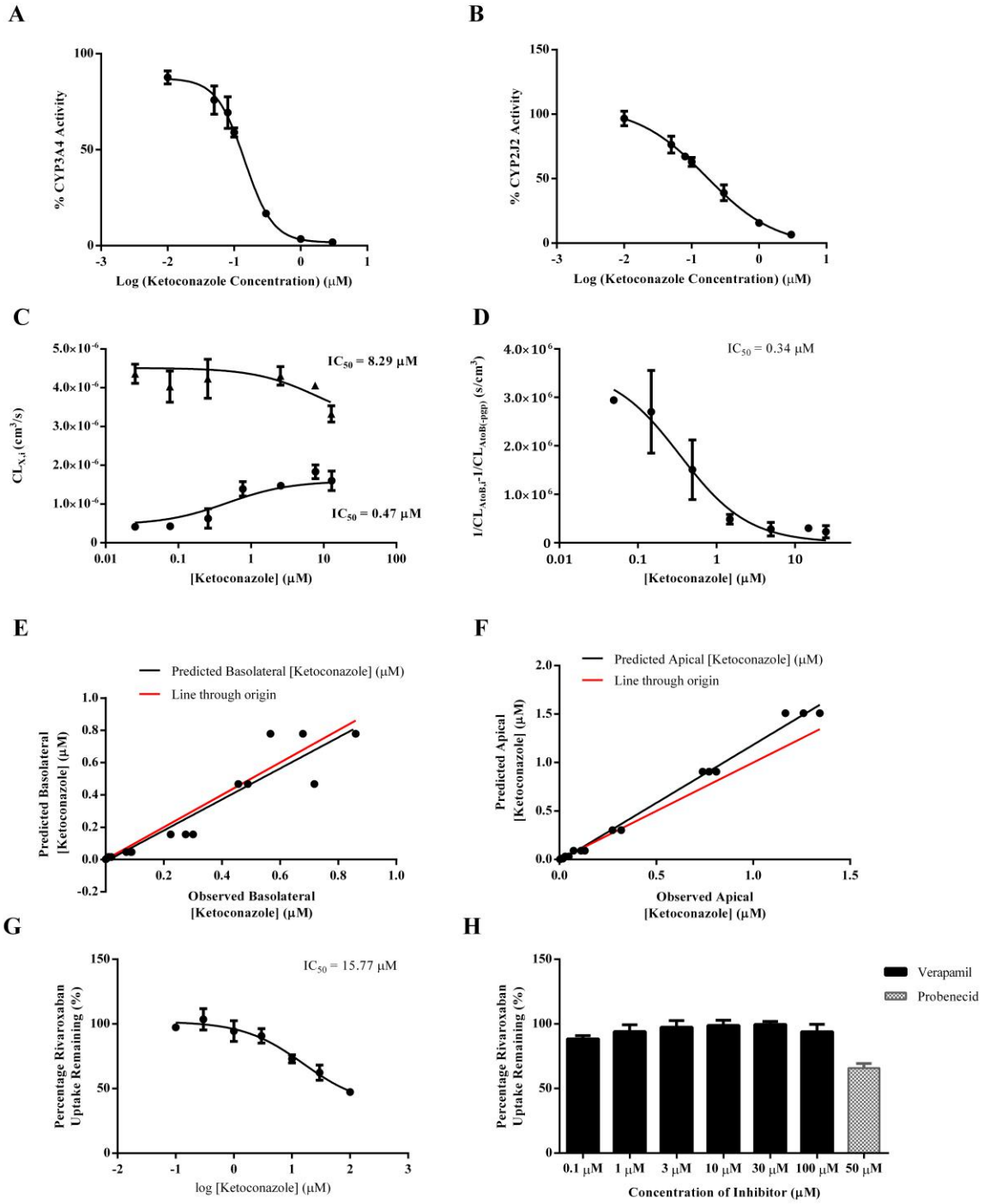


**Supplemental Fig. 7.** Inhibition of the enzyme and transporter-mediated elimination of rivaroxaban by ketoconazole and verapamil. (**A and B**) represent *in vitro* $IC_{50}$ curves used to quantify the reversible inhibition of CYP3A4- and CYP2J2-mediated metabolism of rivaroxaban respectively. (**C and D**) illustrate the inhibitory effects of intracellular unbound concentrations of ketoconazole on the $CL_{AtoB,i}$; $CL_{BtoA,i}$ and $1/CL_{AtoB,i}$ - $1/CL_{AtoB}$(-P-gp) values of rivaroxaban. Intracellular unbound concentrations derived from three compartmental modeling were verified via assessing the goodness of fit between measured versus predicted ketoconazole concentrations in the (**E**) basolateral and (**F**) apical compartments of the transwell apparatus. The *in vitro* $IC_{50}$ values describing the inhibition of the P-gp-mediated efflux of rivaroxaban by ketoconazole was converted to the inhibition constant $K_i$ by applying the Cheng Prusoff equation (eq. S14a) assuming competitive inhibition. (**G and H**) illustrate the inhibitory effects of ketoconazole and verapamil respectively on the OAT3-mediated uptake of rivaroxaban into HEK cells. Inhibition experiments performed in (**G**) is represented as the mean ± SD of two experiments. All other data are results from a single experiment carried out in triplicate.

**A**

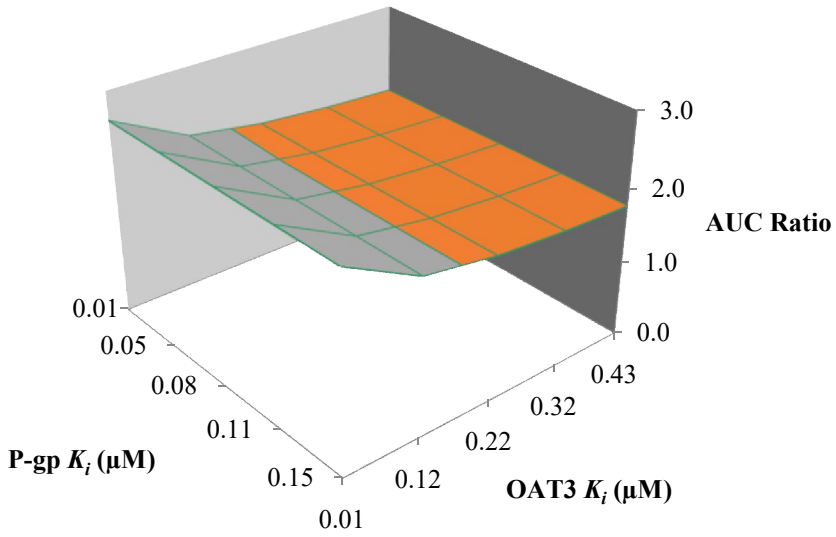
3.0
2.0
AUC Ratio
1.0
0.0
0.01
0.05
0.08
0.11
0.15
P-gp $K_i$ (µM)
0.01
0.12
0.22
0.32
0.43
OAT3 $K_i$ (µM)

**B**

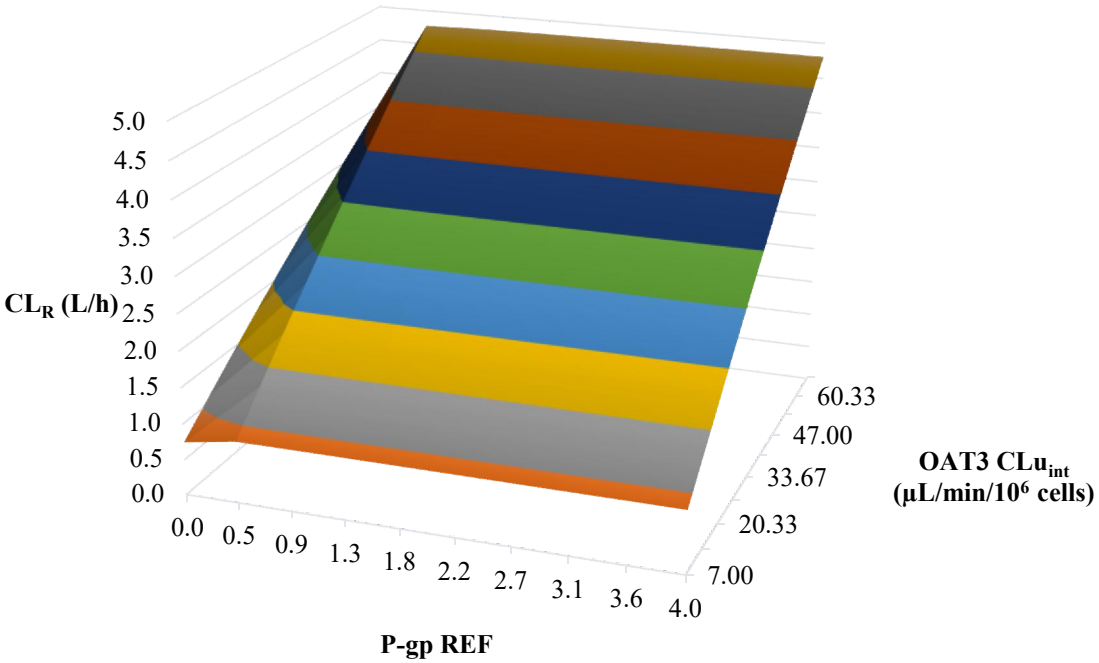
5.0
4.5
4.0
3.5
3.0
2.5
2.0
1.5
1.0
0.5
0.0
$CL_R$ (L/h)
0.0
0.5
0.9
1.3
1.8
2.2
2.7
3.1
3.6
4.0
P-gp REF
60.33
47.00
33.67
20.33
7.00
OAT3 $CLu_{int}$ (µL/min/$10^6$ cells)

**C**

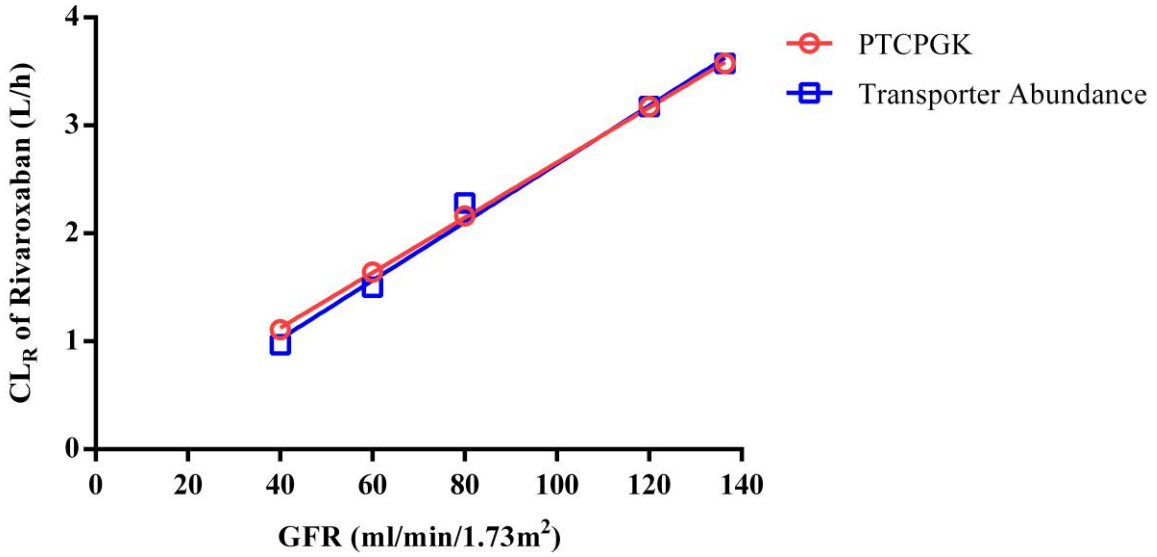


**Supplemental Fig. 8.** (**A**) Simulated rivaroxaban AUC ratio at different input values of OAT3 $K_i$ and P-gp $K_i$. (**B**) Simulated rivaroxaban $CL_R$ at different input values of OAT3 $CL_{int,T}$ and P-gp REF. Values of OAT3 $CL_{int,T}$, P-gp REF, OAT3 $K_i$ and P-gp $K_i$ were varied using the automated sensitivity analysis tool in the Simcyp simulator in a population representative following the clinical trial design reported by (Mueck *et al.*, 2013). (**C**) Predicting the effect of various physiological changes (either reductions in PTCPGK or transporter abundance) characterizing mild and moderate renal impairment on the $CL_R$ of rivaroxaban

**Supplemental Table 8.** Comparison of **(A)** clinically observed renal clearance with simulated renal clearances of rivaroxaban using the **(B)** 35-compartment mechanistic kidney model versus **(C)** MechKiM module within the Simcyp simulator

| $f_{u,p}$ | Reported Apparent Permeability ($10^{-6}$ cm/s) | $CL_{api,scr}$ (L/h)[a] | $CL_{bsl,scr}$ (L/h)[a] | Observed $CL_R$ (L/h) (A) | Simulated $CL_R$ (L/h)[b] (B) | Simulated $CL_R$ (Mech KiM) (L/h)[b] (C) | Fold difference |
|---|---|---|---|---|---|---|---|
| **0.065** | 21.8 (Caco-2) | 0 | 0 | 3.1 | 0.27 | | |
| | 12.7 (L-MDR1) | | | | 0.32 | | |
| | 25.8 (LLC-PK1) | | | | 0.26 | | |
| | 12.88 (MDCK-MDR1) | | | | 0.32 | 0.35 | B/C = 0.91 |
| **0.065** | 12.88 (MDCK-MDR1) | 42.3 | 0 | 3.1 | 0.37 | 0.35 | B/A = 0.12 |
| **0.065** | 12.88 (MDCK-MDR1) | 42.3 | 52.9 | 3.1 | 4.4 | 3.26 | B/A = 1.41<br>C/A = 1.05 |

[a] Prediction of *in vivo* rivaroxaban basolateral and apical secretion clearances based on *in vitro* transporter data (**Supplemental Table 1**) using scaling factors of 60 million proximal tubule cells per gram kidney and 341.5 g of kidney per person.

[b] Renal clearance was calculated as the steady state urinary excretion rate (amount of drug excreted into the urine in a unit time) divided by the plasma rivaroxaban concentration at steady state.

**Supplemental Table 9:** Physiological changes in renal impairment

| GFR (mL/min/1.73m$^2$) | Tubular Flow (L/h) (Percentage of Cardiac Output)[a] | OAT3 Abundance[b] | P-gp Abundance[b] | PTCPGK[b] |
|---|---|---|---|---|
| **136.4** | 59.0 | 1 | 1 | 60 |
| **120** | 59.0 | 0.88 | 0.88 | 52.8 |
| **80** | 59.0 | 0.59 | 0.59 | 35.2 |
| **60** | 54.6 | 0.44 | 0.44 | 26.4 |
| **40** | 54.6 | 0.29 | 0.29 | 17.6 |

Reduction in both filtration and secretion was performed to represent changes in renal impairment. Simulated population representative of the healthy "NEurCaucasian" population available in Simcyp population had an age, weight, and body surface area of 58 years, 82 kg, and 1.97 m$^2$ respectively.

[a]Cardiac output for the population representative was defined as CO = BSA×60×(3-0.01*(age-20)). Tubular flow was defined as 19% of cardiac output for a healthy population (GFR > 80 mL/min/1.73 m$^2$), 17.67% of cardiac output for GFR 30-60 mL/min/1.73m$^2$ and 16.98% for GFR < 30 mL/min/m$^2$

[b]Relative change in GFR for each scenario was calculated using the value of 136.4 ml/ min/m$^2$ as baseline and applied to the OAT3 abundance, P-gp abundance or PTCPGK parameter. Reductions in renal transporter expression was represented in MechKiM by assigning relative abundances for the OAT3 and P-gp transporters in kidney in the "poor transporter" (PT) phenotype as a proportion of the Simcyp "extensive transporter" phenotype value of 1 and setting the frequency of PT in the modified population to 1 (Scotcher *et al.*, 2017). Changes were applied equally to each of the 3 sub-regions of the proximal tubule.

## REFERENCES


Ballard P, and Rowland M (2011) Correction for nonspecific binding to various components of ultrafiltration apparatus and impact on estimating in vivo rat clearance for a congeneric series of 5-ethyl,,5-n-alkyl barbituric acids. *Drug Metab Dispos* **39**:2165–2168.

Brouwer KLR, Keppler D, Hoffmaster KA, Bow DAJ, Cheng Y, Lai Y, Palm JE, Stieger B, and Evers R (2013) In Vitro Methods to Support Transporter Evaluation in Drug Discovery and Development. *Clin Pharmacol Ther* **94**:95–112.

Dias C, Moore KT, Murphy J, Ariyawansa J, Smith W, Mills RM, and Weir MR (2016) Pharmacokinetics, Pharmacodynamics, and Safety of Single-Dose Rivaroxaban in Chronic Hemodialysis. *Am J Nephrol* **43**:229–236.

Ellens H, Johnson M, Lawrence SK, Watson C, Chen L, and Richards-Peterson LE (2017) Prediction of the transporter-mediated drug-drug interaction potential of dabrafenib and its major circulating metabolites. *Drug Metab Dispos* **45**:646–656.

FDA/CDER (2017) In Vitro Metabolism- and Transporter- Mediated Drug-Drug Interaction Studies Guidance for Industry. *FDA Guid*.

Frishman WH, and Lazar EJ (1992) Sustained-release verapamil formulations for treating hypertension. *J Clin Pharmacol* **32**:455–62.

Gnoth MJ, Buetehorn U, Muenster U, Schwarz T, and Sandmann S (2011) In vitro and in vivo P-glycoprotein transport characteristics of rivaroxaban. *J Pharmacol Exp Ther* **338**:372–380.

Greenblatt DJ, Patel M, Harmatz JS, Nicholson WT, Rubino CM, and Chow CR (2018) Impaired Rivaroxaban Clearance in Mild Renal Insufficiency With Verapamil Coadministration: Potential Implications for Bleeding Risk and Dose Selection. *J Clin Pharmacol* **58**:533–540.

Haeri A, Javadian B, Saadati R, and Dadashzadeh S (2014) Metabolite parameters as an appropriate alternative approach for assessment of bioequivalence of two verapamil formulations. *Iran J Pharm Res IJPR* **13**:383–9, Shahid Beheshti University of Medical Sciences.

Kishimoto W, Ishiguro N, Ludwig-Schwellinger E, Ebner T, Maeda K, and Sugiyama Y (2016) Usefulness of A Model-Based Approach for Estimating In Vitro P-Glycoprotein Inhibition Potency in a Transcellular Transport Assay. *J Pharm Sci* **105**:891–896.

Kreutz R, Persson PB, Kubitza D, Thelen K, Heitmeier S, Schwers S, Becka M, and Hemmrich M (2017) Dissociation between the pharmacokinetics and pharmacodynamics of once-daily rivaroxaban and twice-daily apixaban: a randomized crossover study. *J Thromb Haemost* **15**:2017–2028.

Kubitza D, Becka M, Mueck W, Halabi A, Maatouk H, Klause N, Lufft V, Wand Dominic D, Philipp T, and Bruck H (2010) Effects of renal impairment on the pharmacokinetics, pharmacodynamics and safety of rivaroxaban, an oral, direct Factor Xa inhibitor. *Br J Clin Pharmacol* **70**:703–712.

Kubitza D, Becka M, Mueck W, Halabi A, Maatouk H, Klause N, Lufft V, Wand Dominic D., Philipp T, and Bruck H (2010) Effects of renal impairment on the pharmacokinetics, pharmacodynamics and safety of rivaroxaban, an oral, direct Factor Xa inhibitor. *Br J Clin Pharmacol* **70**:703–712.

Kubitza D, Becka M, Roth A, and Mueck W (2013) The influence of age and gender on the pharmacokinetics and pharmacodynamics of rivaroxaban-an oral, direct factor xa inhibitor. *J Clin Pharmacol* **53**:249–255.

Kubitza D, Roth A, Becka M, Alatrach A, Halabi A, Hinrichsen H, and Mueck W (2013) Effect of hepatic impairment on the pharmacokinetics and pharmacodynamics of a single dose of rivaroxaban, an oral, direct Factor Xa inhibitor. *Br J Clin Pharmacol* **76**:89–98.

Mathialagan S, Piotrowski MA, Tess DA, Feng B, Litchfield J, and Varma M V. (2017) Quantitative prediction of human renal clearance and drug-drug interactions of organic anion transporter substrates using in vitro transport data: A relative activity factor approach. *Drug Metab Dispos* **45**:409–417.

Mathialagan S, Rodrigues AD, and Feng B (2017) Evaluation of Renal Transporter Inhibition Using Creatinine as a Substrate In Vitro to Assess the Clinical Risk of Elevated Serum Creatinine. *J Pharm Sci* **106**:2535–2541.

Moore KT, Vaidyanathan S, Natarajan J, Ariyawansa J, Haskell L, and Turner KC (2014) An open-label study to estimate the effect of steady-state erythromycin on the pharmacokinetics, pharmacodynamics, and safety of a single dose of rivaroxaban in subjects with renal impairment and normal renal function. *J Clin Pharmacol* **54**:1407–1420.

Mueck W, Kubitza D, and Becka M (2013) Co-administration of rivaroxaban with drugs that share its elimination pathways: pharmacokinetic effects in healthy subjects. *Br J Clin Pharmacol* **76**:455–466.

Polli JW, Humphreys JE, Harmon KA, Castellino S, Mara MJO, Olson KL, John-williams LS, Koch KM, and Serabjit-singh CJ (2008) The Role of Efflux and Uptake Transporters in N - { 3-Chloro-4- [( 3-fluorobenzyl ) oxy ] phenyl } -6- [ 5- ({[ 2- ( methylsulfonyl ) ethyl ] amino } methyl ) -2-furyl ] -4-quinazolinamine ( GW572016 , Lapatinib ) Disposition and Drug Interactions. **36**:695–701.

Popović-Nikolić MR, Popović G V., and Agbaba DD (2017) The Effect of Nonionic Surfactant Brij 35 on Solubility and Acid-Base Equilibria of Verapamil. *J Chem Eng Data* **62**:1776–1781.

Riccardi K, Ryu S, Lin J, Yates P, Tess D, Li R, Singh D, Holder BR, Kapinos B, Chang G, and Di L (2018) Comparison of Species and Cell-Type Differences in Fraction Unbound of Liver Tissues, Hepatocytes, and Cell Lines. *Drug Metab Dispos* **46**:415–421.

Shirasaka Y, Sakane T, and Yamashita S (2008) Effect of P-glycoprotein expression levels on the concentration-dependent permeability of drugs to the cell membrane. *J Pharm Sci* **97**:553–565, Elsevier Masson SAS.

Stampfuss J, Kubitza D, Becka M, and Mueck W (2013) The effect of food on the absorption and pharmacokinetics of rivaroxaban. *Int J Clin Pharmacol Ther* **51**:549–561.

Troutman MD, and Thakker DR (2003) Efflux ratio cannot assess P-glycoprotein-mediated attenuation of absorptive transport: Asymmetric effect of P-glycoprotein on absorptive and secretory transport across Caco-2 cell monolayers. *Pharm Res* **20**:1200–1209.

Vermeer LMM, Isringhausen CD, Ogilvie BW, and Buckley DB (2016) Evaluation of Ketoconazole and Its Alternative Clinical CYP3A4/5 Inhibitors as Inhibitors of Drug Transporters: The In Vitro Effects of Ketoconazole, Ritonavir, Clarithromycin, and Itraconazole on 13 Clinically-Relevant Drug Transporters. *Drug Metab Dispos* **44**:453–459.

Volpe DA (2016) Transporter assays as useful *in vitro* tools in drug discovery and development. *Expert Opin Drug Discov* **11**:91–103, Informa Healthcare.

von Bonsdorff C-H, Fuller SD, and Simons K (1985) Apical and basolateral endocytosis in Madin-Darby canine kidney (MDCK) cells grown on nitrocellulose filters. *EMBO J* **4**:2781–2792.

**Modelling Supplemental Data.**

**Modelling Supplemental Data File 1:** Simulated PK of rivaroxaban in mild renal impairment.

**Modelling Supplemental Data File 2:** Predicted extent of DDI between rivaroxaban and verapamil in a healthy population.

**Modelling Supplemental Data File 3:** Predicted magnitude of DDI between ketoconazole and rivaroxaban in a healthy population where the $K_i$ of ketoconazole against OAT3-mediated rivaroxaban uptake has been optimized.

**Modelling Supplemental Data File 4:** Simulated PK of rivaroxaban in the absence of mechanistic kidney modelling

**Modelling Supplemental Data File 5:** Simulated PK of rivaroxaban in the presence of mechanistic kidney modelling